

INLET VORTEX FORMATION UNDER CROSSWIND CONDITIONS

by

Nathan Rosendo Horvath

A Thesis

Submitted to the Faculty

of the

WORCESTER POLYTECHNIC INSTITUTE

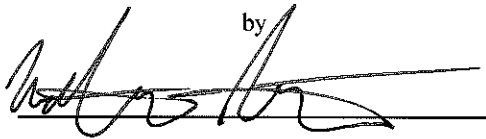
in partial fulfillment of the requirements for the

Degree of Master of Science

in

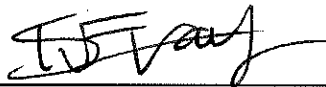
Mechanical Engineering

by

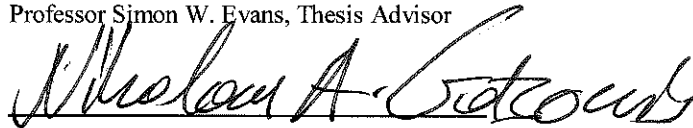


April 2013

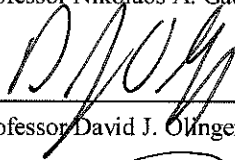
APPROVED:



Professor Simon W. Evans, Thesis Advisor



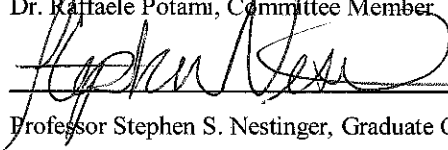
Professor Nikolaos A. Gatsonis, Committee Member



Professor David J. Olinger, Committee Member



Dr. Raffaele Potami, Committee Member



Professor Stephen S. Nestinger, Graduate Committee Representative

Dedicada à minha família,

Gabriel, Siomara,

Kevin e Alexander,

com amor e gratidão.

Abstract

A jet engine operating near the ground at low aircraft speeds, high thrust, and subject to a crosswind, can experience a flow separation region on the windward inlet lip and the formation of a vortex that extends from the ground to the engine fan face, known as the inlet vortex. This structure forms from a single point on the ground and is ingested by the engine. Inlet vortices are often observed during engine power-up at the start of the take-off run. They create considerable stagnation pressure losses and flow distortions at the engine fan face, compromising fan efficiency, thrust, and increasing the potential for compressor surge. Inlet vortices have enough suction power to kick up sand and rocks that are then sucked into the engine when an aircraft is operating near the ground and especially over poorly-maintained tarmac. Thus foreign object damage (FOD) becomes a serious threat for an engine under these conditions, and may lead to compressor blade erosion, deteriorating engine performance and reducing service life. The work presented here used ANSYS FLUENT to model a jet engine under crosswind. The 3-D Navier-Stokes equations were solved for compressible, unsteady flow. The mesh generated contained 5.6 million tetrahedral and wedge elements. The goal of this research was to better understand the inlet vortex formation mechanisms by studying its transient formation process, and to provide new information for future development of vortex prevention techniques. This work has shown multiple smaller inlet vortices coexisting on the ground plane during the first 0.9s of the formation process. After about 1s, these vortices are shown to coalesce and form one single inlet vortex, containing the circulation of all the smaller vortices combined. The smaller vortices were weak enough to not present danger of FOD, but once coalesced could lift up a 16cm diameter chunk of tarmac asphalt. The conclusion of this work is a recommendation for the development of a solution to the inlet vortex problem focused on preventing the coalescing of the vortex during its formation, thus eliminating the threat of FOD.

Acknowledgements

I am particularly grateful for the guidance, support and mentorship provided by my thesis advisor Prof. Simon Evans. His willingness to be interrupted at the most unexpected moments is greatly valued. His wealth of knowledge and natural teaching ability have been indispensable. It has truly been a privilege to work with him.

I would like to offer my special thanks to the following individuals: Raffaele Potami for sharing his knowledge of CFD and expertise in data storage; Adriana Hera for her insightful guidance in ANSYS meshing; Sia Najafi and Randy Robinson for their technical support. I would also like to offer my sincere gratitude to Ali Nematbakhsh for contributing with his Tecplot and CFD experience throughout the course of this project. I appreciate the many conversations about our research, CFD, life and religion.

I am deeply grateful for the caring and tender support of my girlfriend Vicky. She is truly my best friend and her joyful spirit has been a great encouragement.

I also acknowledge the loving support of my family, Gabriel, Siomara, Kevin and Alex. I appreciate all the sacrifices they have made during my six years at WPI. Their encouragement, prayers, kind suggestions and occasional rebukes have made my journey both fruitful and rewarding. Their love is a gift from God and I am deeply indebted to them.

And most importantly, I would like to thank my God for supplying me with divine strength to carry out this work. I acknowledge that I would not be the man I am today had Christ not loved me in the midst of my sinfulness and given Himself up for me (Galatians 2:20). I am grateful for His daily presence in my life, for the lifelong friends I have made here and for the wonderful opportunities He has given me during my time in Worcester.

Table of Contents

Abstract	i
Acknowledgements.....	ii
List of Figures.....	vi
Nomenclature	ix
Chapter 1. Introduction	1
1.1 Background and motivation.....	1
1.2 Research objective.....	3
1.3 Research approach.....	3
1.4 Outline	4
Chapter 2. Literature Survey	5
2.1 Introduction.....	5
2.1 Inlet vortex occurrence	5
2.2 Lip separation region and FOD.....	7
2.3 Inlet vortex formation criteria	8
2.4 Inlet vortex flowfield characterization.....	11
2.4.1 Velocity ratio dependence.....	11
2.4.2 Height-to-diameter ratio dependence.....	14
2.4.3 Empirical correlation.....	15
2.4.4 Formation transience.....	16
2.5 Past experimental work.....	16
2.5.1 PIV data.....	17
2.6 Past numerical work	22
2.6.1 Potential flow solutions.....	22
2.6.2 Reynolds-Averaged Navier-Stokes solutions	23
2.7 Vortex prevention methods.....	26
2.8 Conclusions	28
Chapter 3. Numerical Methods.....	30
3.1 Introduction.....	30
3.2 Scaled jet engine model and domain	30
3.3 Mach and Reynolds number scaling.....	33
3.4 Mesh Generation	34
3.4.1 Meshing setup procedure.....	34

3.4.2	Boundary layer considerations.....	34
3.4.3	Mesh refinement considerations	35
3.4.4	Mesh sensitivity study.....	37
3.4.5	Mesh quality assessment	38
3.5	CFD setup specifications	38
3.5.1	General ANSYS FLUENT setup characteristics	39
3.5.2	Boundary conditions determination and setup.....	39
3.5.3	Further boundary condition considerations	43
3.5.4	Solution methods specifications	43
3.5.5	Residuals, monitors and solution convergence.....	43
3.5.6	Solution initialization and iteration setup.....	45
3.6	Case description	45
3.7	Summary	46
Chapter 4.	Data Processing Methodology.....	47
4.1	Fan face distortion coefficient, DC60.....	47
4.2	Circulation, Γ	49
4.3	Conclusion	55
Chapter 5.	Model Validation.....	56
5.1	Experimental model description.....	56
5.2	Comparison of results	58
5.3	Conclusion	61
Chapter 6.	Time History of Inlet Vortex Formation	62
6.1	Case description	62
6.1.1	Velocity profile.....	63
6.2	Summary of observed vortices.....	66
6.3	Flowfield characterization.....	67
6.3.1	Inlet, trailing and secondary vortex plane definitions	67
6.3.2	Two upstream counter-rotating vortices – time step 0.16s.....	69
6.3.3	Two downstream counter-rotating vortices – time step 0.49s.....	75
6.3.4	Three downstream vortices – time step 0.56s.....	82
6.3.5	Step-change in farfield wind speed – time step 0.65s.....	87
6.3.6	Three vortices shift upstream – time step 0.80s.....	92
6.3.7	Vortex coalescing – time step 0.95s.....	97
6.3.8	Final time step, 1.15s	103
6.4	Time history of relevant parameters.....	109

6.4.1	Minimum pressure on near-ground plane.....	109
6.4.2	Inlet vortex strength.....	112
6.4.3	Trailing vortex strength.....	115
6.4.4	Secondary vortex strength.....	117
6.4.5	Total circulation plots.....	119
6.4.6	Fan face distortion coefficient, DC60.....	121
6.5	Conclusion.....	123
Chapter 7.	Conclusions and Recommendations.....	125
7.1	Conclusions.....	125
7.2	Recommendations.....	128
7.2.1	Engine ramp-up study.....	129
7.2.2	Vortex prevention considerations.....	129
7.2.3	Experimental rig and testing.....	130
Bibliography	131

List of Figures

Figure 1.1 Ground vortex on a military turbofan engine visible due to water condensation inside core (Shmilovich and Yadin, 2011).....	2
Figure 2.1 Inlet vortex seen on a (a) jet engine test stand, (b) YC-14 military aircraft, and (c) C-130 aircraft propeller (Trapp and Girardi, 2010).....	6
Figure 2.2 Schematic of lip separation with a shock wave on engine in crosswind (Wakelam et al., 2012).....	8
Figure 2.3 Inlet vortex flow model (Colehour et al., 1971).....	9
Figure 2.4 Streamlines associated with twin inlets at 90° of yaw in an irrotational upstream flow (De Siervi et al., 1982).....	10
Figure 2.5 Flow regime at (a) low V_i/V_∞ and (b) high V_i/V_∞ , in an irrotational upstream flow (De Siervi et al., 1982).....	12
Figure 2.6 Schematic of variations in flow regime as CR is varied (Shin et al., 1986).....	13
Figure 2.7 Existing data of inlet vortex formation and its correlation (Nakayama and Jones, 1999).....	15
Figure 2.8 Schematic of approaching wind direction: (a) headwind, (b) tailwind, (c) crosswind and (d) crosswind at a α yaw angle.....	17
Figure 2.9 Effect of approaching boundary layer thickness on (a) the vortex strength and (b) fan face distortion, DC60 (Murphy and MacManus, 2011).....	18
Figure 2.10 Plots of fan face average stagnation pressure contours at a fixed $h/D_1 = 0.25$ for velocity ratios of (a) 12.1, (b) 9.1, (c) 7.3, (d) 6.1, (e) 5.2 and (f) 4.6 (Murphy and MacManus, 2011).....	20
Figure 2.11 Contours of stagnation pressure at the fan face for (a) an $h/D_1 = 0.25$ and (b) an $h/D_1 = 0.4$ at a comparable velocity ratio of $V_i/V_\infty = 6.2$ (Murphy and MacManus, 2011).....	21
Figure 2.12 The distortion coefficient, DC60, against velocity ratio for the two investigated non-dimensional heights (Murphy and MacManus, 2011).....	21
Figure 2.13 Particle traces that form the trailing vortex (Trapp and Girardi, 2012).....	24
Figure 2.14 CFD results showing pressure contours on wing and fuselage surfaces due to a crosswind on aft-mounted engines of a business jet.....	25
Figure 2.15 Blow-away jet system for inlet-vortex avoidance, image from the patent of Klein (1959).....	26
Figure 2.16 Cox and William (1969) system for inlet vortex attachment.....	27
Figure 3.1 Dimensioned sketch of jet engine model, in centimeters.....	31
Figure 3.2 Dimensioned domain enclosing jet engine model, with labelled faces and coordinate system.....	32
Figure 3.3 (a) Meshed domain, (b) close-up view of refined “bubble” region, and (c) close-up view of lip inflation layers.....	36
Figure 3.4 Mesh sensitivity plots showing vortex (a) X location and (b) Z location.....	37
Figure 4.1 Tecplot circular zones created on near-ground plane ($Y = -0.18589$ m), showing y-vorticity contours.....	51
Figure 4.2 Zone radius sensitivity plot.....	54
Figure 5.1 Velocity vectors and out-of-plane vorticity contours on the measurement plane with coordinates non-dimensionalized by inlet highlight diameter, obtained from (a) the numerical calculation and (b) Murphy and MacManus (2011).....	58
Figure 5.2 Out-of-plane velocity contours on the measurement plane obtained from (a) the numerical calculation and (b) Murphy and MacManus (2011).....	59

Figure 5.3 Fan face stagnation pressure contours on the measurement plane, non-dimensionalized by far upwind stagnation pressure and fan face averaged dynamic pressure, obtained from (a) the numerical calculation and (b) Murphy and MacManus (2011).	60
Figure 6.1 Vortex formation correlation, highlighting the two cases studied in this report (De Siervi <i>et al.</i> , 1982).	63
Figure 6.2 Time history of (a) crosswind speed V_∞ and (b) velocity ratio V_i/V_∞	65
Figure 6.3 (a) Location of near-ground plane and (b) definition of positive vorticity on this plane.	68
Figure 6.4 (a) Location of trailing vortex plane and (b) definition of positive vorticity on this plane.	68
Figure 6.5 (a) Location of secondary vortex plane and (b) definition of positive vorticity on this plane.	69
Figure 6.6 (a) Velocity vectors, (b) static gauge pressure contours, and (c) out-of-plane vorticity contours on near-ground plane, followed by (d) out-of-plane vorticity contours and (e) stagnation pressure on the fan face plane, accompanied by (f) vorticity magnitude iso-surfaces to visualizing vortex core profiles and (g) vortex filament sketch summarizing the flow field at time 0.16s.	75
Figure 6.7 (a) Velocity vectors, (b) static gauge pressure contours, and (c) out-of-plane vorticity contours on near-ground plane, followed by (d) out-of-plane vorticity contours and (e) stagnation pressure on the fan face plane, accompanied by (f) vorticity magnitude iso-surfaces to visualizing vortex core profiles and (g) vortex filament sketch summarizing the flow field at time 0.49s.	82
Figure 6.8 (a) Velocity vectors, (b) static gauge pressure contours, and (c) out-of-plane vorticity contours on near-ground plane, followed by (d) out-of-plane vorticity contours and (e) stagnation pressure on the fan face plane, accompanied by (f) vorticity magnitude iso-surfaces to visualizing vortex core profiles and (g) vortex filament sketch summarizing the flow field at time 0.56s.	87
Figure 6.9 (a) Velocity vectors, (b) static gauge pressure contours, and (c) out-of-plane vorticity contours on near-ground plane, followed by (d) out-of-plane vorticity contours and (e) stagnation pressure on the fan face plane, accompanied by (f) vorticity magnitude iso-surfaces to visualizing vortex core profiles and (g) vortex filament sketch summarizing the flow field at time 0.65s.	92
Figure 6.10 (a) Velocity vectors, (b) static gauge pressure contours, and (c) out-of-plane vorticity contours on near-ground plane, followed by (d) out-of-plane vorticity contours and (e) stagnation pressure on the fan face plane, accompanied by (f) vorticity magnitude iso-surfaces to visualizing vortex core profiles and (g) vortex filament sketch summarizing the flow field at time 0.80s.	97
Figure 6.11 (a) Velocity vectors, (b) static gauge pressure contours, and (c) out-of-plane vorticity contours on near-ground plane, followed by (d) out-of-plane vorticity contours and (e) stagnation pressure on the fan face plane, accompanied by (f) vorticity magnitude iso-surfaces to visualizing vortex core profiles and (g) vortex filament sketch summarizing the flow field at time 0.95s. ...	103
Figure 6.12 (a) Velocity vectors, (b) static gauge pressure contours, and (c) out-of-plane vorticity contours on near-ground plane, followed by (d) out-of-plane vorticity contours and (e) stagnation pressure on the fan face plane, accompanied by (f) vorticity magnitude iso-surfaces to visualizing vortex core profiles, (g) inlet and trailing vortex streamtraces and (g) vortex filament sketch summarizing the flow field at time 1.15s.	108
Figure 6.13 Time history of minimum gauge pressure on near-ground plane.	110
Figure 6.14 Time histories of (a) maximum diameter and (b) maximum mass of asphalt chunk that could be lifted off the ground by the inlet vortices and cause FOD, calculated based on the near-ground plane.	110
Figure 6.15 Time history of inlet vortex strength, calculated on the near-ground plane.	113
Figure 6.16 Time history of trailing vortex strength, calculated on trailing vortex plane.	116
Figure 6.17 Time history of secondary vortex strength calculated on the secondary vortex plane.	118

Figure 6.18 Time histories of (a) total circulation for inlet, trailing and secondary vortices and (b) combined circulation of all vortices.....	120
Figure 6.19 Time history of fan face distortion parameter, DC_{60}	123
Figure 7.1 Conceptual design of experimental rig.....	130

Nomenclature

V	Velocity
H or h	Height (from the ground)
D	Diameter
M	Mach number
\dot{m}	Mass flow rate
p	Pressure
T	Static temperature
ρ	Air density
Re	Reynolds number
A	Area
Γ	Circulation
ω	Vorticity
h	Measuring plane height from the ground
ν	Viscosity
C	Specific heat coefficient
γ	Adiabatic coefficient
δ^*	Boundary layer thickness
DC_{60}	Fan-face pressure distortion coefficient
X	Downstream crosswind dimension
Y	Dimension normal to ground
Z	Intake axial dimension
<u>Subscripts</u>	
i	Intake
∞	Upstream crosswind
j	Jet
t	Stagnation
o	Outer
h	Highlight
min	Minimum
max	Maximum
x	Crosswind direction

y Out-of-ground direction
z Intake axial direction

Abbreviations

CFD	Computational Fluid Dynamics
2-D	Two dimensional
3-D	Three dimensional
u-RANS	Unsteady Reynolds-Averaged Navier-Stokes
CR	Capture Ratio
BC	Boundary Condition
CPU	Central Processing Unit
FOD	Foreign Object Damage

Chapter 1. Introduction

1.1 Background and motivation

The technological advancements of recent decades have made air travel more accessible than ever before. The consequent swelling number of air travelers worldwide, coupled with rising fuel costs, is now leading airlines to demand more fuel-efficient, low-maintenance jet engines. Engine manufacturers have responded with high-bypass turbofan engines characterized by larger-than-ever nacelle diameters for improved performance. However, this effective solution increases the risk of Foreign Object Damage (FOD), as it places the engines closer to the ground.

A jet engine operating near the ground in static or near static conditions, at high-thrust, and subject to a crosswind, can experience a flow separation region on the windward inlet lip and the formation of a ground-to-inlet vortex, known as the inlet vortex. The operating conditions that cause these phenomena often coincide with engine power-up at the start of the take-off run. The inlet vortex, depicted in Figure 1.1, has been investigated for over six decades, but the mechanisms by which it originates and is maintained are still not well understood, and an adequate prevention technique has yet to be developed.

The impact of the inlet vortex and lip separation on engine performance is significant. Both create stagnation pressure losses – resulting in reduced inlet recovery – and flow distortions at the fan face. These distortions are associated with momentum loss and large velocity gradients as the non-uniform flow reaches the fan face. They can alter the local flow angle seen by the fan blades, decreasing fan efficiency and thrust, reducing compressor stall margins and consequently increasing the likelihood of compressor surge. Due to local flow separations on blade surfaces, inlet vortices and lip separation have been shown to induce fan vibration, generating large resonant forces leading to high cycle fatigue (Murphy, 2008).



Figure 1.1 Ground vortex on a military turboprop engine visible due to water condensation inside core (Shmilovich and Yadlin, 2011).

Moreover, the likelihood of FOD is largely increased when a vortex is present. An inlet vortex has enough suction power to pick up objects such as sand, dirt and rocks when an aircraft is operating near the ground and especially over poorly-maintained tarmac or on dirt airstrips. If these are ingested by the engine, compressor blade erosion can occur, deteriorating engine performance and reducing service life.

Numerical techniques have recently been used to model the inlet vortex phenomenon. However, none have endeavored to study in detail the transient behavior of this inherently unsteady problem. The research described here uses an unsteady computational fluid dynamics (CFD) model to provide a fundamental understanding of the transient formation process of the inlet vortex under crosswind conditions, from its inception to the fully-developed vortex. Two crosswind scenarios were modeled in the same calculation by varying the wind speed and keeping the engine suction speed constant.

1.2 Research objective

The objective of the research discussed in this thesis was to study the formation mechanisms by which the inlet vortex originates and is sustained, so as to inform the development of preventive techniques. This was accomplished by conducting a detailed numerical analysis, investigating the transient behavior of the inlet vortex system. To the best of this author's knowledge, no other research team has studied the unsteadiness of inlet vortex formation.

1.3 Research approach

To accomplish this task, the full 3-D Navier-Stokes equations were solved using ANSYS FLUENT 14, a commercial CFD software, for a 7.5% scale cylindrical model of a jet engine inlet. An unsteady, compressible, and turbulent Reynolds-Averaged Navier-Stokes (RANS) model was used. In order to ensure a mesh-independent solution, a grid sensitivity study was performed, enabling the selection of an adequate mesh. Before proceeding with the desired case study, a validation of the numerical model was conducted, based on a published experiment from Cranfield University (Murphy and MacManus, 2011). Once the validation process was concluded and an effective simulation procedure developed, one extensive simulation was carried out with a

carefully refined mesh. Boundary conditions were determined such that a clear, strong inlet vortex was expected to form, based on experimental data from the literature. Small time step sizes were chosen to not only ensure stability in the numerical calculation, but also to analyze the evolution of the inlet vortex with time. All simulations were conducted on parallel CPUs to decrease total computational time.

1.4 Outline

The introduction presented here is followed by Chapter 2, containing a survey of the relevant literature regarding the inlet vortex problem. Chapter 3 describes the computational methods employed in this thesis research, providing insight into numerical modeling, software setup and data processing. The case studied in this research is also outlined in detail in Chapter 3. The methods by which data was gathered and processed are fully explained in Chapter 4, Data Processing Methodology. Chapter 5 outlines the model validation. Chapter 6 presents and discusses the results of the case simulated in this research, drawing conclusions based on flowfield observations. Chapter 7 concludes the report, summarizing the most relevant conclusions, discussing the limitations of the work contained herein, and presenting recommendations for continuation of this research.

Chapter 2. Literature Survey

2.1 Introduction

This chapter presents a survey of available and relevant literature pertaining to the inlet vortex problem. Section 2.2 introduces the inlet vortex and provides real images of observed occurrences. Section 2.3 describes the inlet lip separation accompanying the vortex, and provides insight concerning FOD occurrence. It is followed by section 2.4, which presents the requirements for vortex formation, and section 2.5, characterizing the inlet vortex flow field. Section 2.6 highlights major experimental work done in the past decades, and section 2.7 outlines the numerical work to date. The chapter concludes with a brief presentation of the key vortex prevention methods proposed by past investigators.

2.1 Inlet vortex occurrence

Since the advent of jet engines in large commercial airliners during the 1950s, ingestion of foreign objects has been a popular topic of study. The existence of the inlet vortex system and its alarming impact on FOD occurrence were known in the second half of the twentieth century, but very few experiments had been conducted to investigate these issues. Initial attempts at studying the inlet vortex were made using engines on test stands, and soon afterwards scaled

model inlets were tested in wind tunnels. In the 1970s, panel methods and computer codes were developed to gain further insight into the phenomenon, but only in the past decade has CFD been applied to its study (Trapp and Girardi, 2010; 2012).

Figure 2.1 shows the inlet vortex in three distinct scenarios: part (a) shows the vortex in an engine on a test stand in close proximity to the ground, part (b) shows it on a military engine far above the ground, and part (c) shows it on a propeller aircraft. These figures demonstrate that the vortex can occur in a wide range of design and operating conditions.



(a)



(b)



(c)

Figure 2.1 Inlet vortex seen on a (a) jet engine test stand, (b) YC-14 military aircraft, and (c) C-130 aircraft propeller (Trapp and Girardi, 2010).

In standard atmospheric conditions, the vortex is invisible. However, the local flow temperature within the vortex core can fall below the dew point temperature. If enough humidity is present in the air, condensation will occur, making the vortex visible. Also, if water or sand is present on the ground, it may be sucked up into the vortex and thus outline its core.

2.2 Lip separation region and FOD

When an aircraft engine is caught in a crosswind, the inlet vortex shown in Figure 2.1 is accompanied by a flow separation area on the windward lip. This happens due to the flow turning around the lip edge as it is sucked into the engine. As the flow bends around the lip edge, it may approach transonic speeds depending on the engine mass flow rate and inlet leading edge geometry, creating shock waves between the lip and fan face. Figure 2.2 shows a schematic of this lip separation region.

Inlet vortices and windward lip separation cause significant engine performance losses, since both these phenomena create stagnation pressure deficits and flow distortions at the fan face. As the distorted flow arrives at the compressor stage of the engine, it may cause flow blockage in between blade passages, leading to compressor blade stall and increasing the potential for compressor surge. There is also a considerable loss of thrust associated with the pressure losses and consequent reduced inlet recovery. A turbofan engine, for example, will suffer a 13% loss in thrust due to a 10% loss in inlet recovery (Raymer, 2006), where inlet recovery is the total pressure delivered to the engine divided by freestream total pressure. It is thus important that stagnation pressure losses associated with the ingested flow be kept to a minimum.

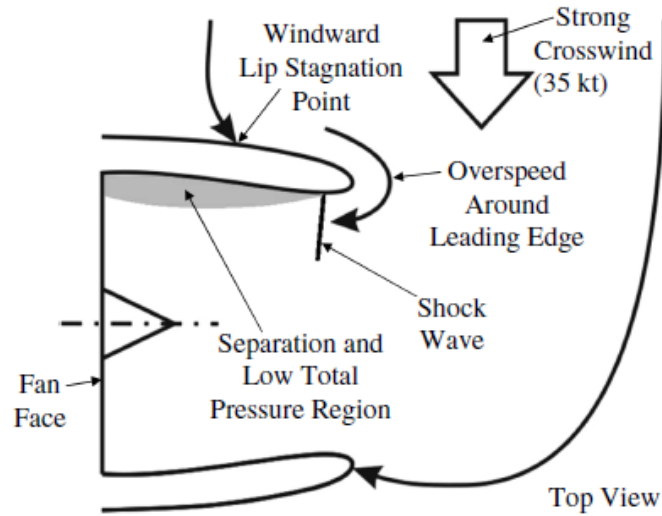


Figure 2.2 Schematic of lip separation with a shock wave on engine in crosswind (Wakelam et al., 2012).

Additionally, FOD becomes a serious threat when a vortex is present. It has been observed that the average suction force on the ground of an engine without an inlet vortex is less than 11b. On the other hand, an engine with an inlet vortex present can produce a force of 40lb (Colehour *et al.*, 1971). Consequently, an inlet vortex has the necessary suction strength to kick up debris into the engine when an aircraft is operating near the ground. This can cause compressor blade erosion (in the event of sand ingestion), deteriorating engine performance and reducing service life. The mechanism by which this happens has been demonstrated by Colehour *et al.* (1971), revealing that foreign objects do not enter the jet engine via the inlet vortex core, as was previously thought. Rather, they are entrained in the inlet flow field and carried into the inlet after being kicked up from the ground by the vortex.

2.3 Inlet vortex formation criteria

The first author to propose the minimum requirements for an inlet vortex to exist was Klein (1959), stating that:

1. A stagnation point must exist on the ground (or other fixed structure), where an omnidirectional airflow parallel to the surface converges in a manner similar to a sink.
2. There must be an updraft from the stagnation point to the inlet.
3. Ambient vorticity must be present in the flow.

Figure 2.3 illustrates the model explained by Klein (1959). It shows that the flow coming from multiple directions convergences and forms a stagnation point on the ground. The inlet suction induces an updraft, which pulls this slower air around the stagnation point upwards, forming the vortex core. Klein (1959) proposed that ambient vorticity was the principal source of vorticity in the vortex core flow, and without it the inlet vortex would not form.

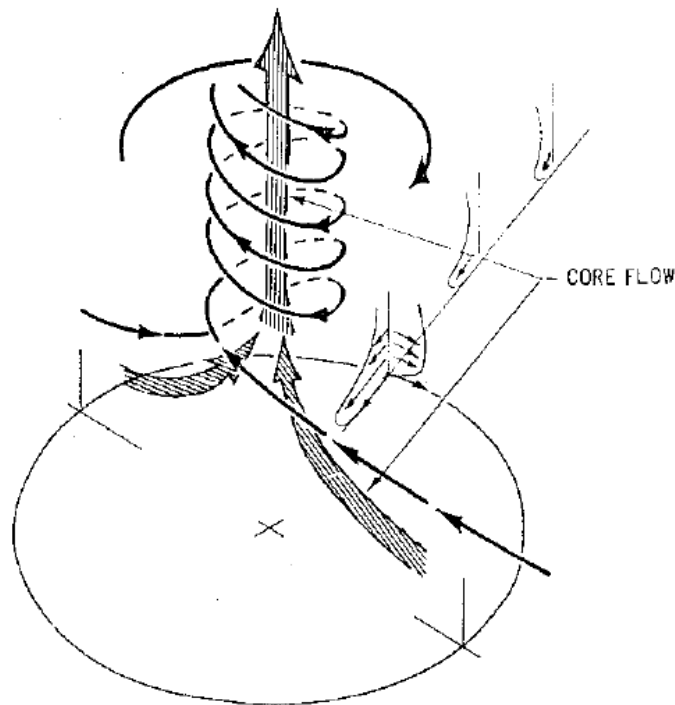


Figure 2.3 Inlet vortex flow model (Colehour et al., 1971).

De Siervi *et al.* (1982) conducted experiments to study the mechanisms of the inlet vortex formation. One particular experiment was undertaken to understand whether or not ambient vorticity and/or the ground boundary layer played a role in creating the inlet vortex. The

experiments were done by vertically aligning two Plexiglas® inlet models in a water tunnel and generating a crosswind flow. Visualization was made possible by the use of hydrogen bubbles. The setup and flow field observed are pictured in Figure 2.4.

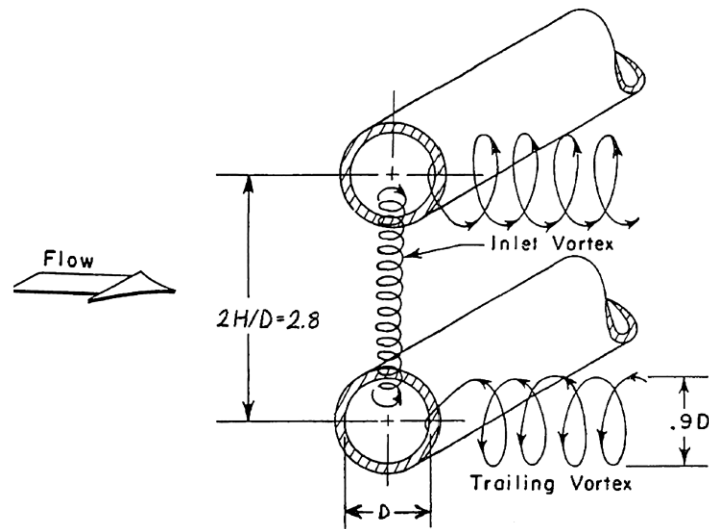


Figure 2.4 Streamlines associated with twin inlets at 90° of yaw in an irrotational upstream flow (De Siervi et al., 1982).

Their observations revealed two fascinating results. Even without a ground plane the inlet vortex still formed. In other words, the vorticity generated within the ground boundary layer is not required for an inlet vortex to form. This experiment was done in an irrotational flow field, with no upstream vorticity sources. The fact that the inlet vortex was observed in an upstream irrotational flow dismisses Klein's third requirement, suggesting a different source of vorticity responsible for creating the inlet vortex. De Siervi *et al.* (1982) proposed that the vorticity in the core of the vortex was produced initially by the action of viscosity in the boundary layers on the outer surfaces of the inlet. Once the vortex is formed, however, there is no longer any vorticity convected into the core, and the vorticity needed to maintain the vortex is produced by the extension of the vortex filaments in the core. Hence the presence of a ground boundary layer (or ambient vorticity) is not necessary for the formation of an inlet vortex. Nevertheless, should the

approaching air contain vorticity, then an inlet vortex will form via a different mechanism; one that involves the amplification of the vertical component of this existing ambient vorticity as the vortex lines are convected into the inlet. This work was complimented by Liu *et al.* (1985) and Shin *et al.* (1986), both of which support the above-mentioned vortex formation mechanisms.

2.4 Inlet vortex flowfield characterization

The two fundamental non-dimensional groups typically used to characterize the inlet vortex flow field are: the suction-velocity-to-crosswind-velocity ratio V_i/V_∞ ; and the inlet-height-to-inner-diameter ratio H/D_i . These non-dimensional groups are responsible for defining the capture area of the inlet. The capture area is defined as the region where all the air contained in it is captured by and sucked into the inlet.

2.4.1 Velocity ratio dependence

Figure 2.5 illustrates how the projection of the capture area and velocity ratio are related, as established from experiments carried out by De Siervi *et al.* (1982), along with the resulting vortical flow.

At low velocity ratios ($V_i/V_\infty \leq 5$), corresponding to either a low inlet suction velocity or a high crosswind speed, De Siervi *et al.* (1982) showed that the capture area does not touch the ground, there is no stagnation point on the ground, and an inlet vortex is not present. However, two counter-rotating vortices, referred to as trailing vortices, of roughly equal strength were observed, as shown in Figure 2.5(a). These are formed due to vorticity production along the outer body of the inlet resulting from the convection of boundary layer fluid on the inlet outer walls to the freestream flow. De Siervi *et al.* (1982) observed that the expected inlet lip separation point aft of the engine occurred near the three o'clock location. As the velocity ratio was increased, the authors noticed that the inlet lip separation point shifted clockwise and the upper trailing vortex

became stronger than the lower one. At high velocity ratios ($V_i/V_\infty \geq 20$), corresponding to either a high inlet suction velocity or low crosswind speed, the capture area was shown to overlap with the ground, as depicted in Figure 2.5(b). The lower trailing vortex disappeared and an inlet vortex formed on the ground plane extending into the inlet.

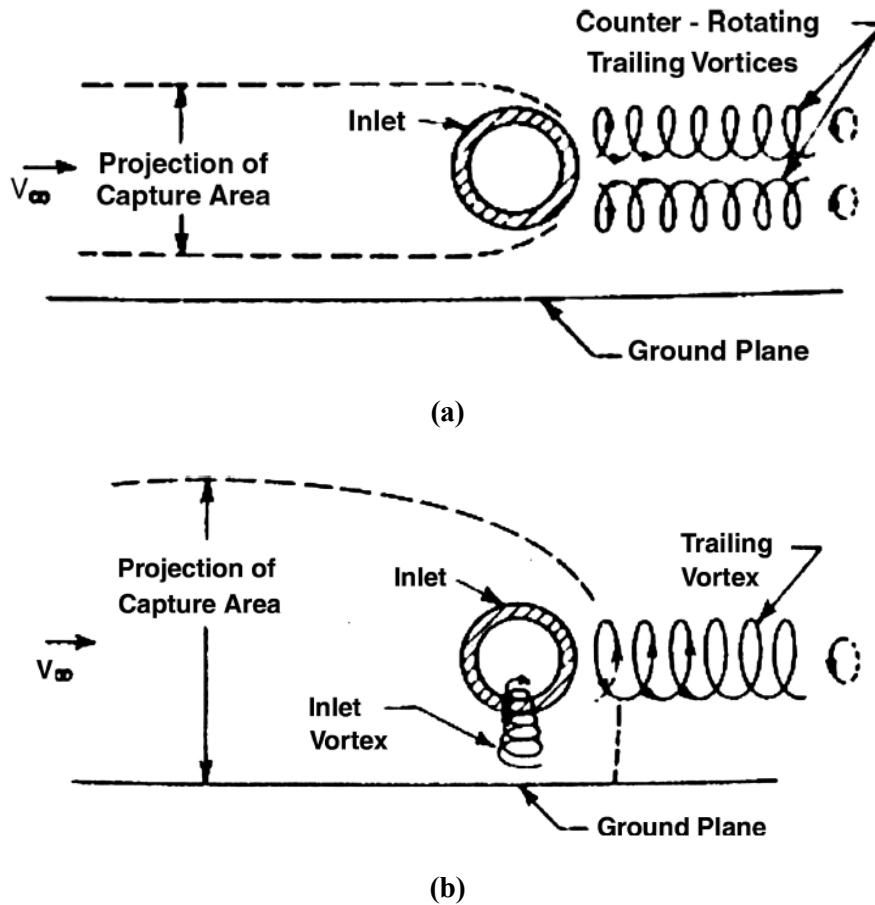


Figure 2.5 Flow regime at (a) low V_i/V_∞ and (b) high V_i/V_∞ , in an irrotational upstream flow (De Siervi et al., 1982).

Figure 2.6 illustrates, in a very simplified form, the variations in flow regime as the capture ratio (CR) is increased, as identified by Shin *et al.* (1986), where the capture ratio is defined as

$$CR = \left(\frac{V_i}{V_\infty}\right) \left(\frac{D_i}{D_o}\right)^2 \quad (2.1)$$

Note that increasing the capture ratio is equivalent to increasing the velocity ratio, provided the comparison is made between identical inlets. Therefore, these ratios can be used interchangeably.

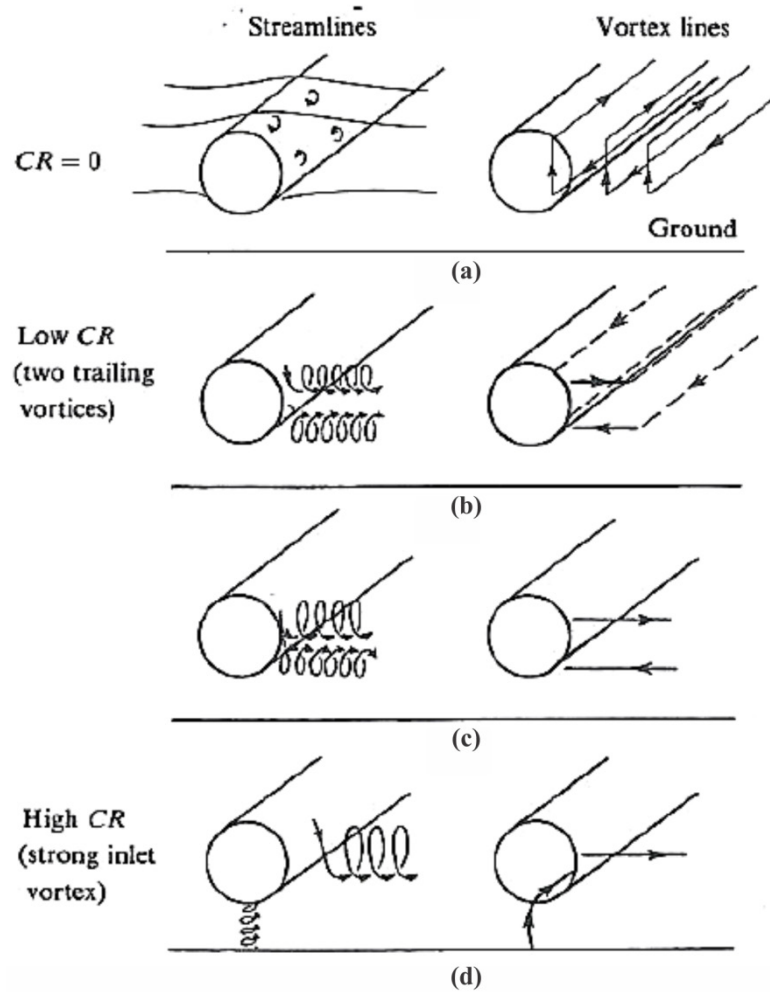


Figure 2.6 Schematic of variations in flow regime as CR is varied (Shin et al., 1986).

Figure 2.6(a) shows that with no inlet suction, the inlet is essentially a semi-infinite cylinder, with vortices shed from the top, bottom, and end of the inlet. Figure 2.6(b) shows that at a low capture ratio (low velocity ratio), two counter-rotating trailing vortices are formed near the trailing edge lip of the inlet. Increasing the capture ratio further shifts the trailing vortex system

downward and counter-clockwise (when viewing the inlet from in front, as in Figure 2.6), with the upper vortex increasing in diameter (i.e. swirling more air over a larger area) and the lower decreasing, as illustrated by Figure 2.6(c). The circulation around each vortex was found to increase, although it remained essentially equal and opposite for the upper and lower vortices (Shin *et al.*, 1986). Lastly, at a high velocity ratio, the upper trailing vortex was shown to increase in diameter once again, and the lower vortex was shown to shift downward and attach itself to the ground, becoming the inlet vortex, as depicted in Figure 2.6(d). It was also observed that the transition of the lower trailing vortex to the inlet vortex is abrupt – once a critical velocity ratio was reached, the lower trailing vortex abruptly attached itself to the ground. Increasing the velocity ratio just slightly above this value resulted in a small upwind shift of the ground attachment location.

2.4.2 Height-to-diameter ratio dependence

The non-dimensional height ratio H/D_i has also been shown to have an effect on inlet vortex occurrence. Experiments conducted by several authors (Motycka *et al.*, 1973; Glenny *et al.*, 1970; Liu *et al.*, 1985; Shin *et al.*, 1986; Murphy *et al.*, 2011) and numerical simulations (Nakayama and Jones, 1999; Trapp and Girardi, 2010) have shown that the capture area needed for ground interaction is smaller at a low H/D_i (engines placed close to the ground), and can therefore be achieved at lower inlet suction speeds. This increases the likelihood of inlet vortex formation on engines positioned on the underside of wings. To avoid operating in this low velocity ratio regime, pilots will gradually bring their aircraft to full thrust at the start of a take-off run, so as to gain speed without allowing the capture area to become too large, and using the effective headwind generated as an aid in blowing off the vortex.

2.4.3 Empirical correlation

Experimental data has been compiled over the decades to develop an empirical correlation between the two non-dimensional groups discussed above, allowing investigators to predict whether a vortex will be present for a given inlet geometry. Figure 2.7 shows this correlation (dotted line) – above the line, an inlet vortex will form, whereas below the line, it will not. The solid line and data points labeled “present data” represent CFD results obtained by Nakayama and Jones (1999). Various experimental results are also shown.

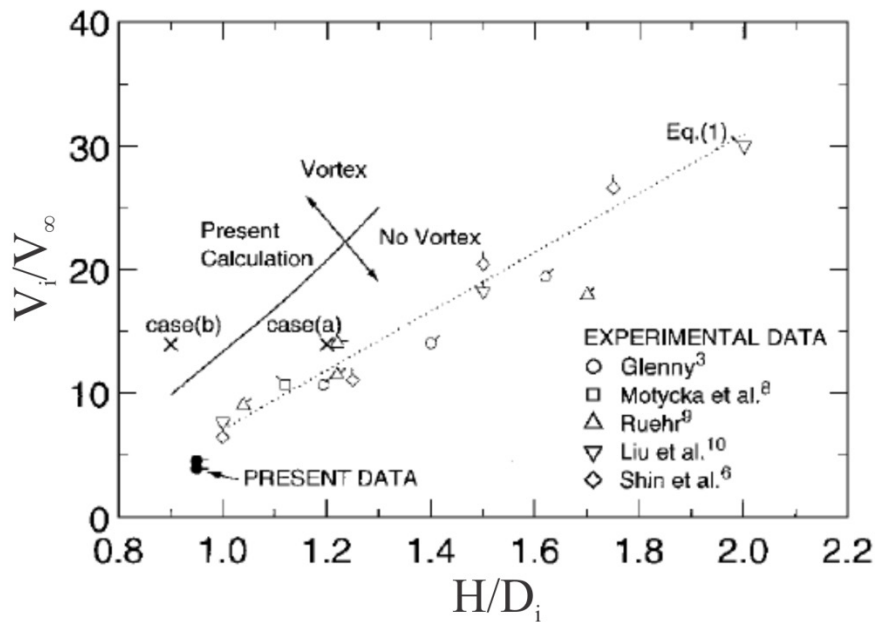


Figure 2.7 Existing data of inlet vortex formation and its correlation (Nakayama and Jones, 1999).

In Figure 2.7, the X axis represents non-dimensional height ratio and the Y axis, the velocity ratio. The dotted line shows a possible correlation for all experiments conducted with inlet vortices by the authors mentioned in the figure. The correlation, developed by data-fitting the results obtained from these authors, was found by Nakayama and Jones (1999) to be:

$$\frac{V_i}{V_\infty} = 24 \times \left(\frac{H}{D_i}\right) - 17 \quad (2.2)$$

To the best of this author's knowledge, there is no data available for very low H/D_i ratios, and therefore this correlation may not be adequate for all non-dimensional height ratios. However, for ratios between 0.9 and 2.0, it is accurate.

For a given non-dimensional height ratio, the minimum velocity ratio for which an inlet vortex will exist is called the critical velocity ratio. The plot above can be used to estimate this ratio for a particular engine, and thus knowing the crosswind velocity experienced by the aircraft, the maximum engine speed can be determined for vortex-free operation.

2.4.4 Formation transience

It has been shown in the literature that the inlet vortex formation process is highly unsteady, with vortex meandering occurring as it attaches itself to the ground. Even though authors such as Brix *et al.* (2000), Funk *et al.* (2001), and Secareanu *et al.* (2005) have pointed this out in their work, there have been very few investigations into the unsteadiness of the phenomenon. This topic still remains an open question and will be addressed in the research provided here.

2.5 Past experimental work

Experimental work has been carried out by various research groups over the past 50 years modeling a number of possible wind scenarios that an engine may encounter: no wind, headwind, tailwind, and crosswind, with varying yaw angles. Figure 2.8 below shows the possible approaching wind directions, looking at a jet engine from above.

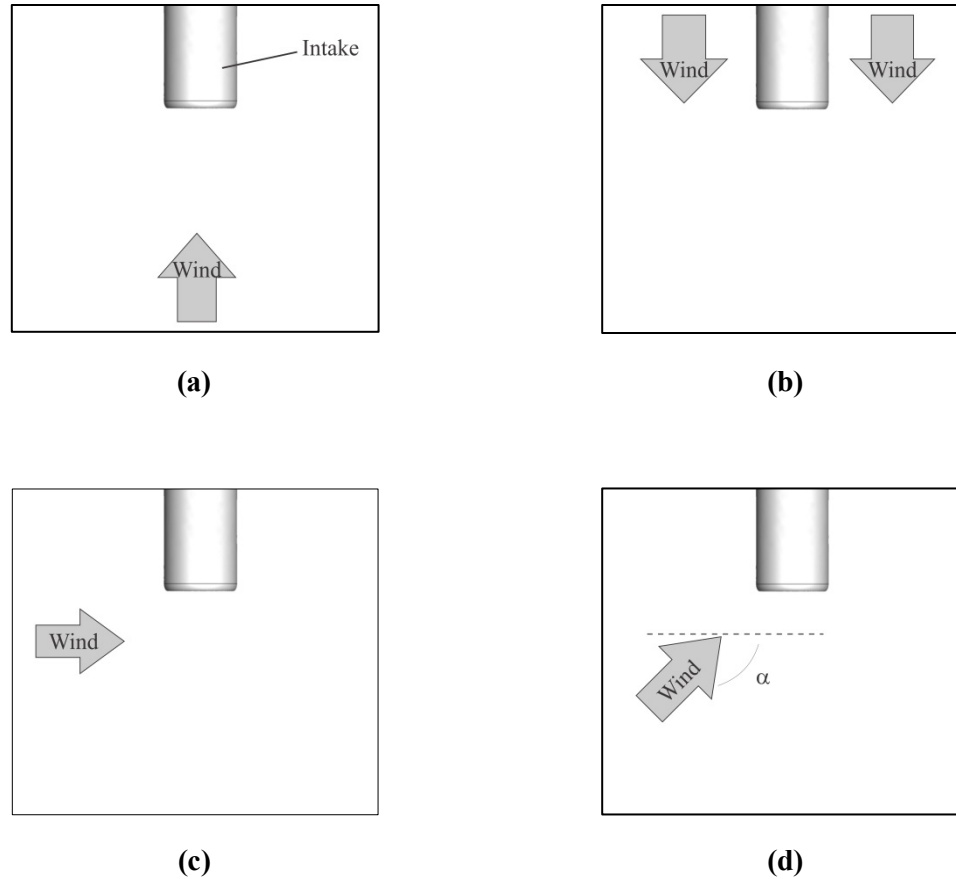


Figure 2.8 Schematic of approaching wind direction: (a) headwind, (b) tailwind, (c) crosswind and (d) crosswind at a α yaw angle.

2.5.1 PIV data

Murphy and MacManus (2011) were the first to apply Stereoscopic Particle Image Velocimetry (SPIV) to the inlet vortex problem, conducting studies on a scaled inlet subject to headwind and crosswind conditions. In 2011, they published an extensive report with quantitative results for various V_i/V_∞ and H/D_i . The data revealed that the inlet vortex strength, i.e. vortex circulation, increases with a decrease in the V_i/V_∞ . In other words, faster crosswinds will yield a stronger inlet vortex, characterized by high core vorticity and consequently high ground suction force. This is consistent with the understanding that the strength of the inlet and trailing vortices

is highly dependent on the vorticity generated around the inlet body, as proposed by Di Siervi *et al.* (1982), and which in turn is directly related to the approaching freestream velocity.

Ground boundary layer independence

Murphy and MacManus (2011) also provided experimental data to prove what has been discussed previously in this chapter: that the inlet vortex is not primarily associated with the ground boundary layer or the ambient vorticity of the approaching flow. In other words, the approaching boundary layer thickness has no significant effect on the characteristics of inlet vortices. The authors demonstrated this by plotting curves of non-dimensionalized circulation around the vortex and fan-face pressure distortion parameter DC_{60} versus velocity ratio, for boundary layer thicknesses of δ^*/D_l equal to 0.11 and 0.03 (D_l is the authors' notation for highlight diameter).

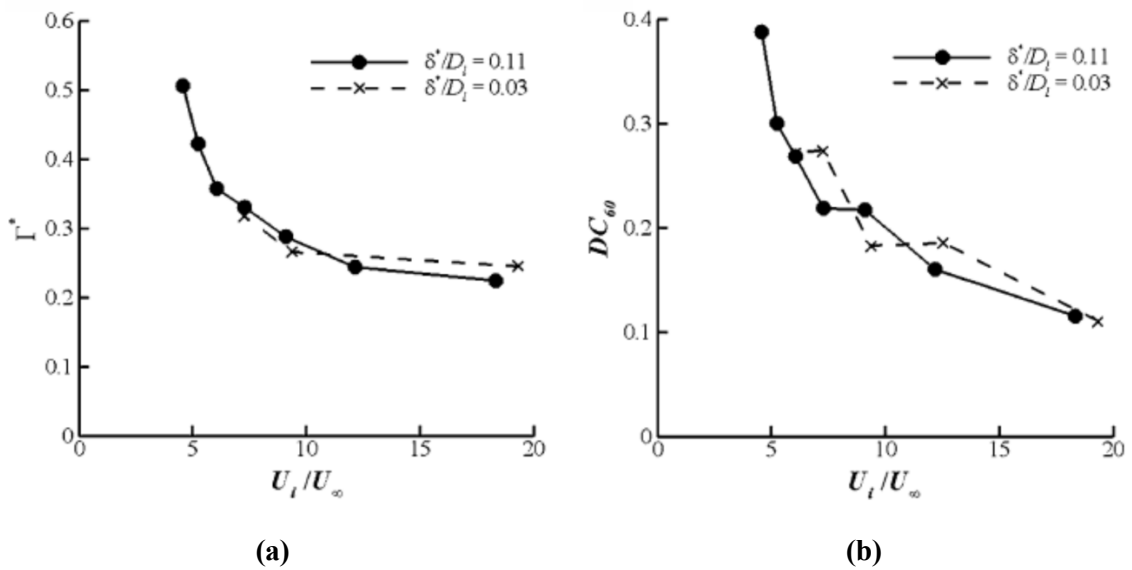


Figure 2.9 Effect of approaching boundary layer thickness on (a) the vortex strength and (b) fan face distortion, DC_{60} (Murphy and MacManus, 2011).

The DC_{60} coefficient is defined as follows:

$$DC_{60} = \frac{P_i - P_{60}}{q_i} \quad (2.3)$$

where P_i is the area-weighted average of stagnation pressure at the fan face measured by the PIV system, P_{60} is the area-weighted average of stagnation pressure at the worst 60-degree sector on the fan face, and q_i is the local dynamic pressure at the fan face. The results, shown in Figure 2.9, revealed negligible differences for the two cases, which had a fixed $H/D_l = 0.25$.

Vortex ingestion location and separation region

As previously mentioned, an inlet under a crosswind will also experience a region of flow separation on the windward side of the lip. This separation region, combined with the ingestion location of the inlet vortex, creates regions of stagnation pressure loss on the fan face.

Figure 2.10 shows non-dimensional stagnation pressure contours of the flow separation region and vortex ingestion location for increasing crosswind speeds. The data, gathered by Murphy and MacManus (2011), was non-dimensionalized with freestream stagnation pressure and dynamic pressure at the fan plane. The contours show that the vortex ingestion location corresponds to the region of greater stagnation pressure deficit, and that this location is on the upwind side of the inlet, shifting clockwise as the crosswind speed is increased. The magnitude of this pressure drop at the inlet vortex ingestion point also increases as the crosswind speed is increased (or velocity ratio decreased), confirming initial conclusions made by De Siervi *et al.* (1982) that at higher crosswind speeds, the vortex will be stronger and larger in size. Additionally, the separation region on the windward lip began to appear at a velocity ratio of 6.1 and, as expected, increased considerably in size as the crosswind speed increased. Since at these speeds the flow had more difficulty bending around the inlet lip, a separation bubble formed, as is illustrated schematically in Figure 2.2.

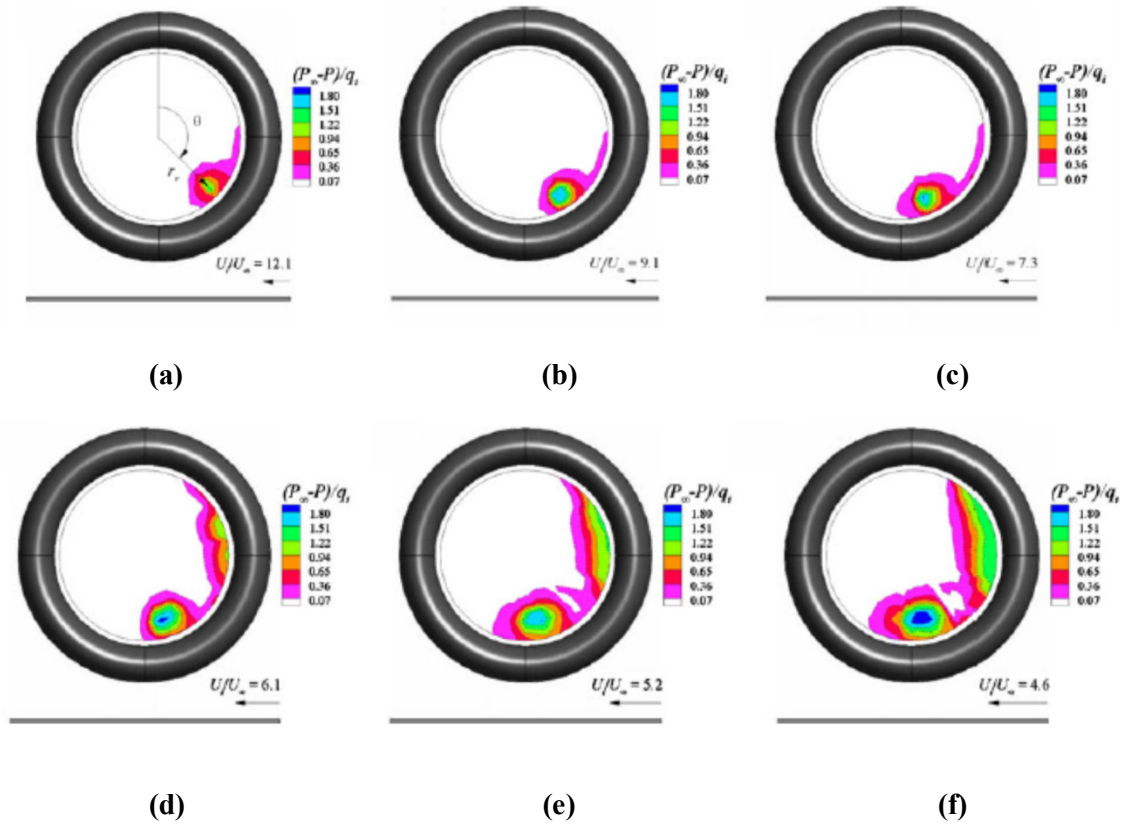


Figure 2.10 Plots of fan face average stagnation pressure contours at a fixed $h/DI = 0.25$ for velocity ratios of (a) 12.1, (b) 9.1, (c) 7.3, (d) 6.1, (e) 5.2 and (f) 4.6 (Murphy and MacManus, 2011).

Non-dimensional height ratio dependence

Figure 2.11 compares stagnation pressure profiles of two inlets of non-dimensional heights equal to 0.25 and 0.40 for a velocity ratio of 6.1. It shows that at a higher distance from the ground plane, a jet engine may not experience the formation of inlet vortices or large windward separation, at a given velocity ratio. This is in alignment with the observations made by De Siervi *et al.* (1982) and the correlation presented in equation (2.1).

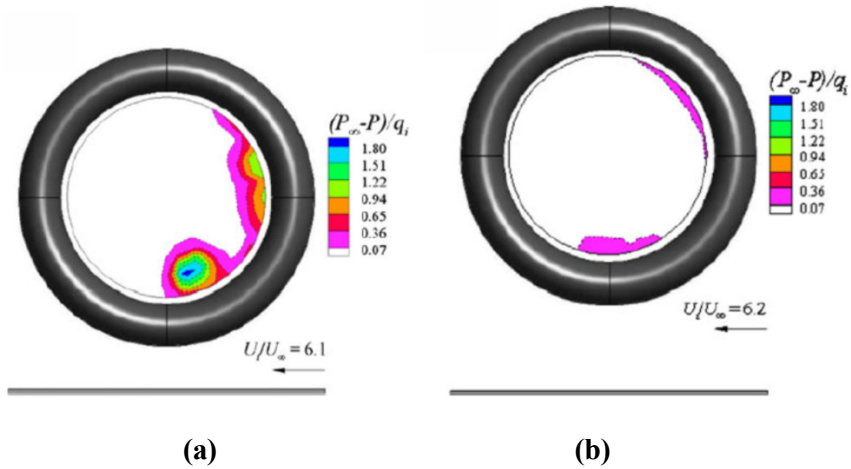


Figure 2.11 Contours of stagnation pressure at the fan face for (a) an $h/D_1 = 0.25$ and (b) an $h/D_1 = 0.4$ at a comparable velocity ratio of $V_i/V_\infty = 6.2$ (Murphy and MacManus, 2011).

The corresponding fan face distortion coefficient DC_{60} , calculated by Murphy and MacManus (2011), is plotted in Figure 2.12 for the two non-dimensional height ratios investigated.

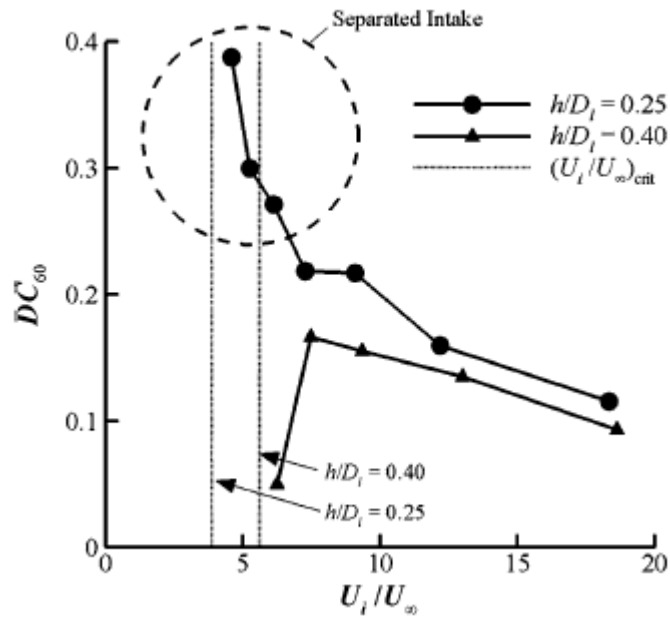


Figure 2.12 The distortion coefficient, DC_{60} , against velocity ratio for the two investigated non-dimensional heights (Murphy and MacManus, 2011).

The general trend shown in Figure 2.12 for $h/D_1 = 0.25$ confirms the expected increase in stagnation pressure loss as the velocity ratio is decreased, as depicted previously in Figure 2.10, for a non-dimensional height of 0.25 (with respect to the highlight diameter). The three data points at the top of the curve (inside the dotted circle) correspond to velocity ratios of 6.1, 5.2 and 4.6, and reveal DC_{60} values that are double in magnitude when compared to the other three data points (of velocity ratios 12.1, 9.1 and 7.3). This supports Figure 2.10, which shows the inlet containing a separation region on the windward lip and a strong inlet vortex. Data is also presented for a non-dimensional height of 0.4. This inlet is located farther from the ground plane and the calculation confirms the data presented in Figure 2.11, revealing the absence of an inlet vortex and no separation region.

2.6 Past numerical work

Over the last two decades, computational methods and CFD have been used to investigate the flow physics of numerous fluid mechanics phenomena, including the inlet vortex. The advantage of using CFD lies with the fact that the whole flow regime is calculated, allowing the retrieval of data from any region of interest at any time. Calculations have been performed using various techniques, including potential flow theory, and commercial Reynolds-Averaged Navier-Stokes solvers.

2.6.1 Potential flow solutions

Nakayama and Jones (1999) were among the first to apply computational methods to the inlet vortex problem. The group used potential flow calculations to predict inlet vortex formation and develop a correlation based on their computations and previous experimental work, shown in Figure 2.7. Their calculations did not however, agree well with experimental data, as shown by the figure.

2.6.2 Reynolds-Averaged Navier-Stokes solutions

Ho and Jermy (2007) conducted calculations using the commercial Reynolds-Averaged Navier-Stokes solver ANSYS FLUENT to study the inlet vortex under headwind conditions. The results revealed the presence of an inlet vortex via velocity streamlines and vector plots. The authors also used an incompressible model, even with inlet flow speeds clearly in the compressible range. This affected the accuracy of the results obtained near the lip and fan face regions. Additionally, the grid size used was 100,000 to 200,000 cells, implying a relatively low domain and boundary layer resolution.

An in-house CFD code was developed by Barata *et al.* (2010; 2012) which assumed incompressibility and steady conditions, and was used to solve a 214,000-element grid. The authors modeled several full-scale jet engines from different manufacturers at various velocity ratios. They showed a concentrated low-pressure region on the ground plane in the cases where an inlet vortex was detected. In the cases where no inlet vortex was present, this region was non-existent. The authors clearly detected the formation of the stagnation point on the ground plane needed for inlet vortices to form, as well as additional vortices located on planes parallel to the fan face. These vortices were not a part of the inlet vortex system and had not been previously identified by other investigators. However, Barata and co-authors provided no explanation as to the presence of these vortices or of how they may have come about.

Trapp and Girardi (2010), from Embraer and the *Instituto Tecnológico de Aeronáutica* (ITA) of Brazil, conducted extensive CFD studies in an effort to characterize the inlet vortex problem in greater detail than previously done. They performed 3-D simulations on a DLR-F6 nacelle, meshed with nearly 5 million elements, and ensured y^+ values were kept below 1 for accurate boundary layer resolution. The authors proved what was already known from experiments: viscous effects are essential for inlet vortex formation. They accomplished this by

conducting two identical tests, an inviscid and a viscous case, with flow conditions such that an inlet vortex was expected to form. Results revealed that while the viscous simulation contained an inlet vortex, the inviscid did not.

In a later publication, Trapp and Girardi (2012) conducted further CFD tests, comparing simulations that had combinations of no-slip and slip wall boundary conditions, and concluded that the vorticity created on the nacelle external walls contributes more to the inlet vortex intensity than does vorticity produced on the ground, as was hypothesized by De Siervi *et al.* (1982). Although the primary vorticity source for inlet vortices was demonstrated to be the nacelle external walls, ground boundary layer vorticity was also convected into the inlet vortex, adding to its strength.

For both high and low velocity ratios, De Siervi *et al.* (1982) previously suggested that the trailing vortices formed were blown infinitely downstream, away from the engine. However, CFD results by Trapp and Girardi suggest that trailing vortices are in fact composed of two rotating flows: an inner core flow and an outer flow, as illustrated in Figure 2.13, showing the outer flow streamlines in white and the inner core flow in blue.

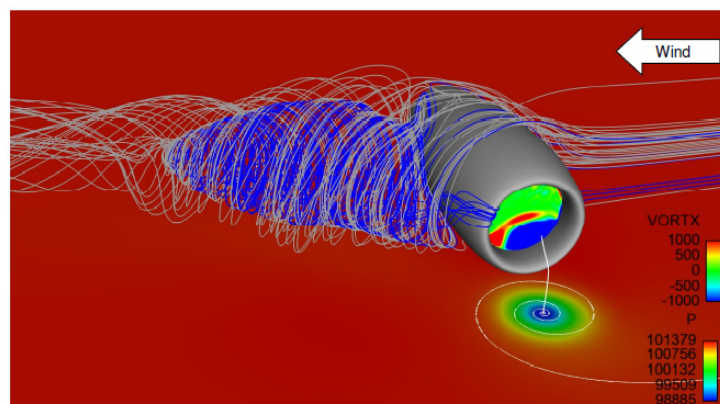


Figure 2.13 Particle traces that form the trailing vortex (Trapp and Girardi, 2012).

The trailing vortex's outer flow is blown infinitely downstream, as initially proposed by De Siervi *et al.* (1982). On the other hand, the trailing vortex's inner core flow is sucked back into the inlet.

Work has also been conducted on full aircraft models to study the interaction of the inlet vortex system with the plane fuselage. Vunnam and Hoover (2011) modeled a business jet fuselage and rear-mounted engine nacelle, modeling fan blades and a one-stage compressor. A mesh of more than 9 million elements was created, with y^+ values less than 200. Under crosswind conditions, an inlet vortex was observed, which attached itself to the upper surface of the wing, and was accompanied by a trailing vortex attached to the fuselage (Figure 2.14). A flow separation region was also detected on the upwind side of the inlet. Fan face distortion was calculated and compared to experimental values for the particular aircraft and engine used. It was found that CFD-predicted distortions were 10 times greater than the experimentally calculated ones. The authors attributed this to the insufficient number of prism layers comprising the boundary layer mesh.

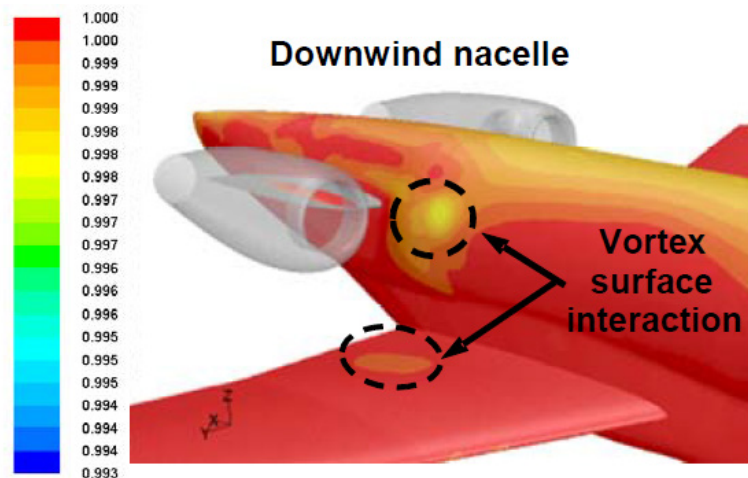


Figure 2.14 CFD results showing pressure contours on wing and fuselage surfaces due to a crosswind on aft-mounted engines of a business jet.

2.7 Vortex prevention methods

There have been many devices patented that attempt to prevent or eliminate the inlet vortex. However, none have been successful in developing a technique applicable to all wind scenarios. The first inlet vortex prevention system to be put into commercial service was the Blow-away Jet used on the DC-8 in the late 1950s and early 1960s, as illustrated in Figure 2.15 (Klein, 1959).

The concept behind this design was to blow high-pressure compressor-bled air onto the ground in the vicinity of where the vortex stagnation point would form. As the air impinged on the stagnation point region close to the ground, it weakened the vortex, which then tended to disappear. This technique, however, failed to account for the unsteadiness of wind and suction speeds, which themselves affect the location of the stagnation streamline. Thus, precise impingement was not always achieved. Moreover, the jet caused severe ground impingement. This caused debris to be kicked up into the air and entrained in the airflow, provoking the exact damage it was intended to avoid (Trapp and Girardi, 2010).

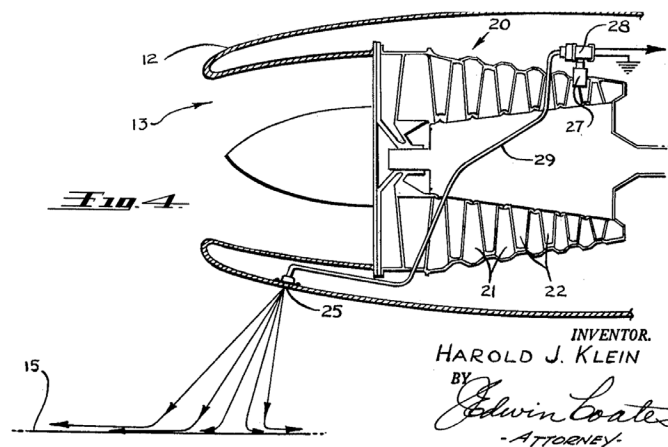


Figure 2.15 Blow-away jet system for inlet-vortex avoidance, image from the patent of Klein (1959).

An ingenious idea patented by Cox and William (1969) is shown in Figure 2.16. The authors believed that extending a platform out in front and beneath the inlet during ground operations would prevent a ground-to-inlet vortex from forming between the inlet and the ground plane, and thus decrease chances of FOD. However, inlet vortices still found their way into the engine by going around the device or attaching to the platform itself. The platform did help prevent foreign object ingestion to a small degree, but it did not prevent fan face distortion.

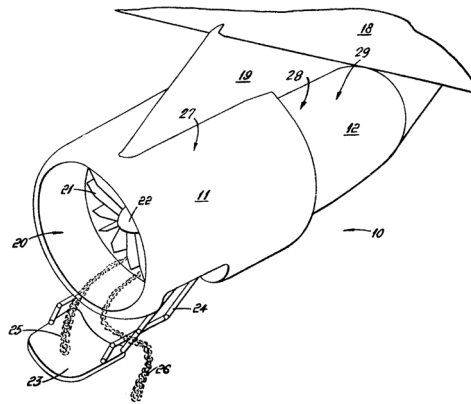


Figure 2.16 Cox and William (1969) system for inlet vortex attachment.

More recently, and with the aid of CFD, active flow control methods have been developed that successfully weaken and subsequently eliminate the vortex. Smith (1970) developed a pulsed actuation system, which consists of two air-ejecting, angled nozzles mounted under the lip. These were deployed under low-speed and high engine power settings. The intermittent high-frequency ejection provides sufficient turbulent mixing to avoid the formation of a coherent vortex (Shmilovich and Yadlin, 2011). There are two major downsides to using this technique, however: (1) it is activated once the vortex is already present, making it a vortex alleviation technique, rather than a vortex prevention technique. (2) There is significant air flow impingement on the ground, which will inevitably kick up debris, increasing risk of FOD.

A sprinkler jet system was developed and tested using CFD by Shmilovich and Yadlin (2006), which acted in a similar fashion to the system proposed by Smith (1970), but consisted of a single swiveling nozzle under the inlet lip. This technique was successful in alleviating the vortex once it formed, but it also impinged on the ground, and over an even greater area than the device by Smith (1970). Hence FOD was a concern with this method as well.

These modern techniques have not been implemented on aircraft to the best of this author's knowledge due to their limited operating range and effectiveness. Current inlet vortex prevention strategies are all operational, strictly limiting the aircraft speed and engine thrust combinations to safe, vortex-free conditions.

2.8 Conclusions

In this chapter an overview of the inlet vortex problem is presented, outlining the basic mechanisms by which it forms, the observations made by investigators and their conclusions. Engine performance and the threat of FOD are discussed. It is shown that in order for the inlet vortex to exist, there must be a source of vorticity. Researchers found that the primary source of this vorticity is the inlet nacelle boundary layer. The ground boundary layer created by the approaching crosswind flow, as well as ambient vorticity, are not necessary for inlet vortices to form but do increase their strength. Experimental and numerical results revealed that a stagnation point is indeed required near the ground plane for an inlet vortex to form. Once a stagnation point exists, the inlet suction stretched the vortex filaments, pulling the inlet vortex upwards and into the inlet.

A description of the two non-dimensional ratios responsible for characterizing the inlet vortex flow field is also presented. The literature reveals that an inlet vortex only forms when the inlet capture area overlaps with the ground plane, and that in these cases a trailing vortex

accompanies the inlet vortex. This corresponds to a high velocity ratio scenario. In the case of a low velocity ratio, two trailing vortices were observed and no inlet vortex formed. A correlation between these two ratios was developed based on data-fitting of available experiments, revealing the conditions under which an inlet vortex will form.

The inlet vortex problem is still not well understood despite having been investigated for nearly six decades. In particular, the unsteady behavior as the vortex transitions from trailing to inlet vortex is yet to be characterized and described. Vortex prevention techniques have been studied and even patented, however none have proven successful at eliminating the vortex under all crosswind conditions. In order to develop an adequate solution to the problem, a greater understanding of the inlet vortex formation mechanism is necessary. The work presented in this research project addresses one aspect of the formation process, studying its transience for the very first time. Numerical techniques have seen considerable improvements over the course of the past 20 years and are thus a valuable tool for investigating fluid dynamics problems. The research contained here used a transient ANSYS FLUENT model to study the inlet vortex formation.

Chapter 3. Numerical Methods

3.1 Introduction

This chapter describes the steps involved in creating the jet engine nacelle model for the present CFD analysis, from geometry and domain considerations, to case setup, boundary condition determination and data post-processing. A thorough description of the case studied in this research is also presented, of which results are presented in Chapter 6.

3.2 Scaled jet engine model and domain

The geometry used in this research was that of a cylinder representing the jet engine enclosed by a rectangular box representing the flow field. The cylinder was chosen as a 7.5% scale model of a real jet engine, with scaled inner and outer diameters of 16 and 20cm, respectively. It contained an elliptical leading edge, with a 2cm semi-major axis and a 2:1 major-to-minor axis ratio. The length of the cylinder was 100cm. The fan face distance to the leading edge was set to 7cm. Figure 3.1 shows a schematic of the engine model, with dimensions in centimeters, followed by Table 3.1 summarizing the model sizing parameters. No rotating turbomachinery components were modeled in this research due to their complexity.

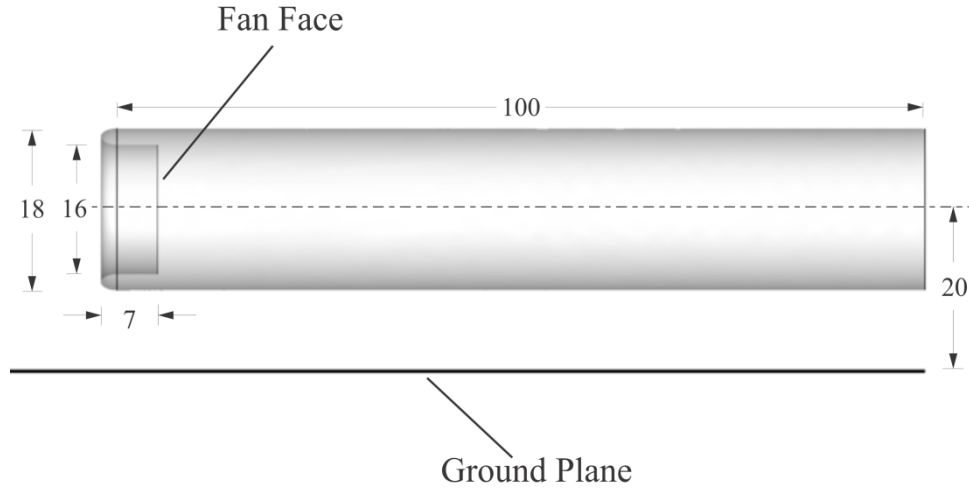


Figure 3.1 Dimensioned sketch of jet engine model, in centimeters.

Table 3.1 Summary of inlet dimensions.

Parameter	Dimension [cm]
Inside diameter, D_i	16
Outer diameter, D_o	20
Length	100
Fan-face to LE distance	7
LE thickness	2
LE length	2

The cylinder described above was enclosed by a rectangular box representing the surrounding air, with dimensions 600cm (X) x 220cm (Y) x 400cm (Z), as shown in Figure 3.2. The height of the cylinder axis from the ground plane was fixed at 20cm, which also fixed the non-dimensional ratio $H/D_i = 1.25$. ANSYS User's Guide recommends that the enclosing boundaries be at a minimum distance of approximately 20 times the characteristic length of the object under study, in this case, the inner diameter of the inlet. This way, any numerical errors

occurring near the boundaries are far enough away from the object that it does not affect the physics of the flow of interest.

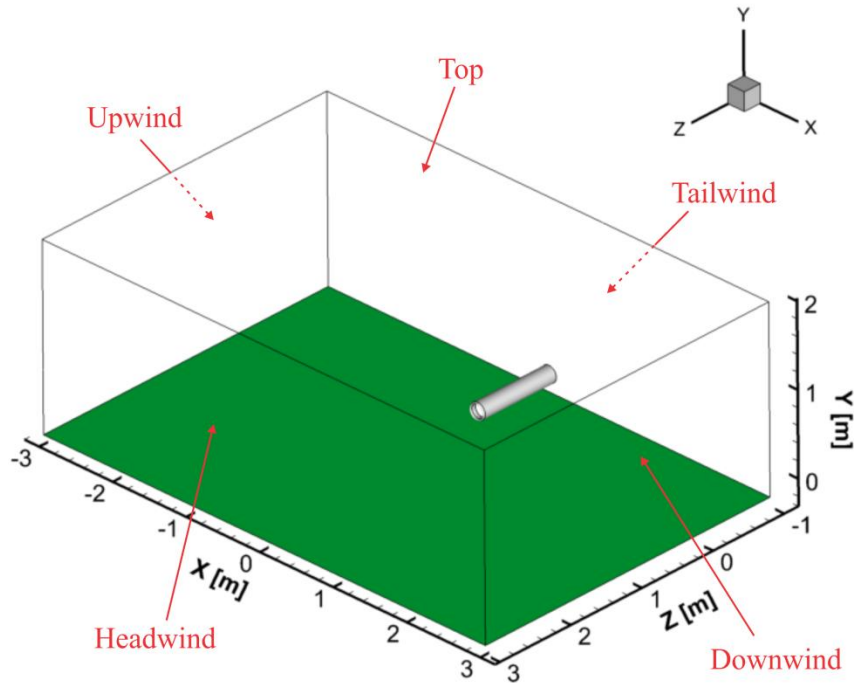


Figure 3.2 Dimensioned domain enclosing jet engine model, with labelled faces and coordinate system.

ANSYS 14 Design Modeler was used to construct the 3-D geometry. A sketch of the cylinder was drawn and revolved about the Z axis and subsequently frozen. The enclosure was then created and frozen as well. A Boolean operation was performed to remove the solid body corresponding to the cylinder, leaving only the surrounding air inside the domain. The coordinate system chosen was such that positive X points in the direction downwind and parallel to the crosswind, positive Y points upwards, normal to the ground plane, and positive Z points out of the inlet. Figure 3.2 shows the domain and XYZ coordinate system described, as well as the names assigned to each of the domain surfaces, with the ground plane highlighted in green. The

origin of the domain was placed coincident with the inlet center axis (Z axis) and located 5cm behind the lip edge.

3.3 Mach and Reynolds number scaling

The research presented here aimed to model a jet engine with an inlet mass flow rate representative of take-off conditions and under the influence of a crosswind. It is known from the literature that representative Mach and Reynolds numbers for this scenario are about 0.55 and 10^7 , respectively (De Siervi *et al.*, 1982). However, due to the 7.5% scaling factor adopted, it was impossible to achieve both of these numbers simultaneously. To illustrate, take the definitions of both Mach and Reynolds numbers at the fan face of a full-scale jet engine:

$$M_i = \frac{V_i}{\sqrt{\gamma RT_i}} \quad (3.1)$$

$$Re_{D_i} = \frac{\rho_i V_i D_i}{\mu} \quad (3.2)$$

When the inner diameter of the full-scale jet engine is multiplied by 0.075 (the scaling factor), the representative inlet suction speed needs to be multiplied by $\frac{1}{0.075} \cong 13$ to match the Reynolds number of the scaled inlet to the full-scale one. The Mach number would then be hypersonic and therefore not desirable.

However, if the inlet velocities were to be matched, the Mach numbers would also be matched (assuming standard air properties are left unchanged). Consequently, the scaled Reynolds number would be smaller by a factor of 0.075. For the purposes of this research, the Mach numbers were matched to 0.55 and the model Reynolds number was of the order of 10^6 .

3.4 Mesh Generation

This section describes the features of the mesh developed for the domain illustrated above.

3.4.1 Meshing setup procedure

ANSYS 14 Mesher was used to mesh the geometry illustrated in Figure 3.2. A patch-conforming method was used, creating an unstructured tetrahedral mesh. The advanced size function was set to “On: Proximity and Curvature” with a coarse relevance center. In order to capture the near-wall boundary layer effects on the engine nacelle model, program-controlled automatic inflation was applied to the surfaces of the inlet lip and inlet outer and inner walls. This inflation method generated structured wedge elements on these surfaces, which were smoothed as they transitioned to the surrounding tetrahedral elements. The method used was total thickness, with 30 inflation layers, a growth-rate of 1.1, and a maximum thickness of 0.3cm.

3.4.2 Boundary layer considerations

Since the representative Mach number for the inlet suction flow was known to be around 0.55 (De Siervi *et al.*, 1982), the air would approach transonic speeds when turned around the inlet lip. A separation region will also form on the inside of the windward lip due to this turned flow. Therefore, small-enough inflation layers were needed to capture these flow phenomena.

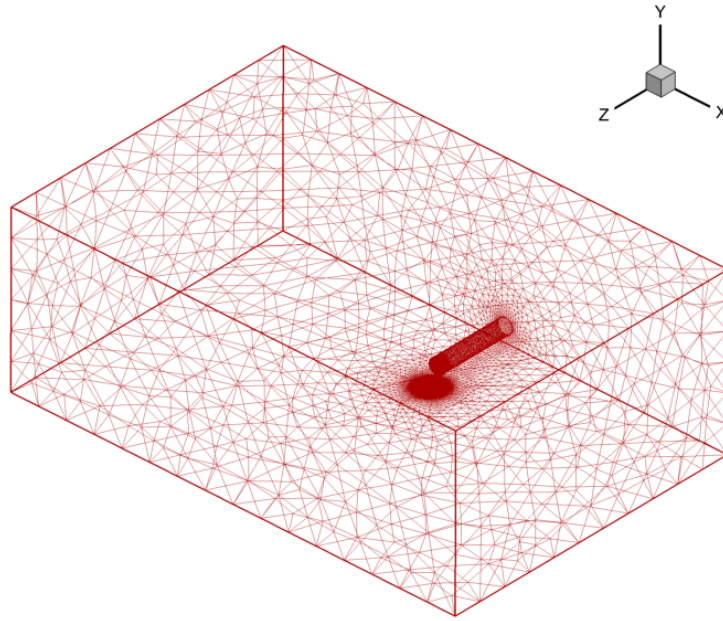
The parameter that describes the degree of refinement of the first inflation layer is the dimensionless wall distance, y^+ , defined as:

$$y^+ = \frac{u^* y}{\nu} \quad (3.3)$$

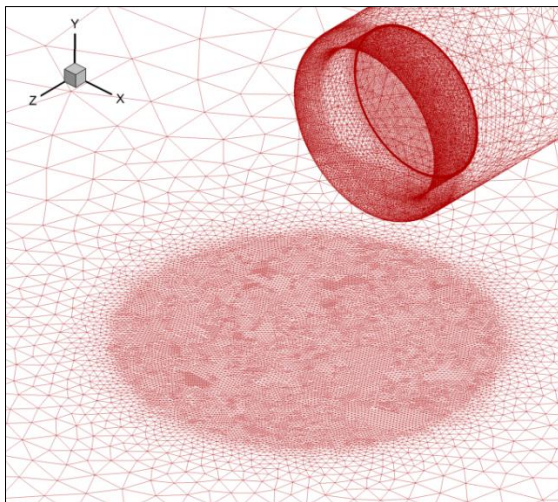
where $u^* = \sqrt{\frac{\tau_w}{\rho}}$ is the friction velocity at the nearest wall (which depends on the wall shear stress and air density near the wall), y is the distance to the nearest wall (or height of the first inflation layer), and ν is the local kinematic viscosity of the air. For accurate boundary layer resolution within the viscous sub-layer, the y^+ must be less than 1. This condition was satisfied in all cases simulated in the present research.

3.4.3 Mesh refinement considerations

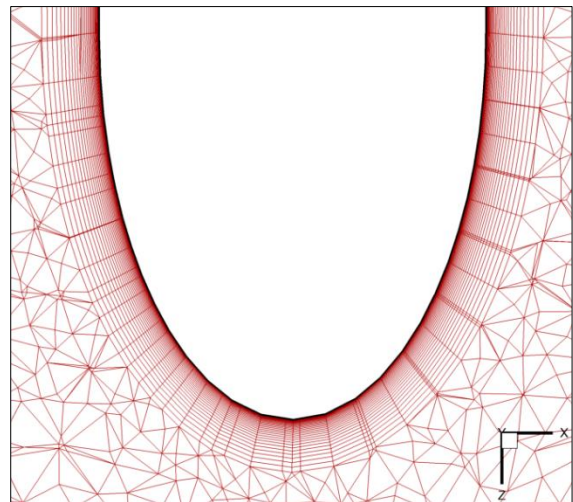
Additionally, in order to accurately visualize the vortex core flow, a “bubble” region of more highly resolved mesh was defined where the inlet vortex was expected to form. This region consisted of a spherical hemisphere 36cm in diameter centered on the ground plane and along the Z axis. A local body sizing mesh refinement was applied to the bubble with a maximum element size of 0.3cm. Based on experimental and numerical results in the literature, the vortex core was expected to be only a few centimeters in diameter, depending on flow conditions and geometry. Therefore, the 0.3cm maximum element size was chosen to accurately capture the ground stagnation point, the vortex’s 3-D profile, and any ground-attachment location shift it may undergo. Element size functions were also applied to the inlet body, lip, and fan face for accurate detection of vortex ingestion and flow separation areas, with a maximum element size of 0.2cm. Figure 3.3 shows the full meshed domain and close up views of the bubble region and inlet inflation layers on the inlet lip. The mesh contained approximately 5.6 million elements. Since this number exceeded the ANSYS academic license limit of 512 000, an ANSYS research license was used.



(a)



(b)

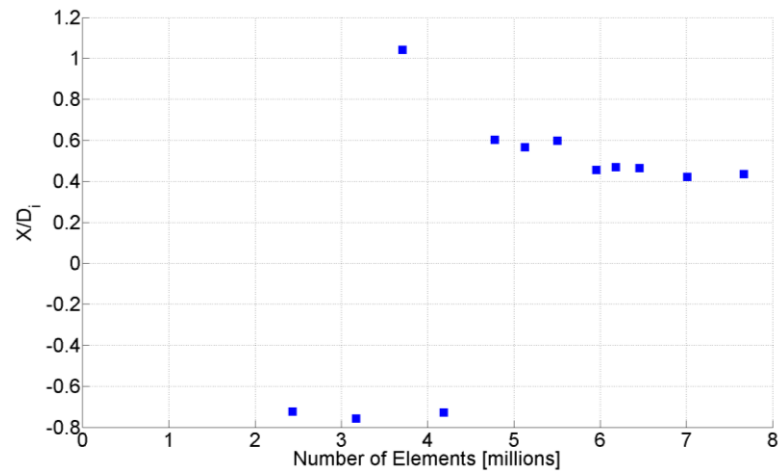


(c)

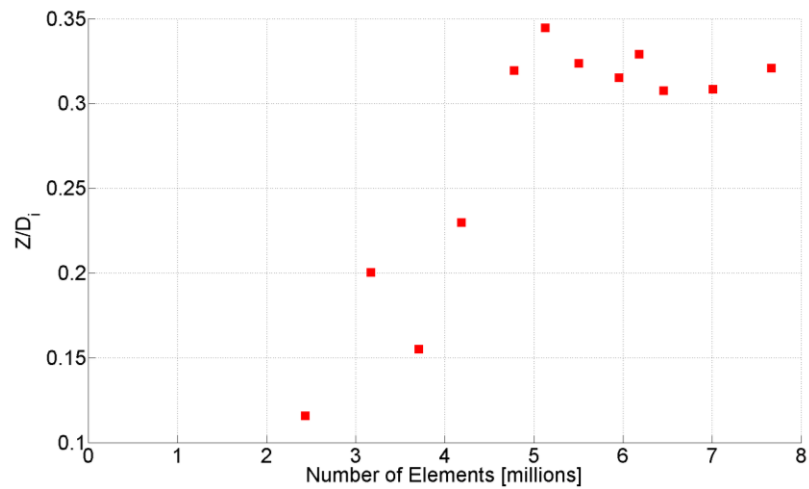
Figure 3.3 (a) Meshed domain, (b) close-up view of refined “bubble” region, and (c) close-up view of lip inflation layers.

3.4.4 Mesh sensitivity study

A mesh sensitivity study was conducted to determine the coarsest mesh that could be used while still obtaining accurate results. This was accomplished by performing 12 CFD tests with the above mesh characteristics, but at different levels of refinement within the bubble region. The metric used for comparison between meshes was ground attachment X and Z coordinates of the vortex core. The results are plotted below in Figure 3.4.



(a)



(b)

Figure 3.4 Mesh sensitivity plots showing vortex (a) X location and (b) Z location.

Due to the large number of tests performed and the time constraint of this research project, all mesh sensitivity tests were conducted assuming steady-state and an identical number of iterations. The results show that at approximately 5.5 million elements, the vortex ground attachment location coordinates seem to not vary widely anymore. Thus, a slightly more refined mesh containing around 5.6 million elements was chosen for use in this research (shown in Figure 3.3).

3.4.5 Mesh quality assessment

The quality of the mesh generated was monitored using ANSYS 14 mesh metrics, specifically skewness and orthogonal quality. Skewness values, in general, range from zero to one, where in 2-D zero corresponds to an equilateral triangular cell (ideal case) and one to a completely degenerate cell (worst case). Degenerate cells are characterized by nodes that are nearly coplanar, or collinear in 2-D. Orthogonal quality values also range from zero to one, but with zero being a completely degenerate cell and one corresponding to an equilateral triangular cell. For the mesh used in this research and depicted above, the skewness average and maximum values were 0.2 and 0.79, respectively, with less than 0.004% of cells having skewness above 0.75. The orthogonal quality average and minimum values were 0.88 and 0.23, respectively, with less than 0.001% of cells below 0.25. Therefore, the quality of the mesh created was deemed good and no modifications were needed.

3.5 CFD setup specifications

This section outlines the specifications of the CFD setup in ANSYS FLUENT, clarifying solver setup inputs and procedure.

3.5.1 General ANSYS FLUENT setup characteristics

ANSYS FLUENT 14 was the commercial CFD software chosen to solve the complete Navier-Stokes equations. The mesh generated in ANSYS 14 was exported as a *.msh* file and subsequently imported into ANSYS FLUENT. A double-precision solver was used with up to 40 parallel processors employed, depending on server CPU availability. Since the desired take-off Mach number was above 0.3, a compressible model was chosen, which required solving the energy equation, in addition to the continuity and momentum equations. To accomplish this, a density-based solver was selected and the air density specification was modified to assume an ideal gas model.

The main research objective of this thesis was to study the unsteady formation process of the inlet vortex. To accomplish this, a transient model was required so that the flow field could be interrogated at different time steps throughout the simulation.

For the given Mach number and engine inner diameter, turbulent flow was expected in the vicinity of the inlet. Thus, an adequate turbulence model was required. After extensive research into the many turbulence models available in ANSYS FLUENT, the SST $k-\omega$ model was chosen for its greater accuracy in predicting adverse pressure gradient boundary layer flows and separation in external aerodynamics problems, and for its lower computational cost compared to Reynolds Stress Models (RSM). The ANSYS FLUENT default constants for the turbulence equations were used, as was recommended by the ANSYS FLUENT user's guide.

3.5.2 Boundary conditions determination and setup

As with any partial differential equation, to solve the full 3-D Navier-Stokes equations required imposing boundary conditions at each of the domain faces (or zones). Table 3.2 relates the type of boundary condition imposed to each of the zones present in the model.

Table 3.2 Boundary condition selection for each domain zone.

Surface (or zone)	Boundary Condition type
Ground	No-slip wall
Inlet lip	No-slip wall
Inlet body	No-slip wall
Fan face	Pressure outlet (with target mass flow rate)
Upwind	Pressure far-field
Downwind	Pressure outlet
Headwind	Pressure outlet
Tailwind	Pressure outlet
Top	Pressure outlet

Following is a detailed description of the calculations involved in determining each of the boundary condition inputs at each zone, along with all other inputs. Reference conditions were picked such that freestream ambient pressure was 101,325Pa at 288K. C_p and γ were assumed to be constants equal to 1006.43J/kg.K and 1.4, respectively.

Ground, inlet lip, and inlet body

A no-slip wall BC was assigned, specifying the temperature of 288 K in the thermal tab.

Fan face

A pressure outlet BC was assigned, with a target mass flow rate.

Since the desired $M_i = 0.55$, using the compressible flow table the temperature and pressure ratios were found to be

$$T/T_o = 0.9430 \quad (3.4)$$

$$p/p_o = 0.8142 \quad (3.5)$$

Assuming a stagnation pressure of 101,325Pa, the static pressure was calculated to be 82,499Pa. In the same way, assuming a static temperature of 288K, the stagnation temperature was found to be 305.408K. This value was used as the backflow total temperature under the thermal tab.

Using the compressible flow table once again,

$$\frac{V_i}{\sqrt{C_p T_o}} = 0.3378 \quad (3.6)$$

$$\frac{\dot{m}\sqrt{C_p T_o}}{A p_o} = 1.0208 \quad (3.7)$$

Therefore, the inlet suction speed at this Mach number was 187.28m/s and the specified target mass flow rate 3.751kg/s. Since a compressible model was used, FLUENT did not allow the specification of a velocity boundary condition. Thus, the inlet suction speed will actually vary according to the calculated density after each iteration. Using the specified mass flow rate, the inlet suction area, and the calculated density, ANSYS FLUENT estimates the corresponding velocity.

For the turbulence specification method, turbulence intensity and turbulent viscosity ratio were used, with values set to 10% and 9, respectively. These were based on recommendations from the ANSYS FLUENT 14 User's Guide. The backflow direction was specified as normal to the boundary.

Upwind

A pressure farfield BC was specified for the upwind zone with pressure equal to ambient, 101,325Pa. The Mach number of the approaching flow was determined by the desired conditions, using the non-dimensional groups described previously. For an $H/D_i = 1.25$, according to De Siervi *et al* (1982), the empirical correlation

$$V_i/V_\infty = 24 \times (H/D_i) - 17 \quad (3.8)$$

yielded a critical velocity ratio of 13. The case studied in this research corresponded to that of an inlet in a crosswind, with a step-change in wind speed. This was accomplished by modifying the wind speed while keeping the inlet conditions unchanged. The initial velocity ratio chosen was 18 and the final 25, with the higher crosswind speed at the start of the run. These ratios were sufficiently higher than the critical ratio of 13 that a single inlet vortex was expected to form at steady-state conditions. From the calculated V_i and desired ratios, the freestream velocities were found to be 10.4m/s and 7.491m/s. Using the following equation,

$$T_o = T + \frac{V_\infty^2}{2C_p} \quad (3.9)$$

the temperature required to stagnate the air was 288.054K and 288.028K, respectively, which were set in the thermal tab. Thus, T/T_o was found to be 0.9998 and 0.9999, respectively, and Mach numbers were then determined from the compressible flow table to 0.0306 and 0.022 for the initial and final setups.

Additionally, the turbulence specification method used was turbulence intensity and turbulent viscosity ratio, with values set to 0.1% and 2, respectively.

Downwind, headwind, tailwind, and top

Pressure outlet boundary conditions were applied, using a static pressure of 101,325Pa and turbulence intensity and turbulent viscosity ratio of 10% and 9, respectively. Backflow total temperature was set to 288.028K.

3.5.3 Further boundary condition considerations

It is important to note that the target mass flow rate specified in the fan face boundary condition was incrementally increased in the first 0.001s of simulation, until it reached the desired value of 3.751kg/s. The reason for this was that if the simulation was initialized with the full value of the mass flow, it would diverge very early on in the solution process due to excessive temperature changes. Thus, making the physical property changes gradual with time allowed for a more stable solution process and prevented issues related to divergence.

3.5.4 Solution methods specifications

Once boundary conditions were set, the solution methods were specified. An implicit formulation was used, with Roe-FDS flux type (default). The spatial discretization was least squares cell based, recommended by ANSYS FLUENT, along with first order upwind for the flow and turbulence parameters, and first order implicit for the transient formulation. The high order term relaxation box was checked on. Once the initial instabilities in the solution disappeared, the spatial discretization for the flow and transient formulation were switched to second order for more accurate, reliable results. Default values were used for the solution controls parameters.

3.5.5 Residuals, monitors and solution convergence

Scaled residuals were used as the primary means of monitoring convergence and stability of the solution at each time step. Since an implicit time formulation was used, residuals for the

continuity, energy and turbulence equations, as well as for X, Y and Z velocity components were calculated at each iteration. This way, convergence could be assessed at each time step. Surface monitors at specific zones in the domain were also set up to aid in the convergence monitoring process. Table 3.3 contains the surface monitor parameters used for the relevant zones.

Table 3.3 Monitors used in ANSYS FLUENT.

Zone	Surface Monitor Parameter
Upwind	Area-weighted average of static pressure and velocity
Fan face	Area-weighted average of Mach number, velocity, and static pressure
Near-ground plane	Vertex-minimum of static pressure

The near-ground plane mentioned above is a plane defined just above and parallel to the ground. Due to the no-slip wall BC on the ground, velocity-related quantities were zero on the surface. Thus, in order to visualize the flow topology on the ground, a new surface needed to be created. The study done by Murphy and MacManus (2011) used a measurement plane at a non-dimensional height from the ground given by

$$\frac{h}{D_t} = 0.083 \quad (3.10)$$

For this report, the highlight diameter of the scaled model engine was 17cm, and so, equation (3.10) yields a height of the near-ground plane above the ground of 1.411cm, which is -18.589cm in Y, relative to the origin

In all post-processed data shown in this report, the near-ground plane was at exactly this distance from the origin. A vertex-minimum of static pressure monitor was chosen because the inlet vortex is characterized by a low-pressure region inside vortex core. Thus, an inlet vortex

could be detected during a CFD simulation simply by studying a time history of the minimum pressure on this plane.

3.5.6 Solution initialization and iteration setup

The simulation was initialized using the hybrid initialization mode, with the external-aero favorable settings box checked. Initial time step size was 10^{-5} s since the bubble region contained elements that were small, therefore requiring a small time step size. Selecting a small time step size prevented excessive changes in the physical properties of the flow and a consequent solution divergence, allowing for smaller changes in the flow physics and sufficient time for the domain to adapt to these flow changes. Once the initial numerical instabilities had subsided, the time step size was increased to 10^{-3} s. However, it was necessary to increase the number of iterations in each time step to ensure residuals were sufficiently low. Initially, the number of iterations per time step was 100, but this number was increased to 300, with residual levels in the range of 10^{-3} to 10^{-4} . Ideally, at least 2000 iterations would have been needed per time step to allow the energy equation residuals to decrease to 10^{-5} . Since the mesh used was very large and with the time constraints for completion of this research work, having this number of iterations was impractical. Therefore, a small sacrifice to the accuracy of the data was accepted in favor of decreasing the computational time, and so for the purposes of this research, the solution was deemed converged once the residuals were between 10^{-3} and 10^{-4} .

3.6 Case description

The case presented in Chapter 6 of this report was identical to the geometry and domain described in sections 3.2 and 3.3, with boundary conditions, setup, and procedures applied as indicated in section 3.5. The velocity ratio (V_i/V_∞) imposed was initially 18 and later increased to

25 after the step-change in wind speed, for a non-dimensional height ratio $\left(H/D_i\right)$ of 1.25. The total flow time was 1.1474s.

3.7 Summary

This chapter describes the process involved in creating a CFD model using ANSYS FLUENT 14 to simulate a scaled jet engine under a crosswind. The mesh created was unstructured and contained 5.6 million tetrahedral and wedge elements. Mesh quality was monitored and $y+$ values were kept below 1 for accurate boundary layer resolution. The CFD setup used was 3-D u-RANS, compressible, and turbulent.

Chapter 4. Data Processing Methodology

This chapter describes the data processing methodology used to post-process and visualize numerical results, in particular the estimation of a fan face distortion coefficient, the DC_{60} , and circulation of vortices present at each time step. To accomplish this, ANSYS FLUENT's autosave function was activated during simulations, saving data (.dat) files every two time steps and case (.cas) files whenever boundary conditions or solver setup were modified. ANSYS FLUENT case files contain information pertaining to the domain zones and CFD solver setup, including boundary conditions. ANSYS FLUENT data files, on the other hand, contain the physical quantities of interest such as velocities, pressures and vorticities at each node or cell center at a particular time step.

4.1 Fan face distortion coefficient, DC_{60}

A non-dimensional parameter often used to quantify pressure losses at the fan face is the DC_{60} , defined previously in equation (2.2) as:

$$DC_{60} = \frac{P_i - P_{60}}{q_i}$$

where P_i is the area-weighted average of stagnation pressure at the fan face, P_{60} is the area-weighted average of stagnation pressure at the worst 60-degree sector on the fan face, and q_i is the local dynamic pressure at the fan face. The worst 60-degree sector is defined as the region containing the highest amount of flow distortion, quantified by the lowest area-weighted average of stagnation pressure.

To evaluate this coefficient, cell-centered, comma-separated ASCII data files were exported directly from ANSYS FLUENT containing XYZ coordinates, total pressure, axial velocity, density and Z-face grid cell area values at the fan face. These were imported into MATLAB R2012a and a script was written to estimate the DC_{60} and the location of the worst 60-degree sector.

Stagnation pressure contours at the fan face revealed the ingestion location of all vortices observed as well as the presence of a large separation region on the windward lip. This region was marked by significant pressure losses, much lower than the ones observed at the vortex ingestion points. This led to a problem when computing the full fan-face DC_{60} , since the separation region skewed the 60-degree sector away from the vortex ingestion point. Thus, in these cases, the DC_{60} did not describe the impact of the inlet vortex on fan face distortion. A solution to this problem was to force the inclusion of the ingestion location within the 60-degree sector. To accomplish this, pressure contours at the fan face were examined at each time step using the probe tool in Tecplot 360 2010 to determine the approximate center of the core. These were then converted into polar angles, fully defining the 60-degree sector and enabling the calculation of the DC_{60} that includes the inlet vortex distortion. However, the values obtained for the coefficient in this way came out negative, implying that the inlet vortex was actually reducing fan face distortion. The reason for this was determined by studying the DC_{60} definition above. Since P_i is an area-weighted average of the stagnation pressure across the full fan face, the

presence of a large lip separation region with considerable pressure losses drove this value down. Because the stagnation pressure of the ingested vortex was not nearly as low as in the separation region, the numerator became negative in the equation. Once again, it was clear that these DC_{60} values were not adequately characterizing the flow at the fan face for a worst sector defined around the vortex. Therefore, a modified DC_{60} parameter was proposed which used P_i and q_i as the stagnation and dynamic pressures, respectively, defined at the center of the fan face ($X = Y = 0$, $Z = -0.05 \text{ m}$) and away from the separation region, rather than as aero-averaged values. This yielded positive distortion coefficients that were not influenced by the windward lip separation pressure loss. This modified DC_{60} is referred to hereafter as the modified inlet vortex DC_{60} .

In summary, three DC_{60} estimates were calculated and compared at each time step: one for the full fan face (including the separation region), one for only the ingested vortex location, and a modified DC_{60} estimated for the ingested vortex location and based on the fan face center point data.

4.2 Circulation, Γ

In order to quantify the strength of vortices present and compare them to each other at each time step, their circulation was computed. Circulation, which is a dimensional quantity characterizing the strength of a vortex or swirling flow, is defined as

$$\Gamma = \oint \vec{V} \cdot d\vec{l} \quad (4.1)$$

where \vec{V} is the velocity vector and the integral is carried out along a closed loop in a given plane. Applying Stokes' theorem, the equation becomes

$$\Gamma = \iint (\nabla \times \vec{V}) \cdot d\vec{A} \quad (4.2)$$

which should now be integrated over an area A on that plane. The curl of the velocity vector is defined as the vorticity vector, which dotted with the infinitesimal area vector becomes the vorticity normal to the area element. Applying a numerical approximation to the equation described, the final circulation equation becomes

$$\Gamma = \iint \omega_{normal} dA \approx \sum_{i=1}^n \omega_{normal}(i) A(i) \quad (4.3)$$

where i ranges from one to the number of elements on the surface under investigation.

To evaluate the circulation around a vortex, circular zones were created in Tecplot based on a method described by Murphy (2008). ANSYS FLUENT data and case files were read into Tecplot and the vorticity vector components $\langle \omega_x, \omega_y, \omega_z \rangle$ were calculated. The probe tool was then used to determine the approximate center of the vortex core. The coordinates of this center were used to create a circular zone or disk around the vortex, as illustrated in the figure below, over which the area in the circulation equation could be defined. Figure 4.1 shows two circular zones on the near-ground plane, located around each of the vortex cores, for a case when two inlet vortices exist.

To create the disk, Tecplot required a specification of the number of equidistant radial and circumferential subdivisions, known as I_{max} and J_{max} , respectively. All circular zones of radius r_{max} obeyed the following ratios, suggested by Murphy (2008) and corrected by the author:

$$\frac{J_{max}}{I_{max}} = 1.74 \quad (4.4)$$

$$\frac{r_{max}D_i}{I_{max}} = \frac{1}{6} [cm^2] \quad (4.5)$$

The structural quadrilateral mesh developed was comprised of $I_{max}(J_{max} - 1)$ nodes using the ratios given above. Data was linearly interpolated from the domain onto the zone to generate vorticity contour, such as that shown in Figure 4.1.

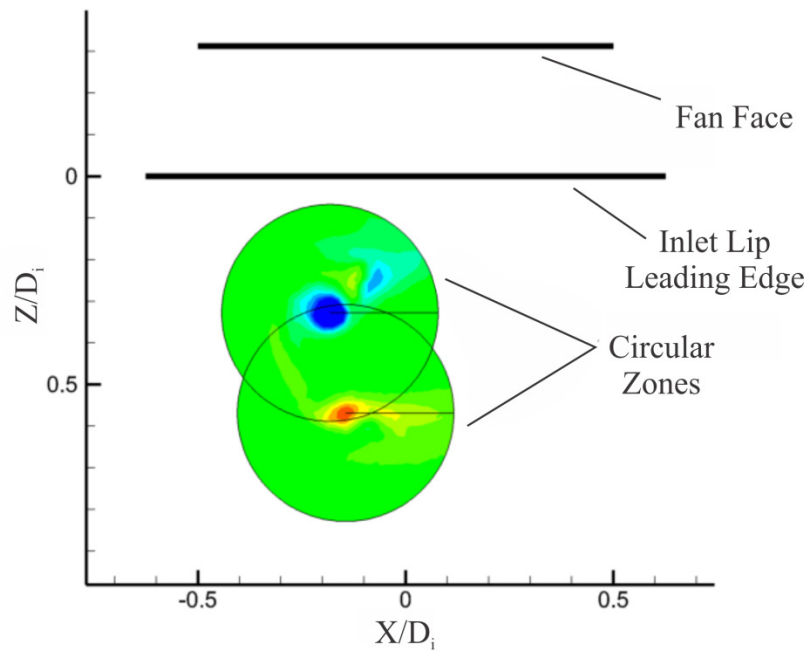


Figure 4.1 Tecplot circular zones created on near-ground plane ($Y = -0.18589$ m), showing y-vorticity contours.

The out-of-plane vorticity and planar coordinates for the disk were then exported in an ASCII format and read into MATLAB. A script was written to calculate circulation due to negative and positive vorticity individually, as well as a total circulation, which was defined as the sum of the absolute circulation of the positive and negative components.

$$\Gamma_{Total} = |\Gamma_+| + |\Gamma_-| \quad (4.6)$$

The reason for calculating three separate circulation values was that sometimes, when multiple vortices were present, the disk zone would contain two or more vortices rotating in opposite directions (with opposite vorticity signs), as in the case shown in Figure 4.1. Since the disk radius was to be kept fixed for all scenarios on a given plane so a time history could be developed using the same area, the vorticity contained in each vortex needed to be assessed individually. Therefore, separating into positive and negative components was found to be a viable solution. Additionally, one zone might also overlap with another zone on the same plane, in the case of multiple vortices. Again, separating the positive circulation from the negative and making note of the direction of rotation of each individual vortex allowed the total circulation to be computed without double-counting circulation in the case of multiple vortices.

The method used to compute the area elements in the circulation equation is defined by the equations below:

$$\left\{ \begin{array}{l} A(1) = \frac{\pi}{J_{max}} \left[\frac{R(2)}{2} \right]^2, \text{ for } i = 1 \\ A(i) = \frac{\pi}{J_{max}} \left[\left(\frac{R(i+1) - R(i)}{2} + R(i) \right)^2 - \left(\frac{R(i) - R(i-1)}{2} + R(i-1) \right)^2 \right], \text{ for } 2 \leq i < I_{max} - 1 \\ A(I_{max}) = \frac{\pi}{J_{max}} \left[R(I_{max})^2 - \left(\frac{R(I_{max}) - R(I_{max} - 1)}{2} + R(I_{max} - 1) \right)^2 \right], \text{ for } i = I_{max} \end{array} \right. \quad (4.7)$$

where $R(i)$ is the distance from node i to the center of the disk. These equations were derived from the basic circumferential segment area equation defined for a radius r and sector angle θ , in radians:

$$S = \frac{r^2\theta}{2} \quad (4.8)$$

Each infinitesimal area element contained two nodes, with the exception of $A(1)$ which contained only one centered at the origin. The out-of-plane vorticity at the center of each infinitesimal area element was approximated by the average of the vorticity on these two nodes.

A disk radius sensitivity study was conducted each time a different XYZ plane was used in order to determine an adequate disk size that would capture the majority of the vorticity generated by the core. This was accomplished by calculating the circulation (positive or negative, depending on the vortex) centered on a fixed point for increasing radius. Consecutive circulation values were compared with each other and a percent error was computed. The disk size was set once the percentage difference of circulation was smaller than 0.5%.

To illustrate this, the sensitivity study results for the XZ plane containing one or more inlet vortices is tabulated in Table 4.1, and the zone radius plotted for all XYZ planes depicted in Figure 4.2.

Table 4.1 Disk zone radius sensitivity test.

Test	I_{max}	J_{max}	r_{max} (cm)	r_{max}/D_i	Γ (m ² /s)	% Difference
1	90	157	1.50	0.0938	3.36	-
2	150	261	2.50	0.156	3.96	18.028
3	200	348	3.33	0.2083	4.01	1.229
4	250	435	4.17	0.2604	3.99	0.496
5	300	522	5	0.3125	4.03	0.937

Figure 4.2 shows that at a $\frac{r_{max}}{D_i} = 0.2604$, the percent error is less than 0.5% compared to the ratio at test 3. Thus, a disk zone radius of 4.1667cm was selected for all circulation calculations on the XZ plane.

Through a similar process, the disk zone radii for the XY and YZ planes were found to be 3.5833cm and 9.5833cm, as summarized in Table 4.2, along with I_{max} and J_{max} values. As will be addressed in Chapter 6, three distinct types of vortices were observed: inlet, trailing and secondary.

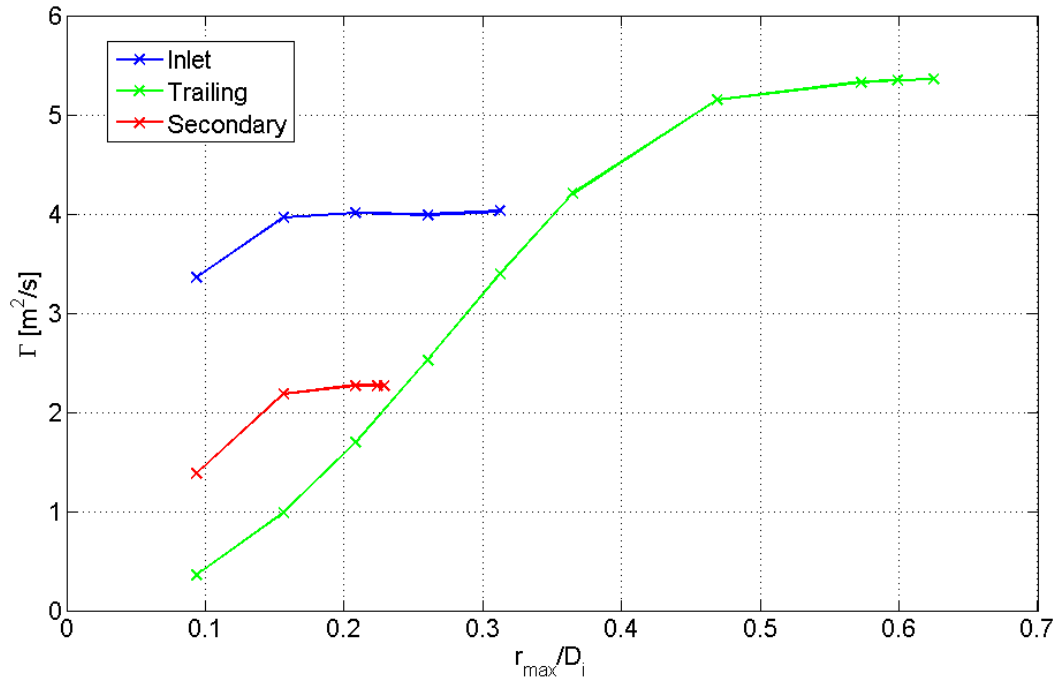


Figure 4.2 Zone radius sensitivity plot.

Table 4.2 Disk zone size for XZ, XY and YZ planes.

Plane	I_{max}	J_{max}	r_{max} (cm)	r_{max}/D_i
XZ	250	435	4.1667	0.2604
XY	215	374	3.5833	0.2240
YZ	575	1001	9.5833	0.5990

Since the core radii of trailing vortices was the largest of all vortical structures present in the inlet vortex phenomenon, a larger zone was needed to capture the vorticity present within its

core (YZ plane). Secondary vortices were observed on the XY plane and had the smallest core diameters.

4.3 Conclusion

This chapter presents the methods involved in post-processing CFD results. Fan face distortion coefficient, DC_{60} , and vortex circulation Γ were calculated for all time steps and are presented in Chapter 6. These parameters are important for quantifying the strength of inlet vortices as well as the impact they have on fan performance.

Chapter 5. Model Validation

Before any simulations were conducted using the geometry, domain and setup described in Chapter 3, a validation of the CFD model developed was performed. The work done by Murphy and MacManus (2011) was used as a reference for this validation phase, as is described below.

5.1 Experimental model description

The experimental model used by Murphy and MacManus (2011) at Cranfield University was simulated in order to perform model validation. The geometry studied consisted of a 1/30th scale, circular, cylindrical model of an inlet subject to a crosswind. The non-dimensional heights of the inlet center and measurement plane were 0.25 and 0.083, respectively, when normalized by the inlet's highlight diameter. The velocity ratio used by Murphy and MacManus (2011) was 18.3. This ratio was very hard to replicate in ANSYS FLUENT because the boundary conditions used for compressible flow required the specification of Mach number and stagnation pressure at the upwind wall, and mass flow rate at the fan face, making it difficult to match the velocities. The fan face Mach number was specified by Murphy and MacManus (2011), and was therefore

used to set this boundary condition. The wind conditions were then determined from the desired velocity ratio and calculated inlet suction speed.

The domain developed for this calculation resembled the previously-described model in Chapter 3, consisting of a cylinder inside a rectangular box. The dimensions of the box were 300cm (X direction) by 120cm (Y direction) by 195cm (Z direction). The mesh created contained the same refinement features as the one used for the case presented in Chapter 6, which was fully described in Chapter 3. It was comprised of both tetrahedral and wedge elements, with a total of 4.7 million elements. y^+ values were kept below 1 to ensure accurate boundary layer resolution. The boundary conditions specified at each of the domain zones are summarized in Table 5.1 below.

Table 5.1 Summary of boundary conditions specified at each domain zone in the validation model.

Surface (or zone)	Boundary Condition type
Ground	No-slip wall
Inlet lip	No-slip wall
Inlet body	No-slip wall
Fan face	Pressure outlet (with target mass flow rate)
Upwind	Mass flow inlet
Downwind	Pressure far-field
Headwind	Pressure far-field
Tailwind	Pressure far-field
Top	Pressure far-field

Note that the boundary conditions for the four sides and top of the domain box are the opposite of those specified in the case presented in Chapter 3. As this author's knowledge of

ANSYS FLUENT grew, the boundary conditions selected in Chapter 3 were deemed more appropriate and overall a better choice regarding solution stability and convergence. The calculation performed here was u-RANS, three-dimensional, unsteady and turbulent. The SST $k-\omega$ turbulence model was used and specified as described in the numerical methods chapter of this report.

5.2 Comparison of results

The results of the simulation are plotted in Figure 5.1(a), Figure 5.2(a) and Figure 5.3(a) alongside equivalent results measured by Murphy and MacManus in their experiments, shown in Figure 5.1(b), Figure 5.2(b) and Figure 5.3(b). Parameters compared include fan face stagnation pressure loss, out-of-plane velocity and vorticity contours, and velocity vectors on the measurement plane.

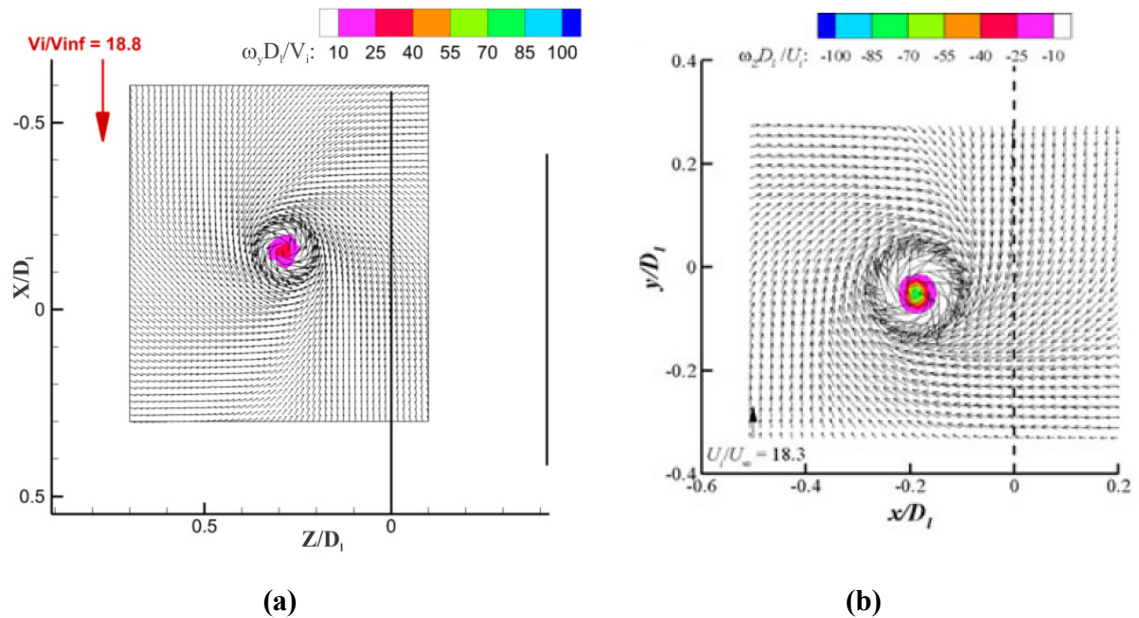


Figure 5.1 Velocity vectors and out-of-plane vorticity contours on the measurement plane with coordinates non-dimensionalized by inlet highlight diameter, obtained from (a) the numerical calculation and (b) Murphy and MacManus (2011).

Figure 5.1(a) and (b) show good agreement in the velocity and vorticity distributions on the measurement plane. Both results show an increase in rotational speed moving inwards towards the vortex core. The core location was about 5cm farther out from the inlet in the numerical calculation and another 5cm farther upwind than in the experimental case. The out-of-plane vorticities, non-dimensionalized by inlet highlight diameter and inlet suction speed at the last time step, are approximately 40 and 60 for the calculation and experiment, respectively, with the experimental results containing about 50% higher vorticity.

Figure 5.2(a) and (b) compares the non-dimensional out-of-plane velocity contour obtained in the calculation and experiment. The contour profiles are very similar to each other, with the highest out-of-plane velocity located at the core's center, slightly upstream of the inlet axis. The non-dimensional velocity at the vortex core is 0.3 and 0.35 in the two cases, respectively; about a 17% difference.

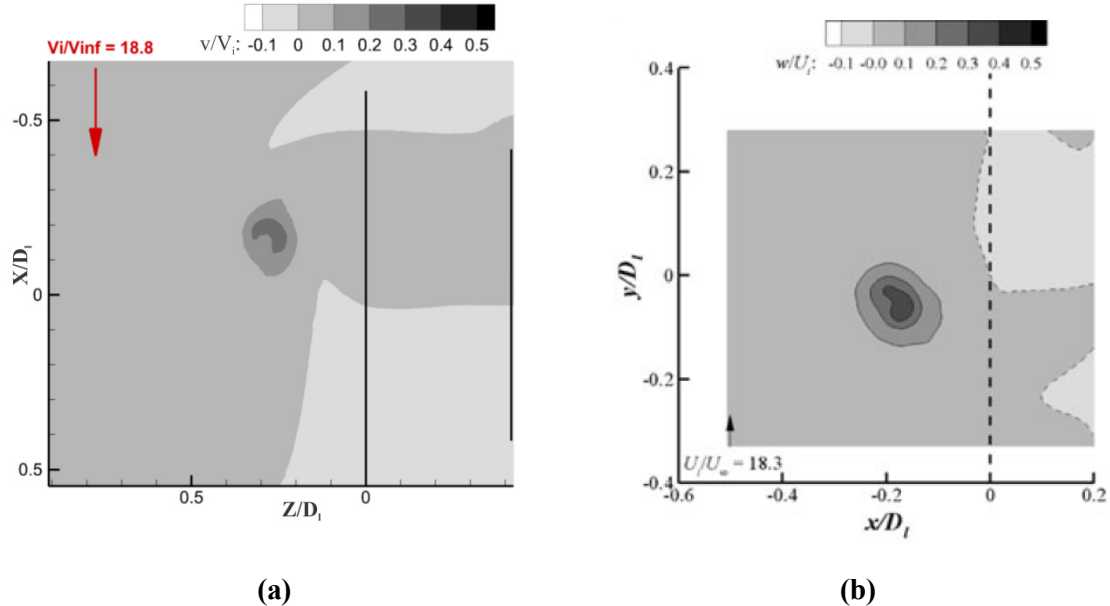


Figure 5.2 Out-of-plane velocity contours on the measurement plane obtained from (a) the numerical calculation and (b) Murphy and MacManus (2011).

The fan face contours (Figure 5.3(a) and (b)) show qualitatively comparable results, indicating the vortex ingestion location was at about 40 degrees from the vertical towards the upwind side of the inlet. However, quantitatively, the calculated stagnation pressure loss at the vortex ingestion point was four times smaller than that from the experiment. Possible reasons for this discrepancy include:

1. The constants specified in the SST $k-\omega$ turbulence equations may have needed refinement. As was mentioned in Chapter 3, the values used were the standard default ANSYS FLUENT values, as per recommendation of ANSYS FLUENT 14 User's Guide.
2. The SST $k-\omega$ turbulence model specified may not have been the most accurate to resolve turbulent properties within the inlet for the elapsed flow time. This model was chosen for reasons presented in Chapter 3, but a turbulence model sensitivity study could be conducted to compare results.

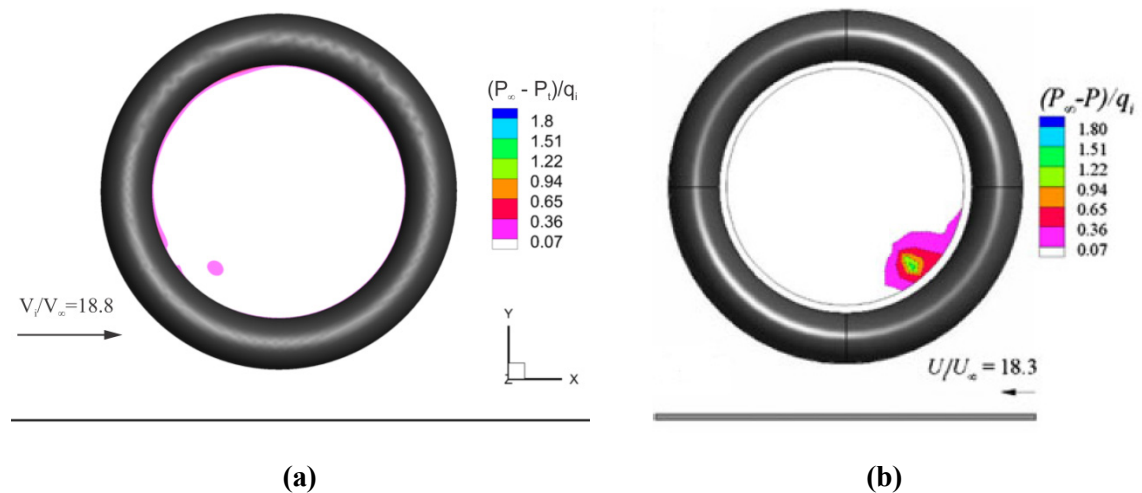


Figure 5.3 Fan face stagnation pressure contours on the measurement plane, non-dimensionalized by far upwind stagnation pressure and fan face averaged dynamic pressure, obtained from (a) the numerical calculation and (b) Murphy and MacManus (2011).

The above observations also apply to the case presented in Chapter 6, affecting fan face distortion computations. The DC_{60} value obtained from the numerical calculation was 0.058, while Murphy and MacManus' (2011) distortion coefficient was 0.12.

5.3 Conclusion

Despite quantitative discrepancies in the results obtained with the CFD model, the data qualitatively resembled Murphy and MacManus' (2011) measurements and the model developed herein served the purposes of this research project. For quantitative results that would be expected to reflect experiments, the author believes that further refinement of the model is necessary, as reflected by the quantitative discrepancies presented here. As such, the analysis described in this report relies heavily on qualitative observations. Calculations were made regarding fan face distortion and vortex strengths, but the author does recognize that these may be less than the actual values were experiments to be carried out.

Chapter 6. Time History of Inlet Vortex Formation

This chapter contains a summarized description of the case studied in this thesis research, followed by a presentation and discussion of results obtained from ANSYS FLUENT. A flowfield characterization is made, showing stagnation pressure and out-of-plane vorticity contours at the fan face and near-ground planes for select time steps. Velocity vectors on the near-ground plane are plotted showing the flowfield topology around each vortex. Vorticity magnitude iso-surfaces are also presented in three dimensions in order to visualize vortex cores. Vortex filament sketches summarize the flowfield at each time step, allowing for comparison between all time steps presented. These are followed by time history plots of minimum ground pressure, vortex strengths and fan face distortion coefficient.

6.1 Case description

As discussed previously in Chapter 3, the case studied in this investigation was that of an inlet under crosswind with a step-change in wind speed. This wind profile was chosen by the author to resemble a true scenario an engine may undergo, in which the wind speed may vary.

The first wind speed is selected such that the farfield velocity ratio is larger than the critical ratio for this inlet geometry; the second wind speed is calculated based on a higher farfield velocity ratio, placing it farther above the threshold curve, as illustrated in Figure 6.1. In this way, in both cases a clear inlet vortex is expected to form. The non-dimensional height ratio H/D_i is fixed at 1.25; the velocity ratio V_i/V_∞ , based on a farfield wind speed, is varied from 18 to 25 by decreasing the crosswind speed while keeping the inlet suction speed constant. The domain and mesh created for this research were shown earlier in Figures 3.2 and 3.3, respectively, and the boundary condition setup was discussed in section 3.5.2. The total flow-time simulated in this test is 1.15s.

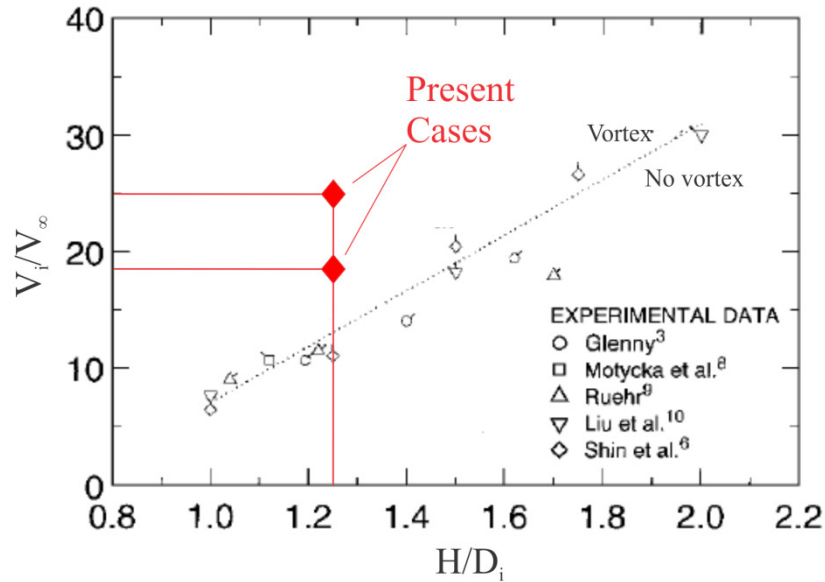


Figure 6.1 Vortex formation correlation, highlighting the two cases studied in this report (De Siervi *et al.*, 1982).

6.1.1 Velocity profile

Figure 6.2(a) and (b) present a time history of the crosswind speed and velocity ratio, respectively. The farfield location is defined as the upwind zone within the domain where the

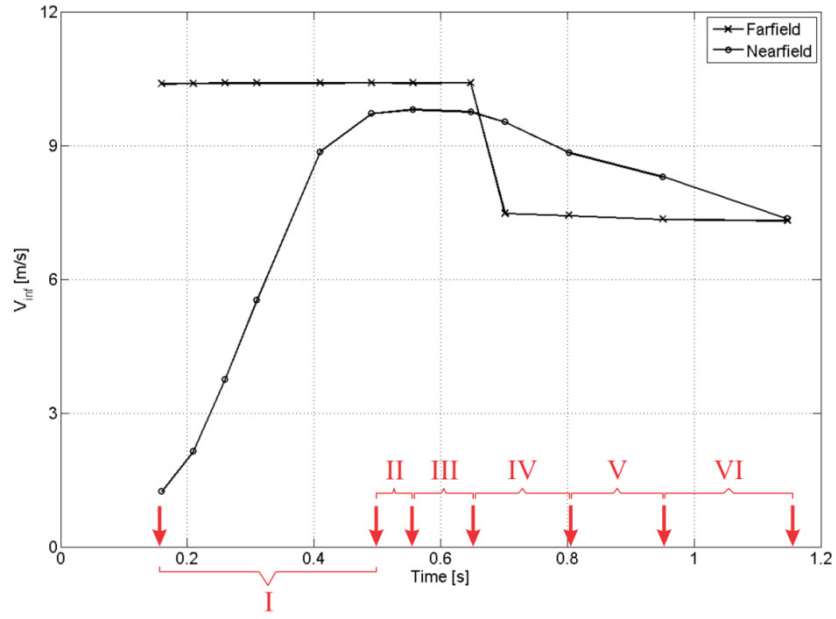
upstream boundary condition is set, as described in Chapter 3. The nearfield location is defined at a point far enough from the surface of the nacelle to avoid potential flow effects, located precisely at (X,Y,Z) coordinate of (-0.10m; 0.40m; -0.73m) and lying on the windward leading edge lip plane perpendicular to the ground. Such distinction is necessary in order to differentiate farfield flow quantities from those observed near the inlet, which take longer to achieve convergence since the farfield boundary condition propagation is not instantaneous throughout the domain.

The arrows labeling Figure 6.2(a) represent the time steps chosen for detailed analysis and flowfield comparison, as presented in section 6.3.

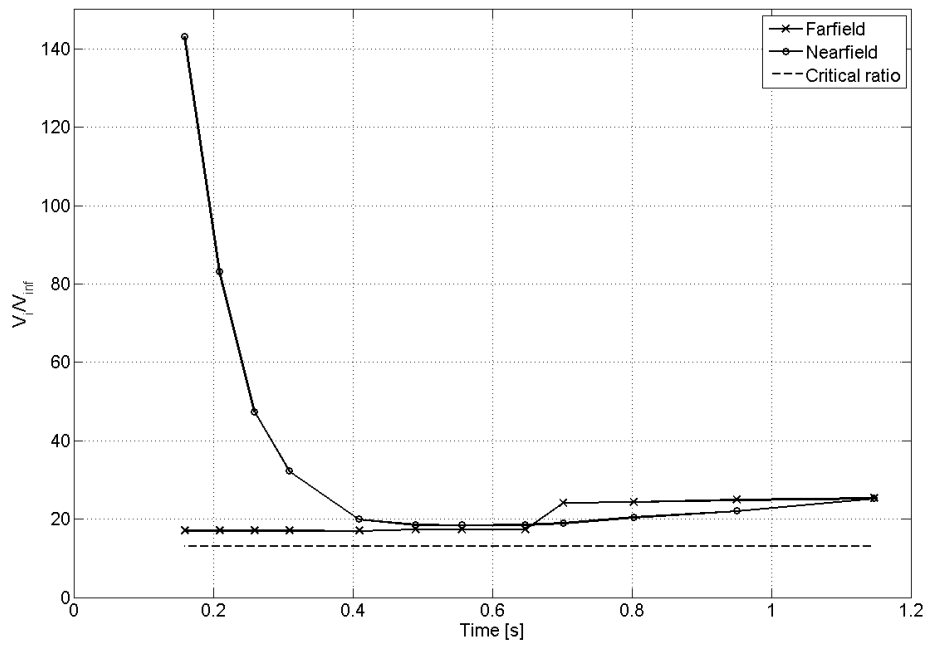
The total flowtime calculated is divided up into six time intervals according to the selected time steps, each representing a unique phase in the inlet vortex formation process as listed below:

- I. Two upstream counter-rotating vortices;
- II. Two downstream counter-rotating vortices;
- III. Three downstream vortices;
- IV. Step-change in farfield wind speed;
- V. Three vortices shift upstream;
- VI. Vortex coalescing.

The initial and final farfield crosswind speeds, representing the step-change in wind speed, are 10.4m/s and 7.5m/s, respectively, calculated from the area-weighted average of V_x at the upwind zone. The change occurred at approximately 0.7s, as indicated in Figure 6.2(a). The nearfield crosswind speed was determined by probing V_x at the nearfield location mentioned above. It ramps up from zero to about 10m/s throughout the first 0.5s, levels out, and then, following the step change in farfield wind speed at 0.7s, decreases to the new wind speed, arriving at around 7m/s at time 1.15s, when the simulation was ended.



(a)



(b)

Figure 6.2 Time history of (a) crosswind speed V_∞ and (b) velocity ratio V_i/V_∞ .

The velocity ratio based on the farfield V_x remained constant at approximately 18 and 23 for the two crosswind speeds specified, as shown in Figure 6.2(b). When measured at the nearfield location, however, the ratio is initially at a high value due to the low crosswind speed,

coming down to the desired value after 0.5s. It was expected that the nearfield velocity would require some time to adjust at the start of the simulation as well as following the step-change in the farfield wind speed. The critical velocity ratio of 13, calculated for this inlet geometry, is plotted in Figure 6.2(b) as a dashed line, confirming that the velocity ratio is kept well above the threshold and consequently a single inlet vortex is anticipated.

6.2 Summary of observed vortices

As will be discussed in sections 6.3 and 6.4, numerical results indicate that during the inlet vortex formation process, multiple ground-to-inlet vortices exist at various time steps, accompanied by trailing and secondary vortices. Secondary vortices, which to this author's knowledge have not been identified in the literature before, are located on the underside of the inlet with cores aligned parallel to the ground plane before being ingested.

Table 6.1 Summary of vortices observed at each time step.

Time [s]	Ground-to-Inlet	Trailing	Secondary
0.1594	2	0	0
0.4904	2	1	1
0.5564	3	1	2
0.6474	3	1	1
0.8024	3	1	1
0.9504	1	1	1
1.1474	1	1	1

Table 6.1 summarizes the number of ground-to-inlet, trailing and secondary vortices observed at each of the time steps that will be described in section 6.3. It shows that multiple ground-to-inlet vortices coexist during the first 0.95s of simulation, after which only one remains – this behavior has not been described in the literature. This behavior is discussed in detail in this chapter. Moreover, trailing and secondary vortices are not present during the first 0.5s of

simulation. This is attributed to the nearfield wind speed's non-instantaneous adjustment to the farfield boundary condition. While some time steps contain two secondary vortices, only one trailing vortex exists throughout the simulation. All of the observed vortices are highly unsteady, changing location and even rotational direction at each of the investigated time steps.

6.3 Flowfield characterization

This section defines the planes on which vortex properties were computed, as well as their sign convention. A compilation of figures and diagrams characterizing the flow-field at various time steps during the unsteady formation process of the inlet vortex is also presented. These time steps were chosen such that the vortex formation process could be clearly illustrated without any redundancies or repetitions. The selected time steps are labeled by the red arrows in Figure 6.2(a).

6.3.1 Inlet, trailing and secondary vortex plane definitions

In order to compute the properties of the inlet vortex, a near-ground plane was defined at a distance of 1cm above the ground plane, as illustrated in Figure 6.3(a). Positive vorticity was then defined in the direction of the positive Y unit vector, as shown in Figure 6.3(b). This then leads to the convention that vortices with positive vorticity on this plane rotate in a counter-clockwise direction when looked from above the near-ground plane (Figure 6.3(b)).

Likewise, a plane was created at the $X = 0.15\text{m}$ location where all trailing vortices would be studied, as shown in Figure 6.4(a). Positive vorticity was defined in a direction parallel to the positive X unit vector (Figure 6.4(b)). Hence a trailing vortex with a positive vorticity core would rotate in a clockwise direction when observed from upstream of the plane (Figure 6.4(b)).

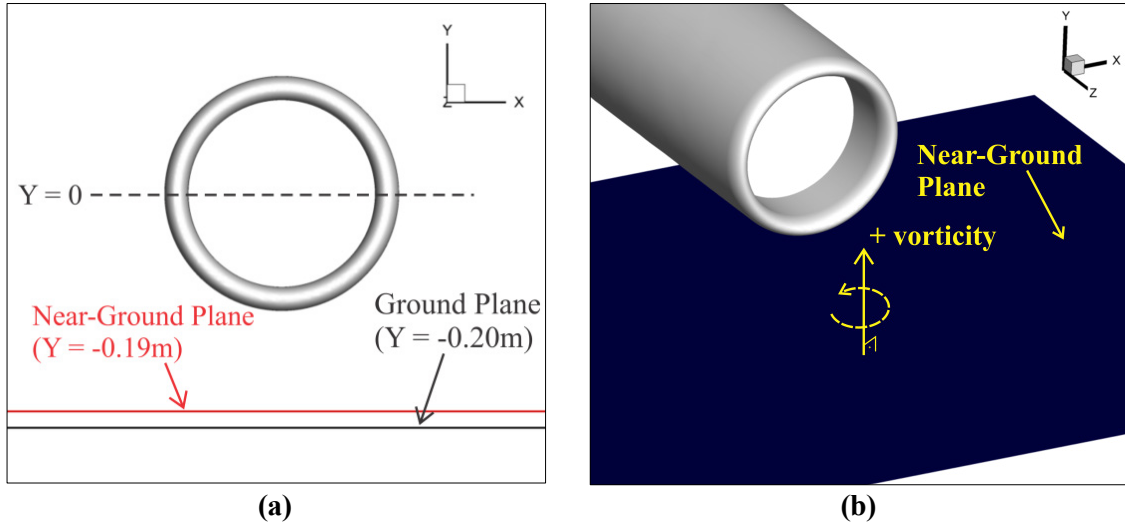


Figure 6.3 (a) Location of near-ground plane and (b) definition of positive vorticity on this plane.

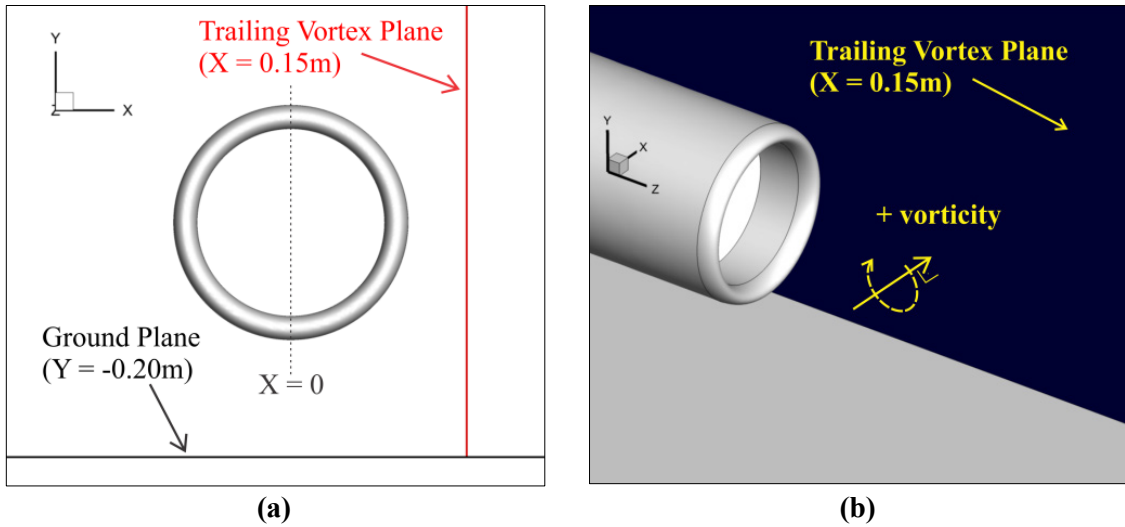


Figure 6.4 (a) Location of trailing vortex plane and (b) definition of positive vorticity on this plane.

Lastly, a third plane was defined at the $Z = 0$ location to observe all secondary vortices, as shown in Figure 6.5(a). Positive vorticity was defined in a direction parallel to the positive Z unit vector (Figure 6.5(b)). Therefore a secondary vortex with a positive vorticity core would

rotate in a counter-clockwise direction when seen from a location with positive Z coordinate (Figure 6.4(b)).

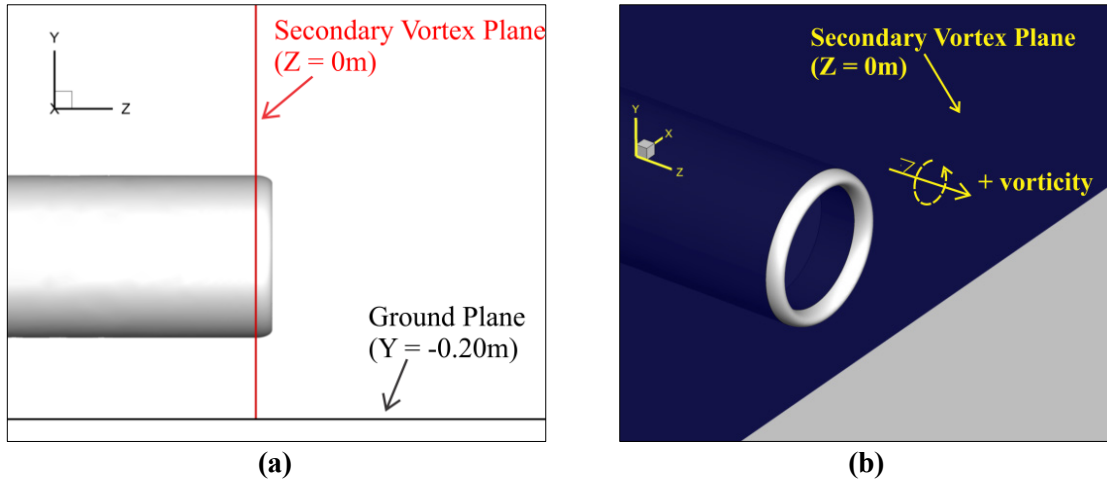


Figure 6.5 (a) Location of secondary vortex plane and (b) definition of positive vorticity on this plane.

6.3.2 Two upstream counter-rotating vortices – time step 0.16s

One of the most illustrative ways of identifying the presence of vortices in a flow is by plotting velocity vectors on a plane parallel to the ground. Figure 6.6(a) shows tangent velocity vectors on the near-ground plane at time step 0.16s.

The figure shows the crosswind moving from the left to the right (positive X direction) and the presence of two counter-rotating vortex cores. The lower of the two cores rotates in a counter-clockwise direction, while the upper, clockwise. The cause of the counter-rotating pair can be inferred from the velocity vectors surrounding the vortices. The wind moving under the inlet is drawn forward (in the positive Z direction) by the inlet suction, meeting air in front of the engine, which was initially moving from left to right with the crosswind but is now drawn aft (negative Z direction) due to the suction of the engine. Therefore, a saddle point forms where these approaching flows meet, labeled in Figure 6.6(a) and identified by the crossed white lines.

The streamlines converge to this saddle point along a path called the attachment line, which in this case lies parallel to the X axis; they are then channeled perpendicular to their original flow direction along a separation line, diverging from the saddle point in the positive and negative Z directions (shown by the white arrows). As the airflow moves along the separation line, it merges with freestream air surrounding the saddle point; this causes the merged airflow to curl around the tips of the separation line, creating two counter-rotating foci. Due to the inlet suction effect, these foci are stretched vertically (in the Y direction) and sucked into the inlet, forming the cores of the two counter-rotating vortices. It is important to note that without the formation of this saddle point, no ground vortices would exist, as has been claimed by Klein (1959) and De Siervi *et al.* (1982), and illustrated by the current result.

Figure 6.6(b) shows gauge pressure contours on the near-ground plane, revealing low-pressure regions where the vortex cores are located. The figure clearly reveals that the clockwise vortex located closer to the inlet contains a region of lower pressure within its core than the counter-clockwise vortex. The scale shows that this low pressure is around 101,200Pa, which is not nearly low enough to make FOD a concern.

Out-of-plane vorticity contours are plotted on the near-ground plane in Figure 6.6(c), illustrating the two vortices. Their directions of rotation have been added to the figure using arrows (the positive Y vector points out of the page). The vorticity contours in this figure were non-dimensionalized by inlet inner diameter and the area-weighted average of V_z at the fan face at the last time step of the simulation. These results confirm the presence of two counter-rotating vortices, plainly identifying the vortex closest to the inlet as the strongest of the two, evidenced by its higher vorticity magnitude.

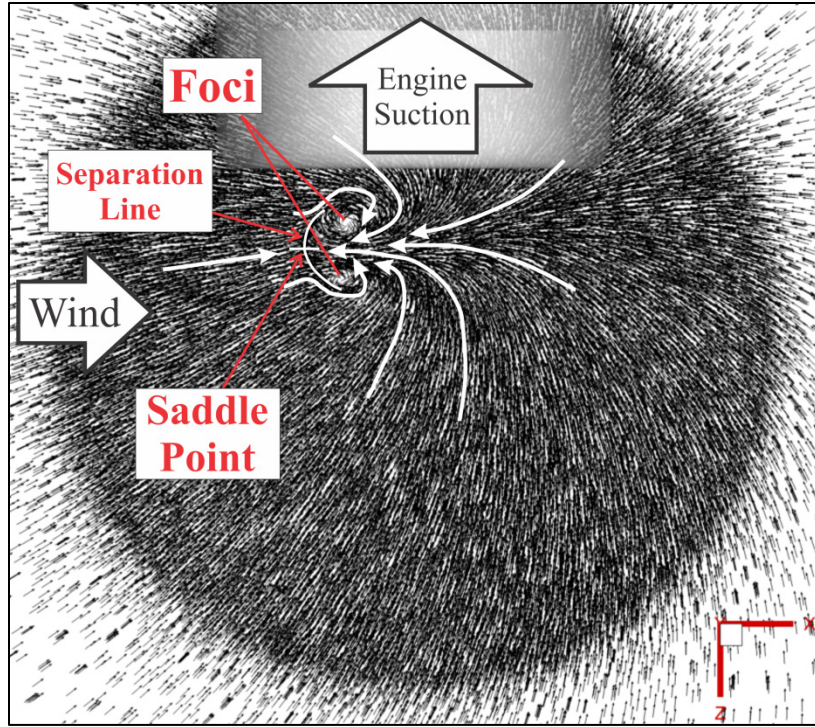
Figure 6.6(d) shows out-of-plane vorticity contours on the fan face plane. Positive vorticity points out of the page. This means that the clockwise vortex (negative vorticity) seen on

the near-ground plane is a counter-clockwise vortex when observed at its fan face ingestion location. The counter-clockwise vortex on the near-ground plane, on the other hand is a clockwise vortex in Figure 6.6(d). The maximum Z vorticity magnitude at the fan face is slightly lower than the maximum ground Y vorticity magnitude, suggesting the vortex has lost some vorticity as it is stretched vertically and ingested by the inlet.

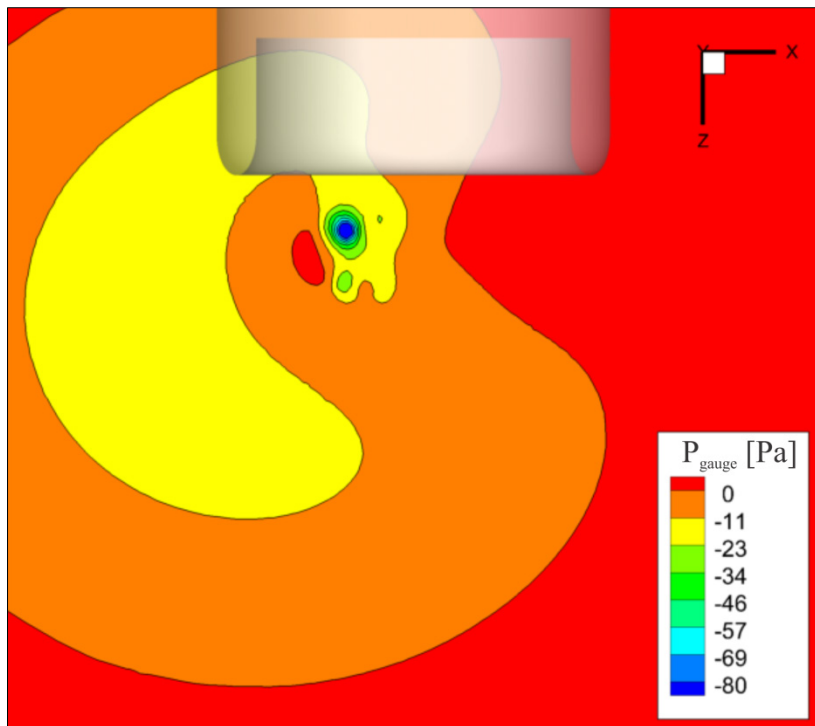
In order to evaluate fan face distortion, stagnation pressure contours are studied at the fan face, non-dimensionalized by a farfield stagnation pressure of 101,325Pa (Figure 6.6(e)). The results show low levels of distortion at the fan face, with stagnation pressure losses confined to the thin boundary layer around the fan and the vortex ingestion locations. This is consistent with expected results. The figure does not show a windward lip separation region due to the low elapsed flow time. Comparing Figure 6.6(d) and (e), the region of highest pressure loss corresponds to the positive Z vorticity region seen on the fan face, where the strongest inlet vortex is ingested. This area on the fan plane is responsible for creating the largest fan face distortion with a DC_{60} of approximately 0.06.

In order to visualize the vortex cores generated at this time step, vorticity magnitude iso-surfaces are shown in Figure 6.6(f), along with fan face out-of-plane vorticity contours identifying the vortex ingestion locations. Figure 6.6(f) reveals two vortex cores, outlining the structure of the inlet vortices as they are ingested by the engine. At this vorticity magnitude level ($1800s^{-1}$), vorticity is also generated on the surfaces of the nacelle and lip, both inside and outside. This vorticity is produced within the boundary layer and is the source of vorticity for the inlet vortices, as previously discussed in the literature review.

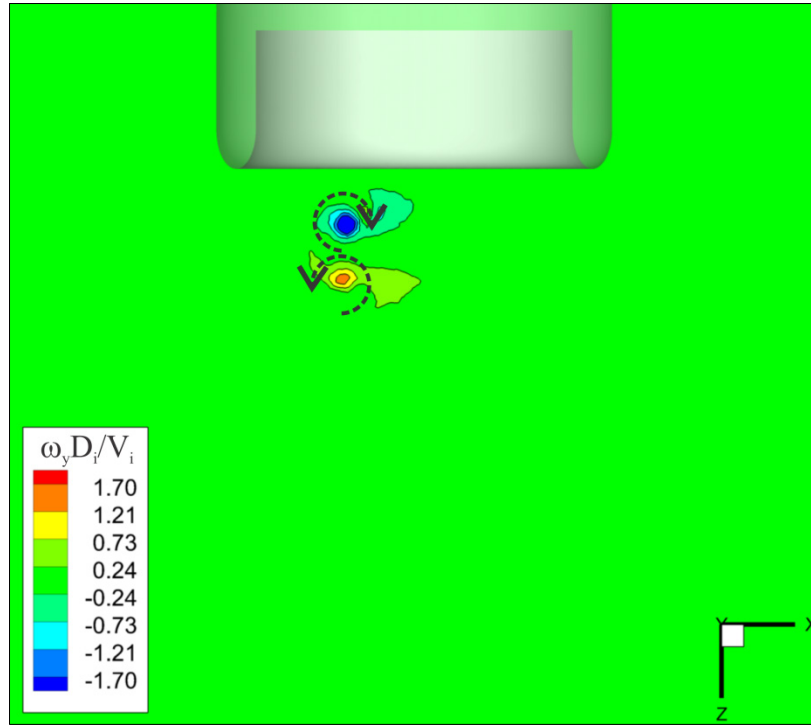
To summarize the flowfield at time step 0.16s, Figure 6.6(g) shows a sketch in isometric view, outlining the vortex filaments that correspond to each of the vortices observed. These filaments indicate the location and rotational direction of the vortex cores.



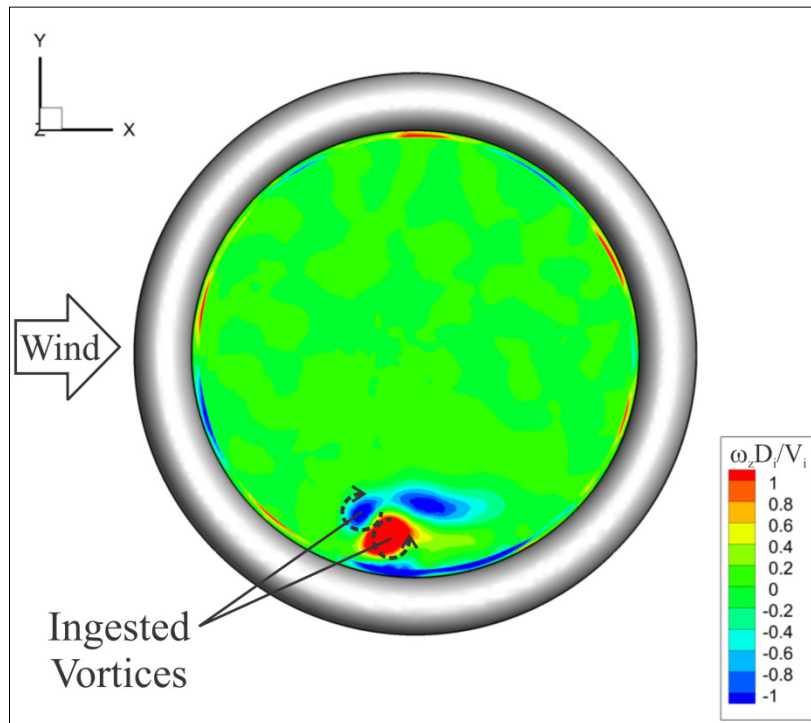
(a)



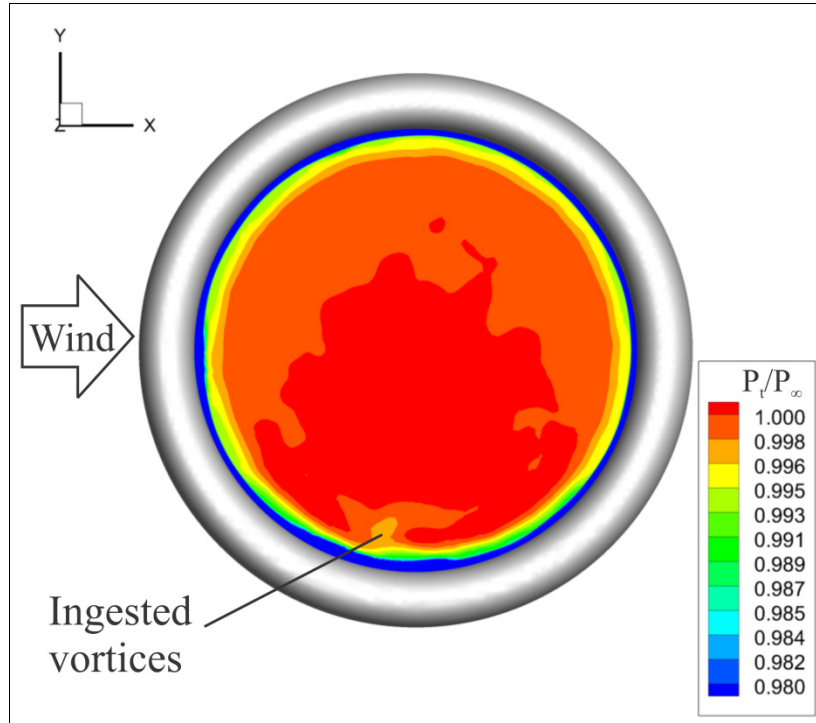
(b)



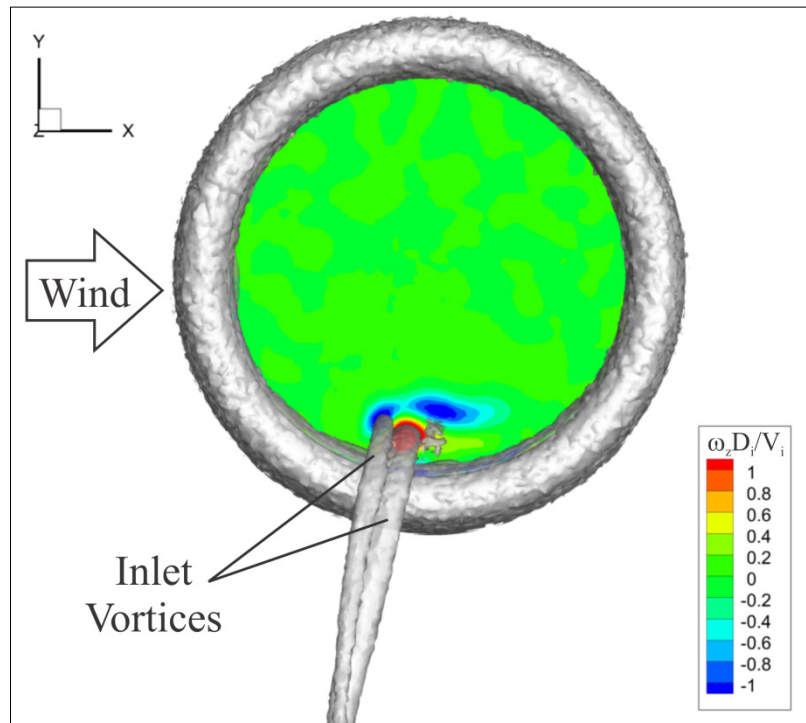
(c)



(d)



(e)



(f)

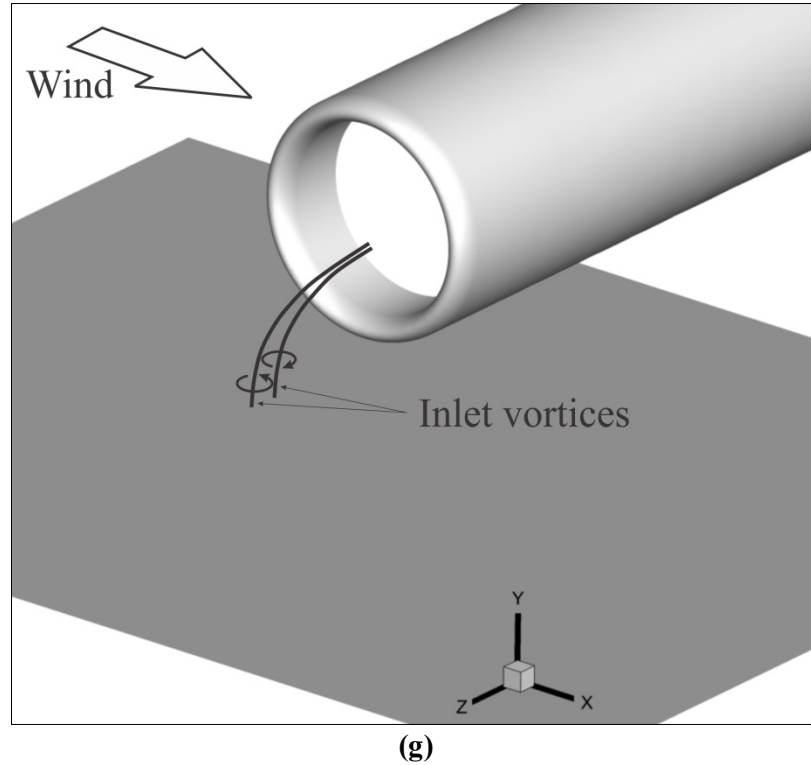


Figure 6.6 (a) Velocity vectors, (b) static gauge pressure contours, and (c) out-of-plane vorticity contours on near-ground plane, followed by (d) out-of-plane vorticity contours and (e) stagnation pressure on the fan face plane, accompanied by (f) vorticity magnitude iso-surfaces to visualizing vortex core profiles and (g) vortex filament sketch summarizing the flow field at time 0.16s.

6.3.3 Two downstream counter-rotating vortices – time step 0.49s

Figure 6.2(a) shows that at time step 0.49s, the nearfield crosswind speed has already ramped up and reached a constant value, close to the specified farfield wind speed. At a higher nearfield wind speed, the two vortices observed previously are expected to be blown downstream by the wind. Figure 6.7(a) confirms this hypothesis.

The vortex system has indeed moved downstream, rotating about 45 degrees counter-clockwise. The counter-clockwise vortex has moved the farthest downstream and has increased in diameter as well. This makes sense in light of the increase in nearfield wind speed, adding more air to the rotating mass-flow surrounding this vortex and raising its rotational speed, while

pushing it downwind. A saddle point is observed linking the two vortices together via a separation line, as described at time step 0.16s. The vortices are formed by the same mechanism discussed in the previous section. However, the distance between their cores has now increased, allowing for more downstream air to flow between them. This, in turn, adds more mass flow to their cores, increasing their size and angular momentum.

The near-ground pressure contours (Figure 6.7(b)) reveal two major changes from the previous time step. Firstly, the dominant vortex is now the counter-clockwise vortex, evidenced by the lowest pressure core (in contrast to the previous time step when the clockwise vortex was the strongest); and secondly, the ground pressures within both vortex cores drops to 300Pa below gauge from a previous 30Pa below gauge for the counter-clockwise vortex, and to 180Pa below gauge from a previous 80Pa below gauge for the clockwise vortex. Both of these observations are attributed to the continual production of vorticity within the inlet and ground boundary layers, as well as its distribution to the vortices present in the system via convection. As a consequence, both vortices exhibit an increase in rotational speed and suction strength. Nevertheless, these ground pressures are still not low enough for FOD to occur.

The out-of-plane vorticity contours on both the near-ground (Figure 6.7(c)) and fan face (Figure 6.7(d)) planes show the downstream shift of the cores and increase of their separation distance. On the near-ground plane, areas of high vorticity exist in the vicinity of each of the vortices following circular patterns. These are associated with the swirling motion of the vortices. They illustrate the inlet vortices' ingestion of vorticity produced within the ground boundary layer, responsible for sustaining the cores. Based on experiments and numerical studies found in the literature, inlet vortices are a direct consequence of viscous flow effects, and do not exist when wall slip is assumed. The presence of boundary layers in turbulent flow allows the formation of rotating flow structures within these layers, which is believed to be the main source

of vorticity for the inlet vortex system (De Siervi *et al.*, 1982). The vorticity contained in these rotating flow structures is convected into the inlet vortex cores, increasing their strength. Figure 6.7(d) shows the increased strength of both vortices, more noticeably evidenced by the downstream vortex, which exhibits a six-fold increase in vorticity compared with the previous time step (Figure 6.6(d)).

In addition to two counter-rotating inlet vortices, two other types of vortices are visible on the fan face: a trailing vortex and two secondary vortices. A trailing vortex always accompanies inlet vortices, as was mentioned in the literature review. It is only observed, however, beginning at 0.49s, once the nearfield wind speed is sufficiently high to enable the production of vorticity within the outer nacelle boundary layer. Figure 6.7(d) shows the ingestion region of the trailing vortex's inner core, which is seen to rotate in a counter-clockwise direction when looking into the fan face. Its direction of rotation is opposite to that of the strongest inlet vortex, as identified by De Siervi *et al.* (1982). However, it is very difficult to make observations concerning the size of the trailing vortex based on Figure 6.7(d) due to the coarse mesh used in this region of the domain, as discussed in Chapter 3.

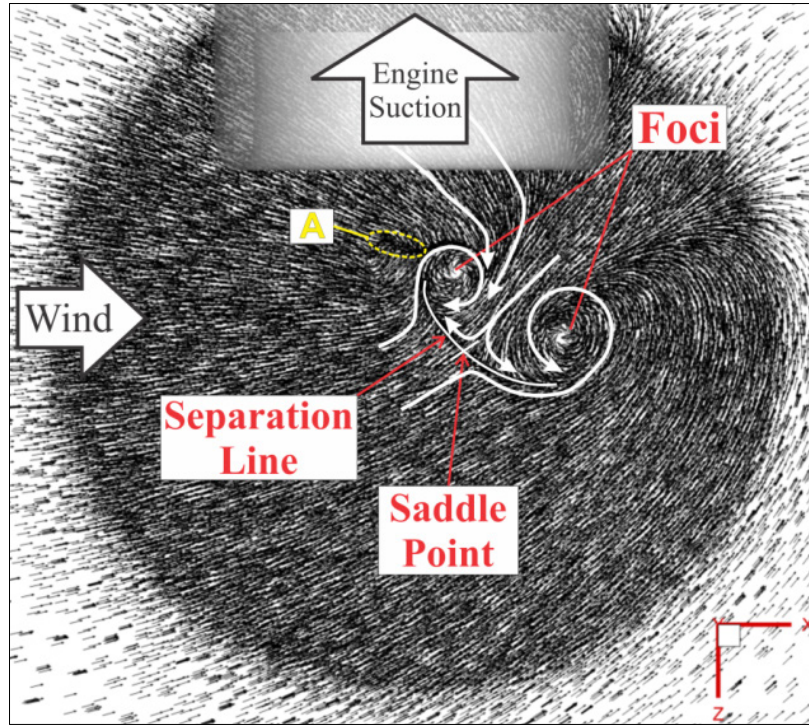
Moreover, one secondary vortex is observed, in addition to the inlet and trailing vortices and is identified in Figure 6.7(d). This secondary vortex enters the inlet rotating clockwise and is characterized by a strong rotating core, comparable to the main inlet vortex. After tracing the core's profile (as illustrated in Figure 6.7(f)), it was found that this vortex did not originate on the ground. Reducing the iso-surface vorticity level, the secondary vortex appears to have originated on the outside surface of the inlet's underside, near the 5 o'clock position. Results show that a stagnation point occurred at this near-wall location, responsible for creating the vortex via a similar mechanism as the ground vortices, and that the vorticity generated by the nacelle's boundary layer fluid is convected into this vortex.

A third inlet vortex appears to be forming as well. This vortex originates from an area A labeled in yellow on Figure 6.7(a) on the ground plane, and although no rotating core is identified on the ground plane, a sharp turning of the velocity vectors is present in that area, indicating a region of concentrated vorticity. At this moment, it is a weak vortex, having the smallest out-of-plane vorticity component on the fan face. Area A resembles the typical flowfield surrounding a saddle point and, as will be seen in the following time step, a saddle point is indeed developing in this region. Hence, a new inlet vortex could indeed be forming at the current time step, justifying the additional vortex ingestion region identified by Figure 6.7(d).

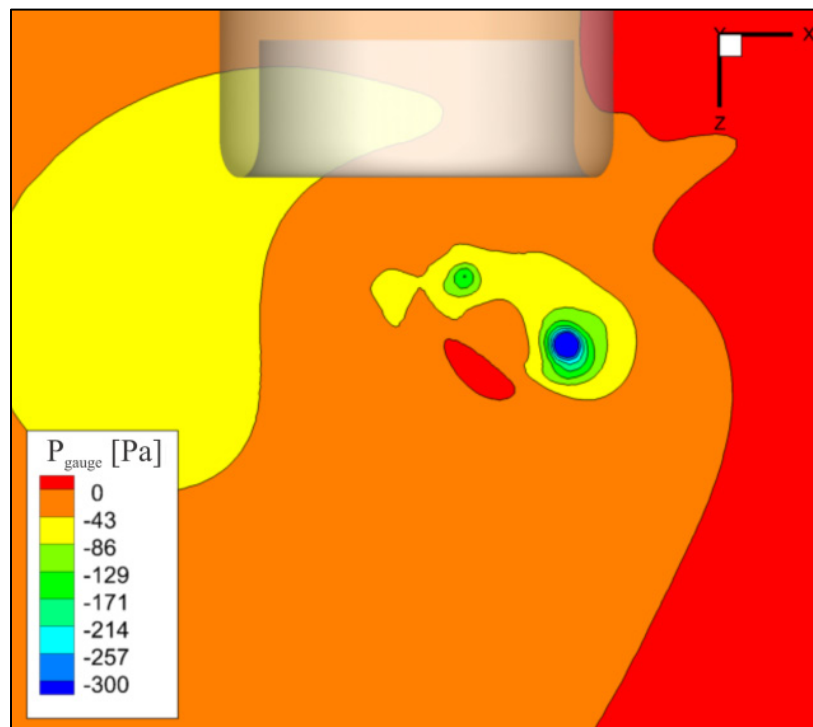
An unknown vortex is also visible at the fan face, as labeled in the Figure 6.7(d). No core structure is present, and it is believed this vortex is created within the lip separation region, and hence is not a part of the inlet vortex system. This additional vortex is not observed at any other time step and is therefore disregarded from the analysis. Figure 6.7(f) shows the inlet, trailing, and secondary vortex cores via vorticity magnitude iso-surfaces. It clearly shows the difference in vortex strength amongst the inlet vortices, with the right-most vortex containing the highest level of vorticity. It also confirms the formation of a third inlet vortex, identified as the “inlet vortex under formation”.

Lastly, fan face stagnation pressure contours are illustrated in Figure 6.7(e), showing pressure losses due to the trailing vortex, in addition to the inlet and secondary vortices, as well as the appearance of a lip separation region. The stagnation pressure loss at the core of the clockwise inlet vortex (seen looking into the fan face) drops from 0.996 at time step 0.16s to 0.99. A lip separation region is now developing on the windward side of the inlet. This region contains significantly lower stagnation pressures than the vortex cores.

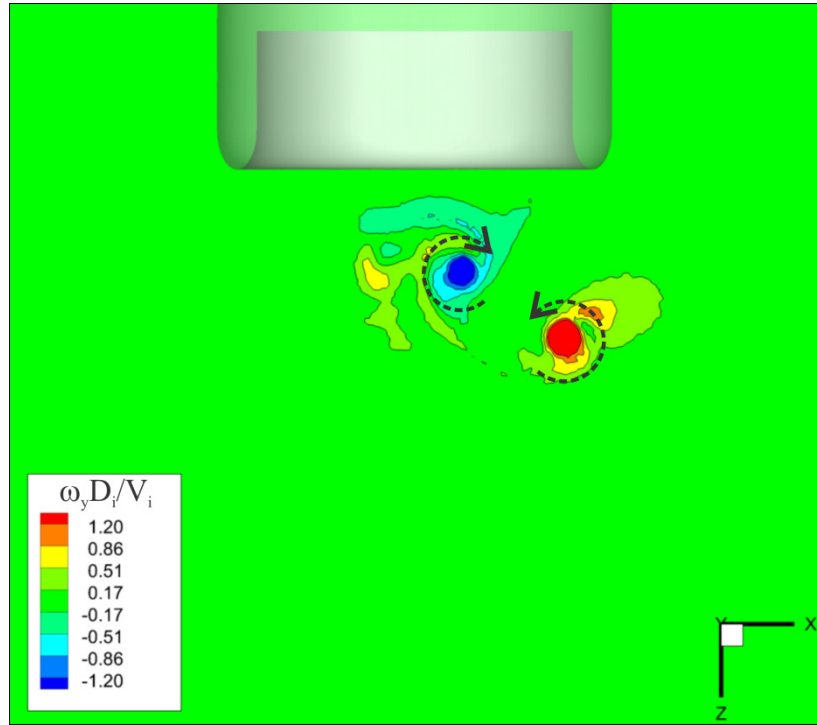
To summarize the flow field at time step 0.49s, Figure 6.7(g) shows a sketch containing vortex filaments that correspond to each of the vortices observed.



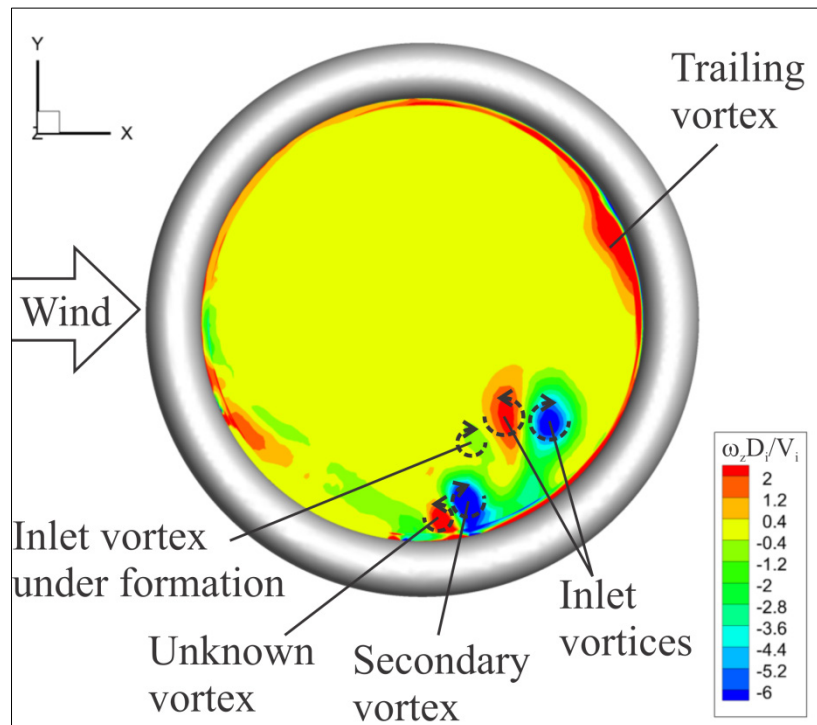
(a)



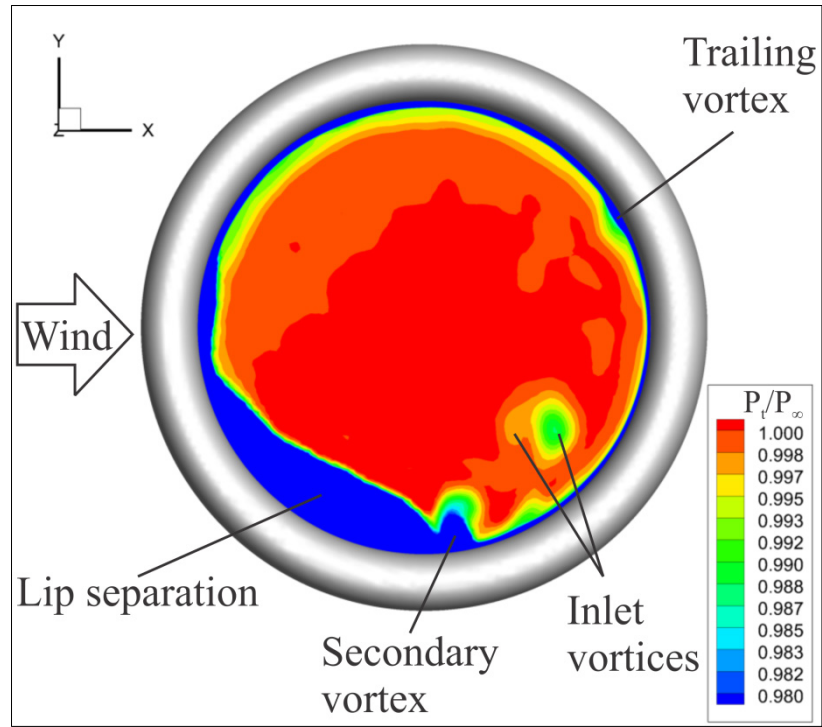
(b)



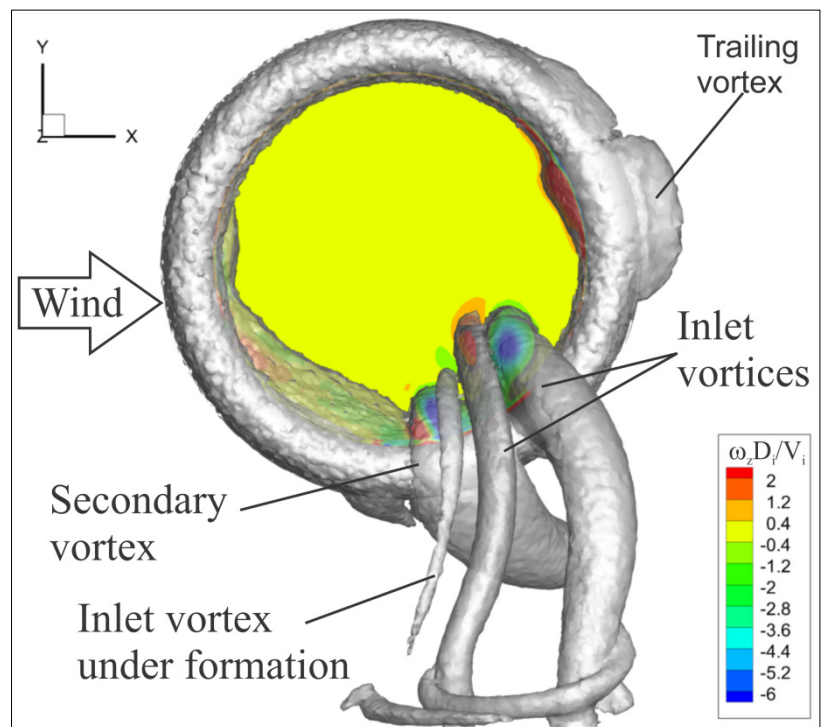
(c)



(d)



(e)



(f)

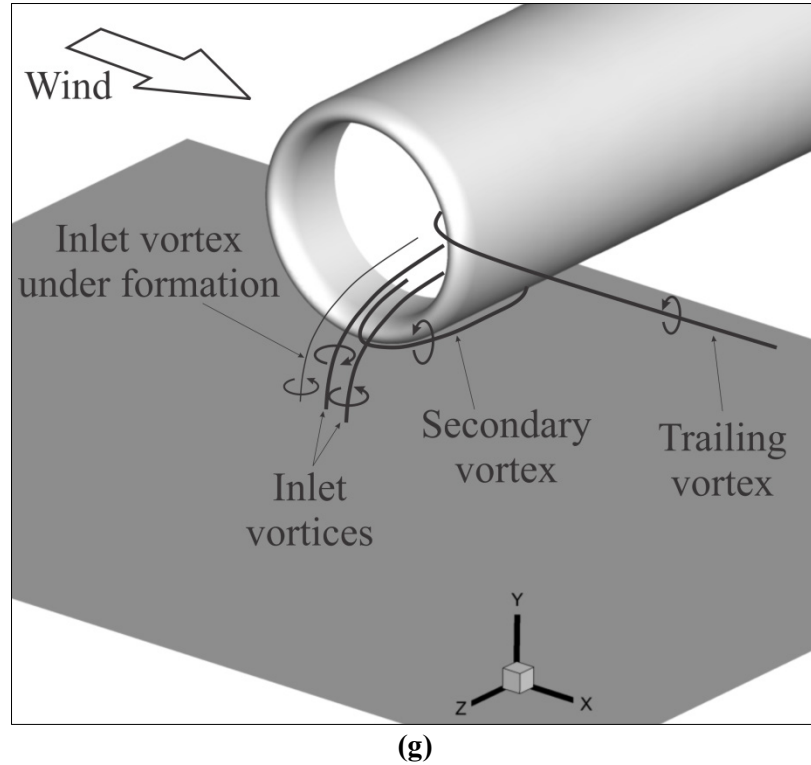


Figure 6.7 (a) Velocity vectors, (b) static gauge pressure contours, and (c) out-of-plane vorticity contours on near-ground plane, followed by (d) out-of-plane vorticity contours and (e) stagnation pressure on the fan face plane, accompanied by (f) vorticity magnitude iso-surfaces to visualizing vortex core profiles and (g) vortex filament sketch summarizing the flow field at time 0.49s.

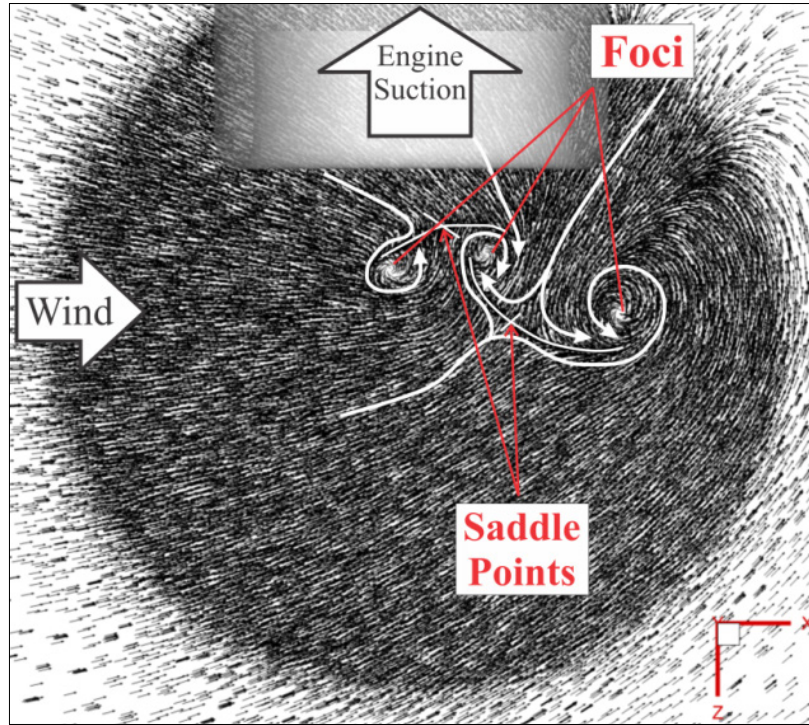
6.3.4 Three downstream vortices – time step 0.56s

At time step 0.56s, three vortices are present. The left-most vortex from the previous time step has split into two counter-rotating vortices, when seen from above the near-ground plane, while the right-most has remained whole (Figure 6.8(a) and (c)). The saddle point existing between the two vortices in the previous time step is still present in this flowfield (between the right-most and center vortices), and an additional saddle point has formed between the center and left-most vortices, as labeled in Figure 6.8(a). This new saddle point originates from the area A labeled in Figure 6.7(a) in the previous time step, along with a new separation line. Consequently, three foci points are formed, which are then stretched vertically forming three inlet vortices.

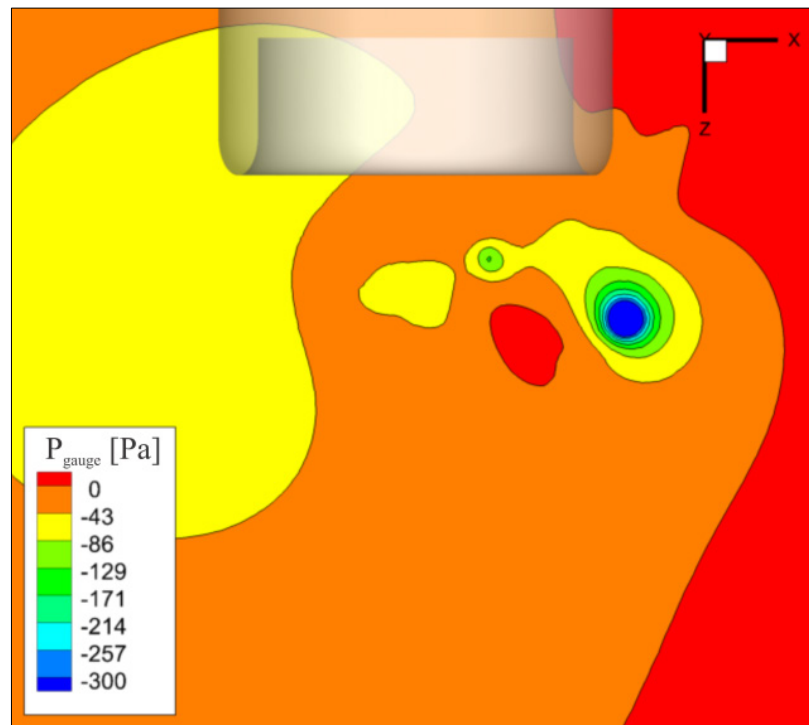
The near-ground static pressure contours reveal the presence of one strong core, with 300Pa below gauge suction pressure, and two weaker cores (Figure 6.8(b)). As in the previous time step, these pressures are not low enough to cause FOD concerns. Additionally, the near-ground static pressure and out-of-plane vorticity contours (Figure 6.8(c)) suggest that the strength of the vortex is independent of the distance from the suction plane to the vortex's attachment point on the group. The strongest vortex is located downstream of the inlet – the farthest from the suction plane of all the ground vortices – and contains considerably more vorticity than the other two vortices. This supports the explanation that the strength of the vortices is dependent primarily on the vorticity generation within the boundary layers of the flow, rather than its proximity to the inlet.

The fan face out-of-plane vorticity contours show the ingestion of three inlet vortices, one trailing vortex, and two secondary vortices (Figure 6.8(d)). The secondary vortices are counter-rotating, with the clockwise vortex having the highest strength. These vortices originate on the surface of the nacelle's underside. The iso-surface of vorticity magnitude shown in Figure 6.5(f) illustrates the crosswind effect experienced by the ground-to-inlet vortices. The dashed line shown in Figure 6.8(f) separates the approximate regions of crosswind flow and suction flow dominance; below the line, the vortex cores are seen to bend in the downwind direction due to the crosswind dominance, whereas above the line, they are seen to move predominantly in the YZ plane, with inlet suction effects dominating.

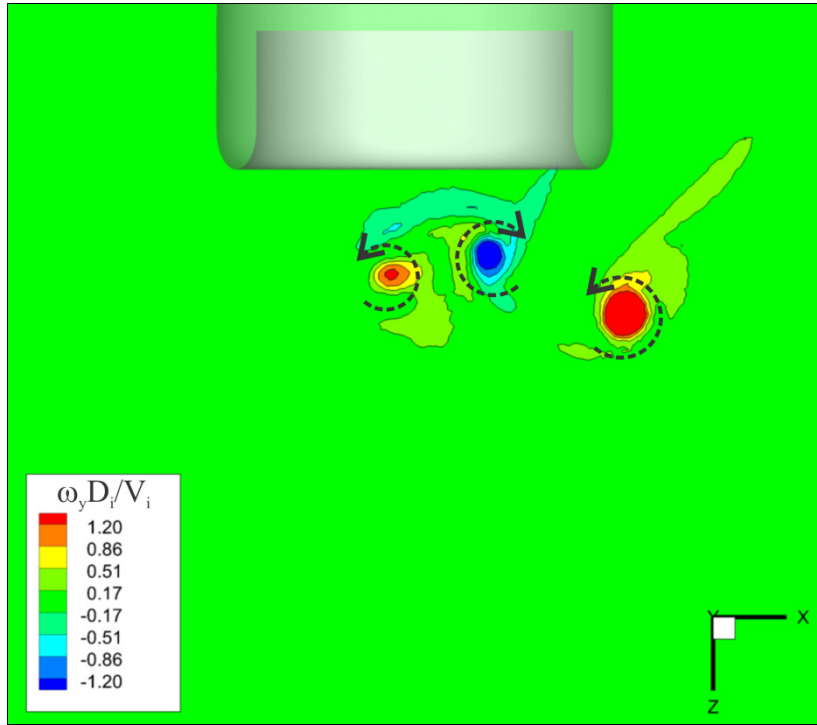
The stagnation pressure contours, shown in Figure 6.5(e) for this time step, reveal the trailing, inlet and secondary vortex core ingestion locations, as well as a pronounced lip separation region. The profile is nearly identical to Figure 6.7(e) from the previous time step, but with a clearer secondary vortex ingestion region. Figure 6.8(g) summarizes the flow field at time step 0.56s, showing the vortex filament sketch.



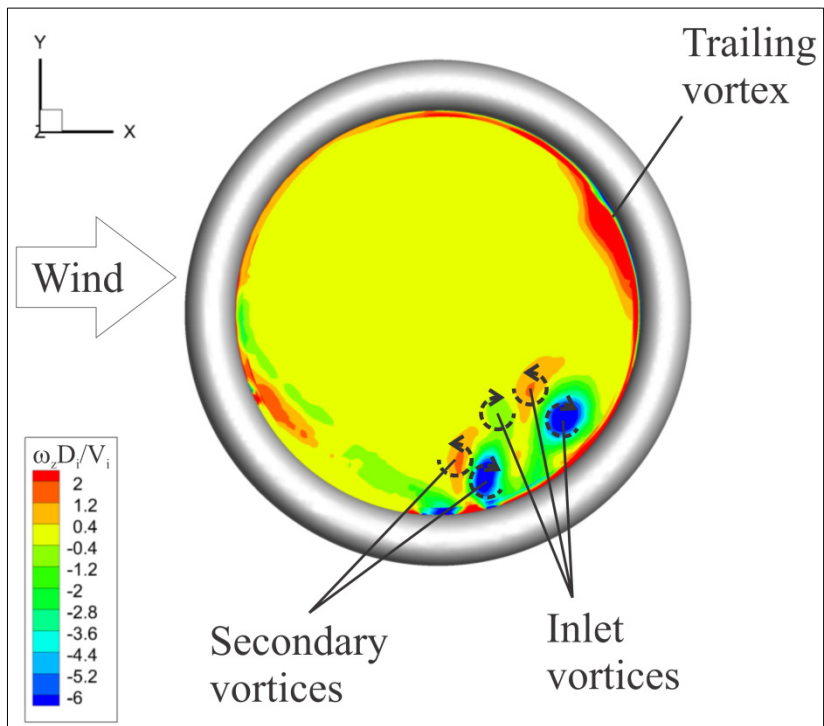
(a)



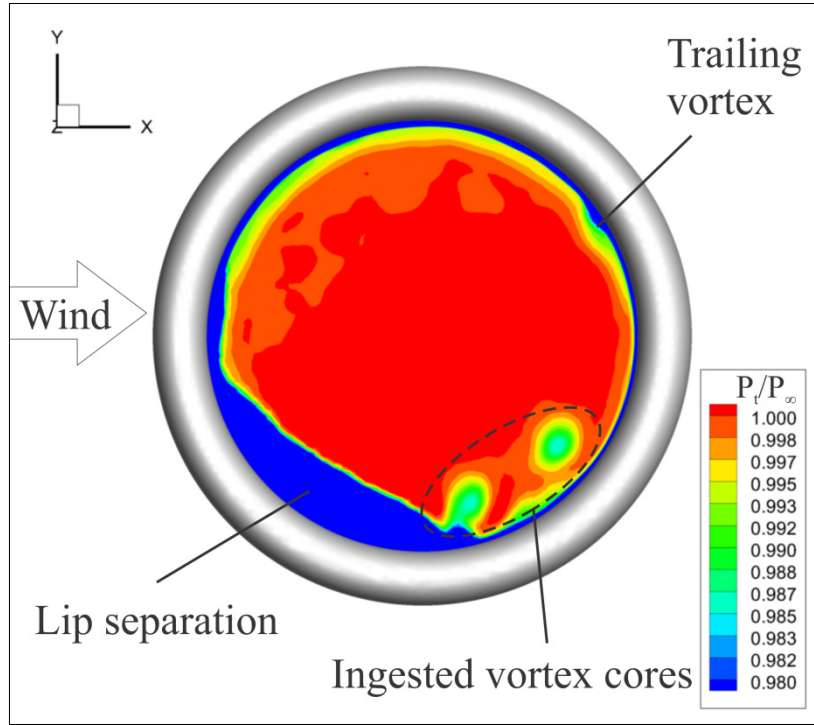
(b)



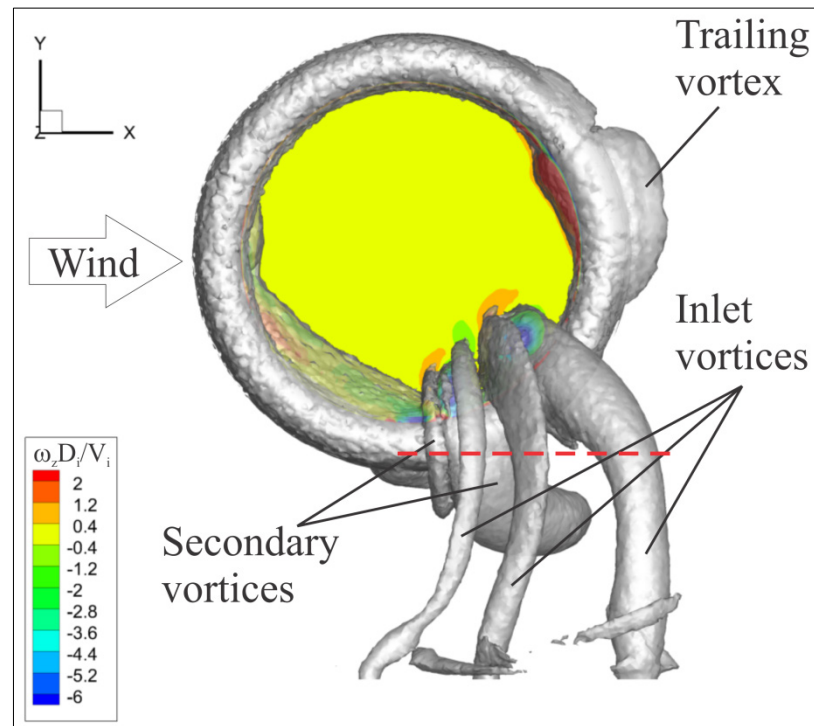
(c)



(d)



(e)



(f)

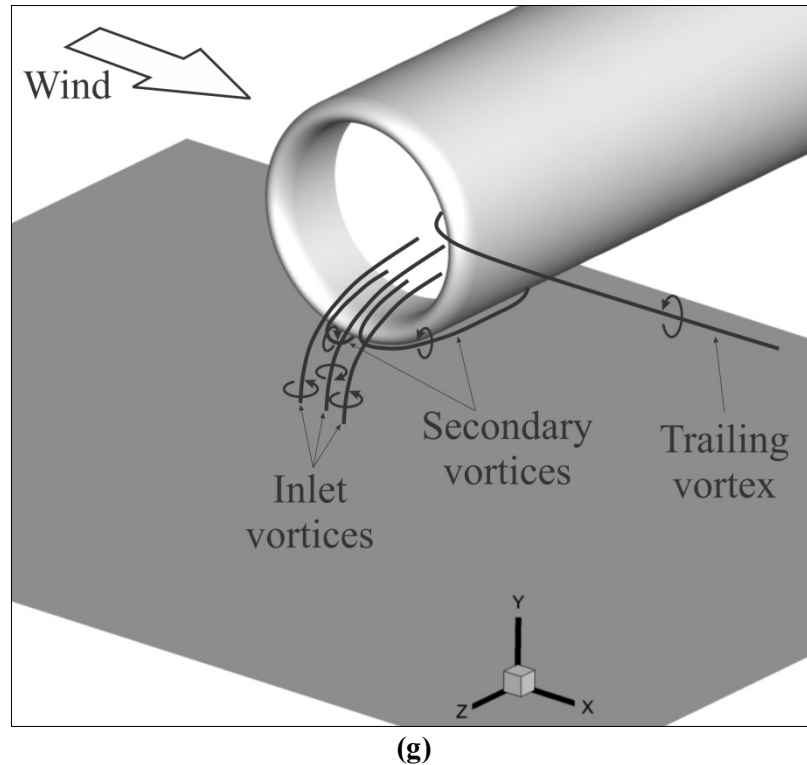


Figure 6.8 (a) Velocity vectors, (b) static gauge pressure contours, and (c) out-of-plane vorticity contours on near-ground plane, followed by (d) out-of-plane vorticity contours and (e) stagnation pressure on the fan face plane, accompanied by (f) vorticity magnitude iso-surfaces to visualizing vortex core profiles and (g) vortex filament sketch summarizing the flow field at time 0.56s.

6.3.5 Step-change in farfield wind speed – time step 0.65s

At this time step, the farfield velocity boundary condition has changed from 10m/s to 7m/s, and the nearfield crosswind speed is beginning to adapt to the new wind profile. Figure 6.9(a), (b) and (c) reveal the existence of three inlet vortices, two rotating in a clockwise direction and another counter-clockwise. As in the two previous time steps (0.49s and 0.56s), the counter-clockwise vortex is the strongest, contains the highest level of vorticity and produces the largest amount of suction on the ground plane (Figure 6.9(b)). The size of this vortex also appears to increase with time, as evidenced by the near-ground vector plot, out-of-plane vorticity, and near-ground pressure contours (Figure 6.9(a), (b) and (c)). The reason for this is that the dominant

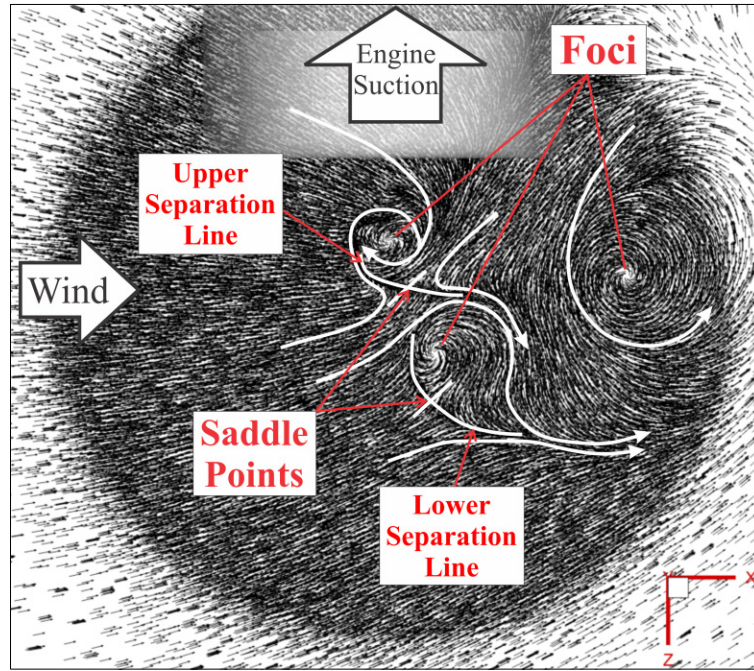
vortex is still developing and a steady-state flowfield has not been reached. Therefore, the vortex can be expected to increase in strength until it is fully developed.

Figure 6.9(a) shows an interesting phenomenon occurring. The separation lines developed by the saddle points are actually inducing a growth in the size of the downstream counter-clockwise vortex. The air flowing along the lower separation line curls upward (in the negative Z direction) and is entrained by this vortex's swirling flow, adding to its mass flow and increasing its diameter. The upper separation line joins the two clockwise-rotating vortices and creates significant flow blockage, which in turn allows more downstream air to be entrained by the counter-clockwise vortex's flowfield.

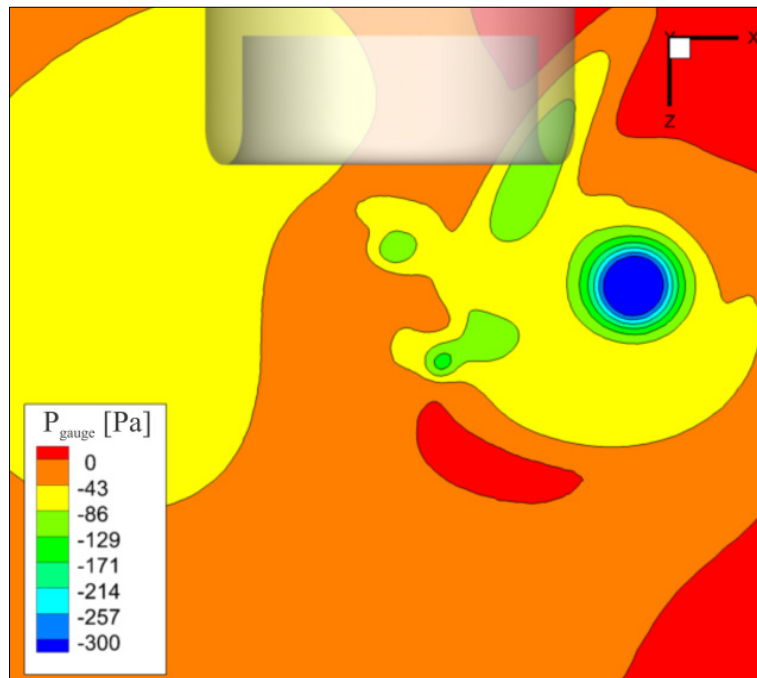
Figure 6.9(d) shows the ingested areas of the trailing, inlet and secondary vortices. The areas of both the trailing and inlet vortices display an increase in size, suggesting more flow was being convected to the outer core of the trailing vortex. One secondary vortex is present as well, and although its strength is comparable to the stronger of the inlet vortices, its diameter is smaller. Some vorticity is also observed in the lip separation region, but not nearly as large as the ingested vortex cores. Even though the trailing vortex displays an increase in size as described above, its low-pressure core appears to be small compared to its outer flow diameter and is ingested at the fan face 1 o'clock location (Figure 6.9(e)). A lip separation region is also present and remains nearly identical to the previous time step.

The three-dimensional profile of each vortex characterizing the flowfield at this time step is depicted in Figure 6.9(f) by iso-surfaces of vorticity magnitude. The rightmost inlet vortex (clockwise rotation on the fan face plane) has to bend significantly in order to be ingested by the inlet due to its downstream position. Smaller vortical structures generated near the ground plane and around the vortex cores are also present. These are associated with the vorticity induced by

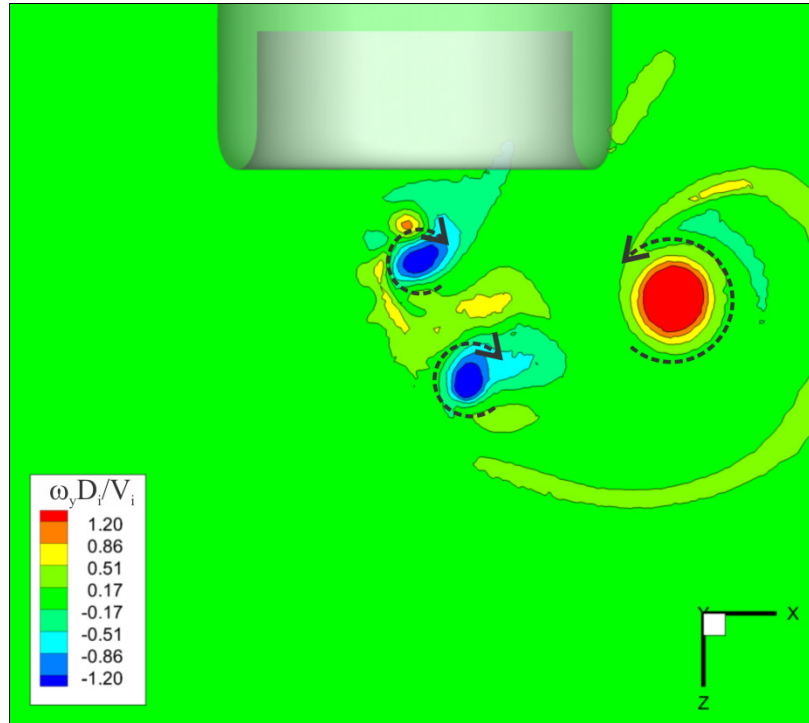
the ground-to-inlet vortices, but are not a part of the individual vortex cores. Figure 6.9(g) summarizes the flow field at time step 0.65s, showing the vortex filament sketch.



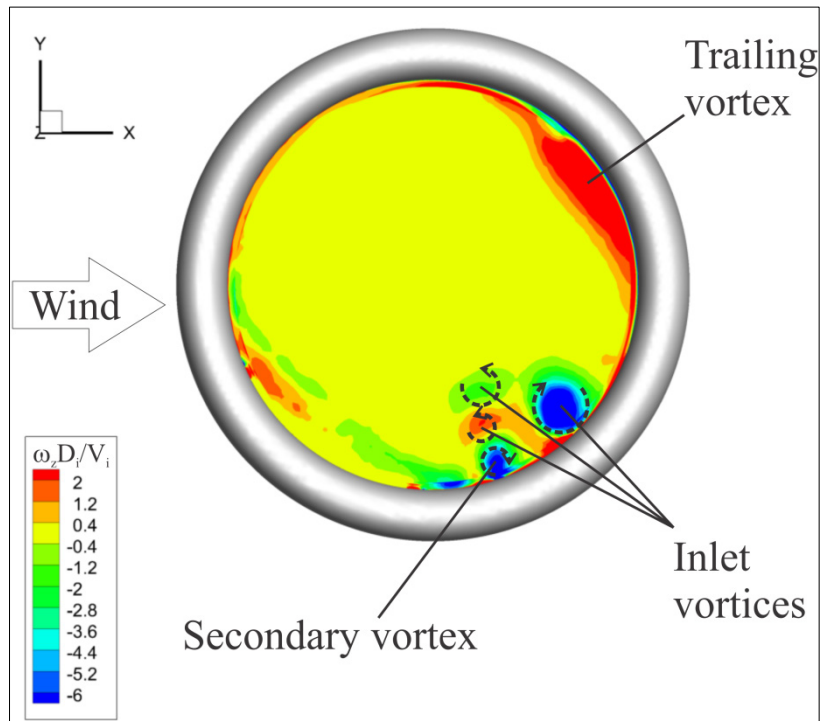
(a)



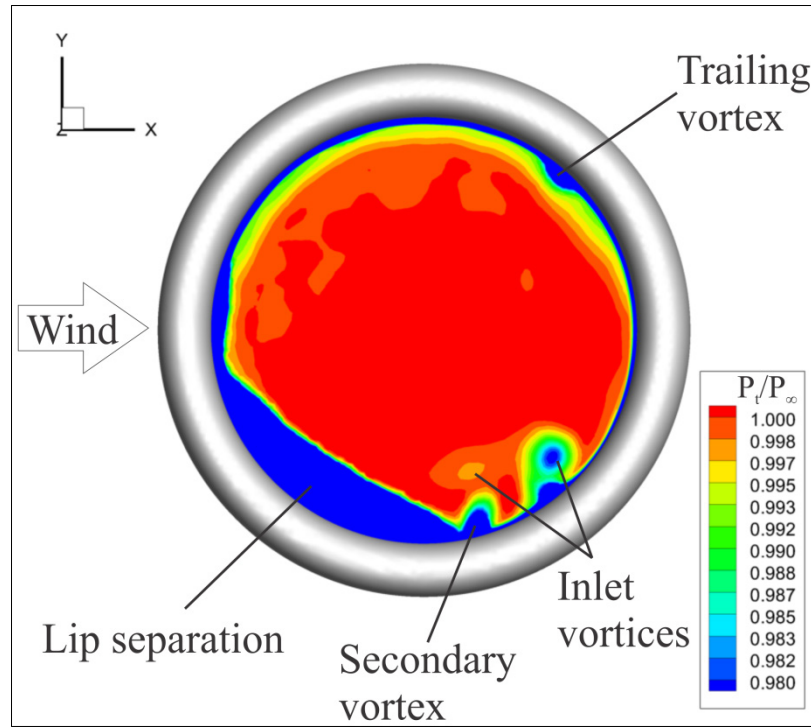
(b)



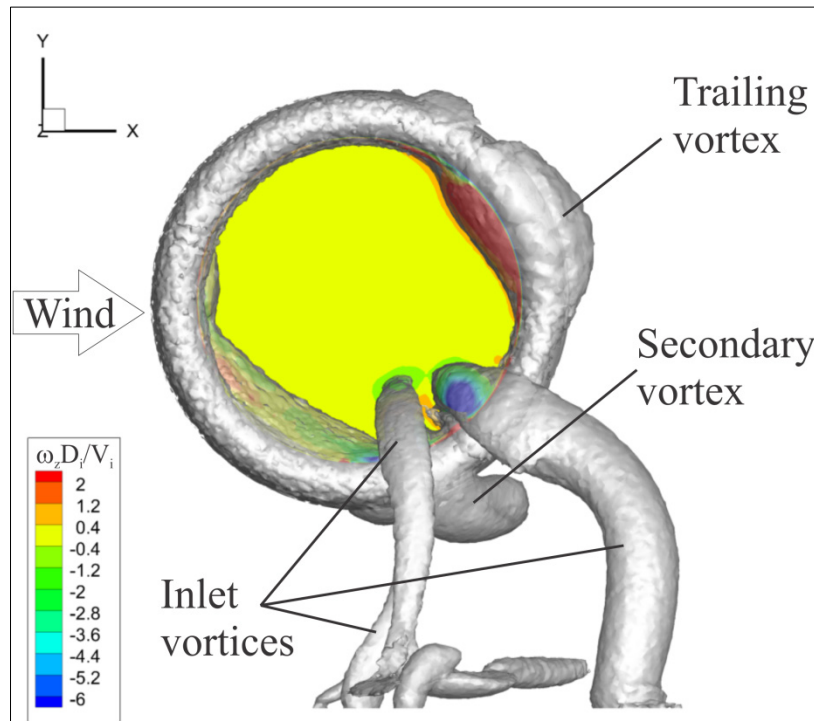
(c)



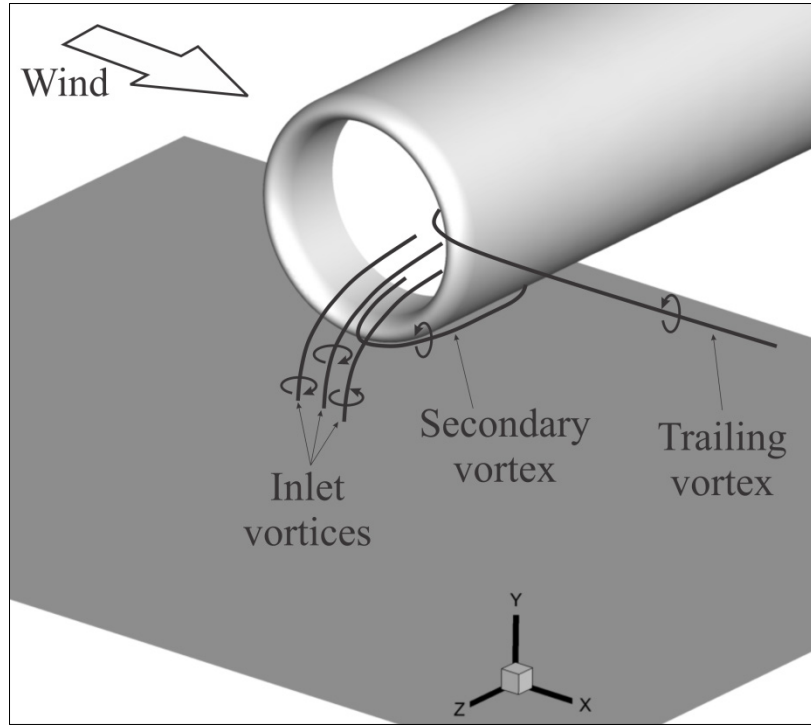
(d)



(e)



(f)



(g)

Figure 6.9 (a) Velocity vectors, (b) static gauge pressure contours, and (c) out-of-plane vorticity contours on near-ground plane, followed by (d) out-of-plane vorticity contours and (e) stagnation pressure on the fan face plane, accompanied by (f) vorticity magnitude iso-surfaces to visualizing vortex core profiles and (g) vortex filament sketch summarizing the flow field at time 0.65s.

6.3.6 Three vortices shift upstream – time step 0.80s

The flowfield at time step 0.80s is very similar to the previous time step (0.65s), containing two clockwise-rotating vortices, one counter-clockwise, one trailing and one secondary vortex. The dominant vortex is again the counter-clockwise vortex, which has now moved slightly upwind. This is expected since the nearfield wind speed is decreasing at this time step, offering less resistance to the inlet suction effects. Flowfield topology of the near-ground plane reveals the presence of three foci points formed as a result of two saddle points, as expected for the three-vortex configuration (Figure 6.10(a)).

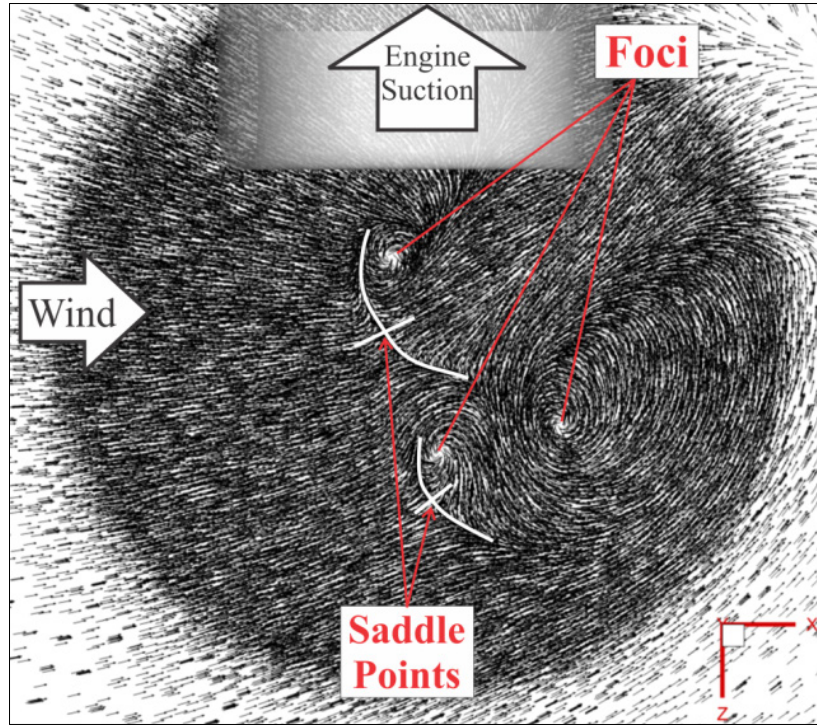
One difference from the previous time step, however, is that the lower of the two clockwise-rotating vortices has lost some of its strength (Figure 6.10(c)). As will be discussed in section 6.4.2, the inlet vortex circulation plot reveals that the combined negative circulation of both clockwise vortices still increases though. Some possible explanations for this are as follows:

1. This particular vortex has lost vorticity by convecting it through its core and into the fan face due to the inlet suction effect; because of the decrease in crosswind speed, less vorticity is being produced within the ground and nacelle boundary layers and therefore less vorticity is available for convection through its core.

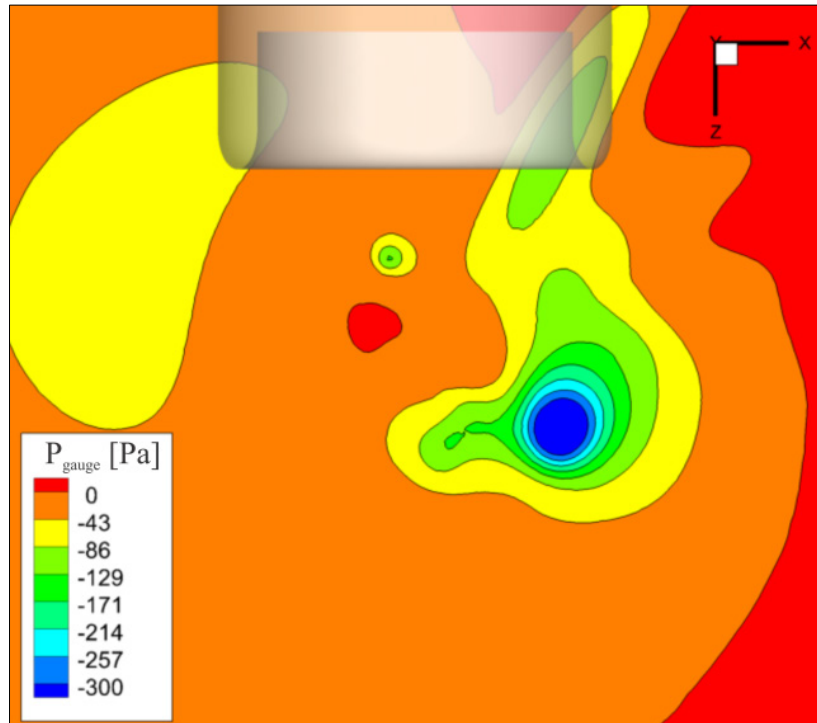
2. There is an unknown mechanism by which vorticity is transferred from one inlet vortex to another during this transient formation process.

This clockwise vortex also happens to be the one most exposed to the crosswind effects, since it is farther away from the engine in the axial direction and lies in front of the counter-clockwise vortex. It suggests that the effects of a decreased wind speed are seen first by this vortex.

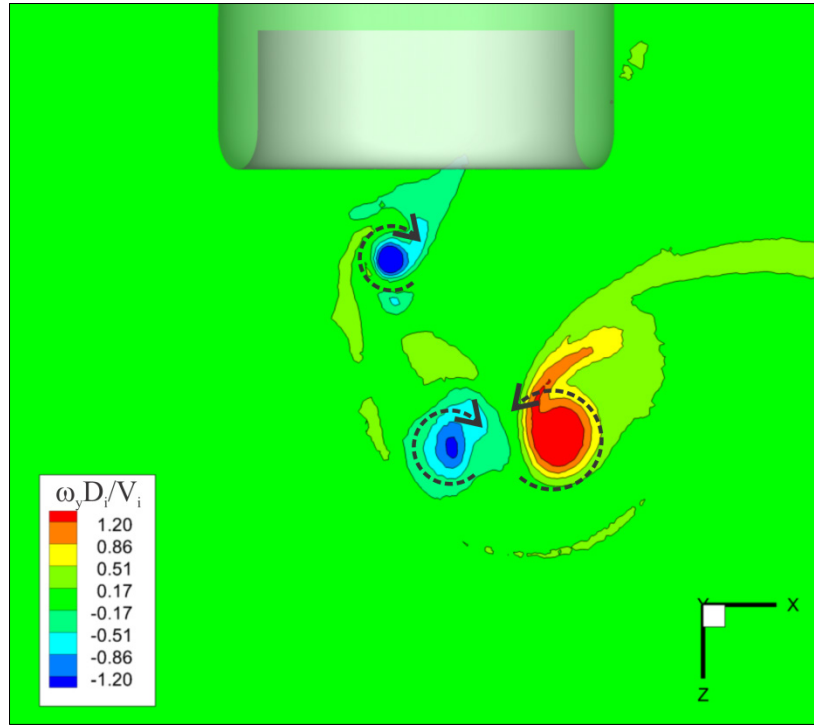
Figure 6.10(d), (e) and (f) describe the flowfield characteristics at this time step, and Figure 6.10(g) summarizes the vortex profiles by sketching their filaments.



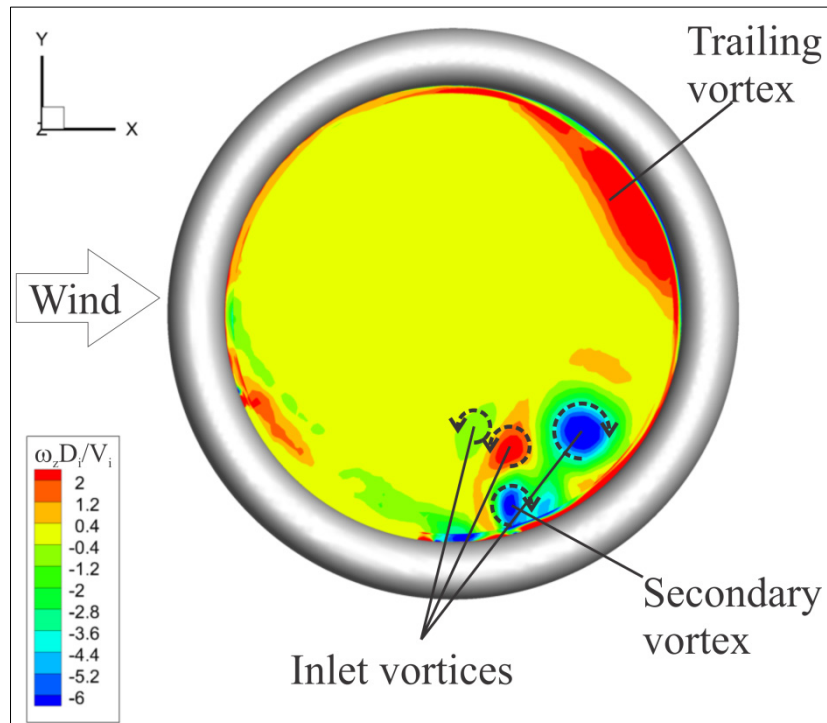
(a)



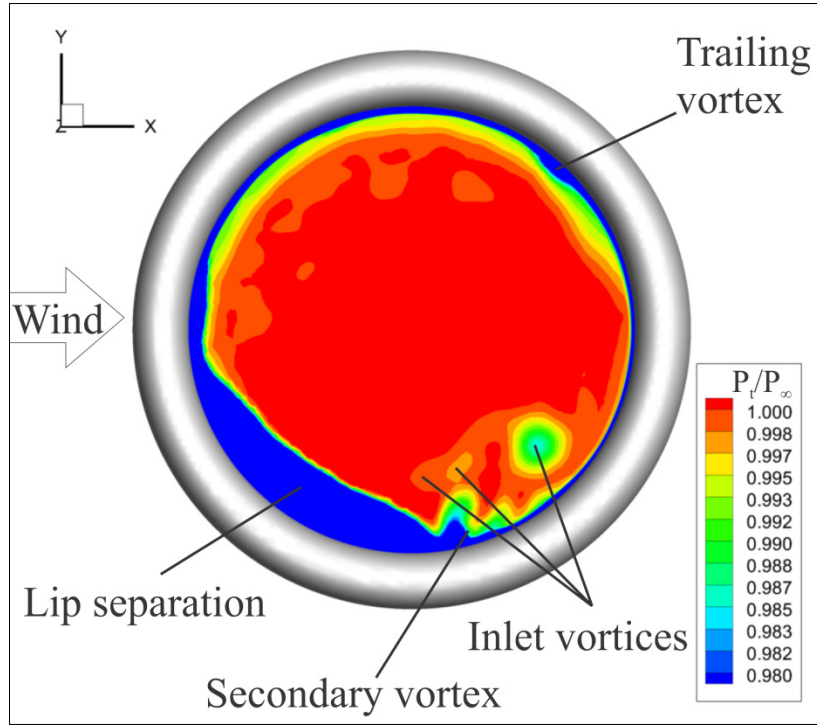
(b)



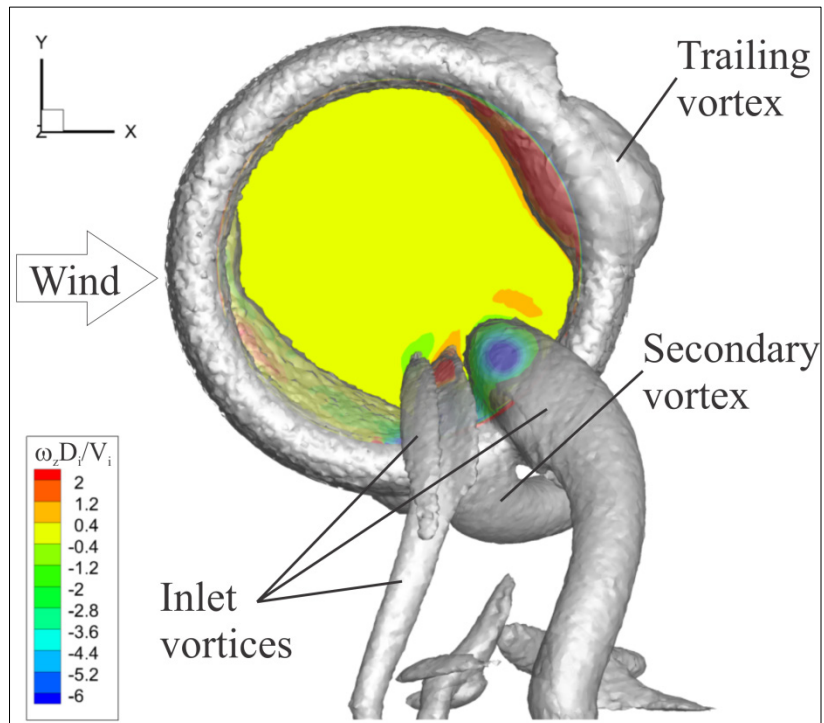
(c)



(d)



(e)



(f)

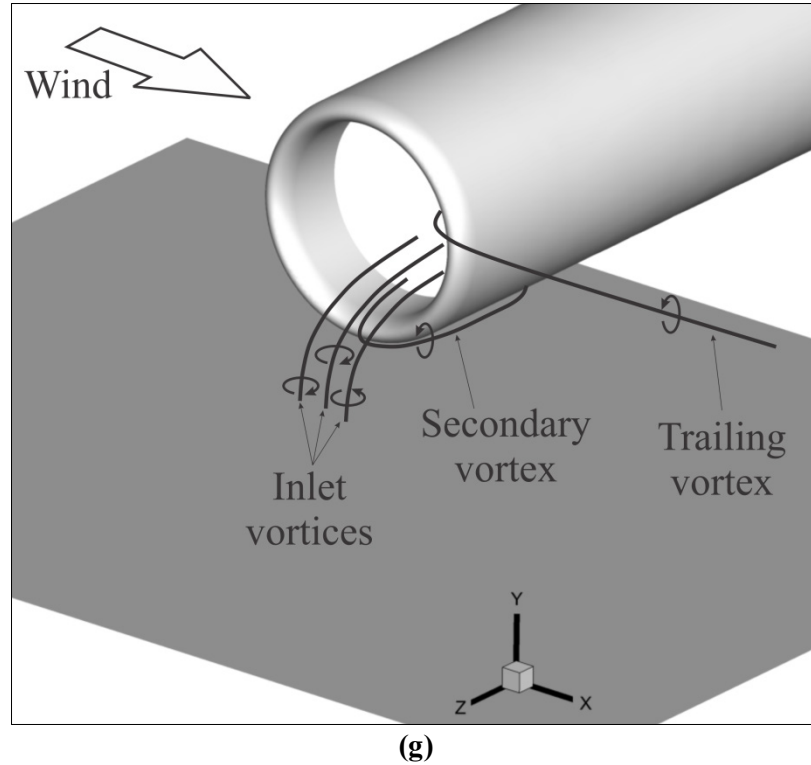


Figure 6.10 (a) Velocity vectors, (b) static gauge pressure contours, and (c) out-of-plane vorticity contours on near-ground plane, followed by (d) out-of-plane vorticity contours and (e) stagnation pressure on the fan face plane, accompanied by (f) vorticity magnitude iso-surfaces to visualizing vortex core profiles and (g) vortex filament sketch summarizing the flow field at time 0.80s.

6.3.7 Vortex coalescing – time step 0.95s

At this time step, the nearfield crosswind speed is 8.3m/s and is still decreasing to match the specified farfield value of 7.3m/s (see Figure 6.2(a)). Figure 6.11(a)-(c) reveal a drastic difference in the flowfield from previous time steps; it now shows the existence of a single inlet vortex (one focus point and no saddle points), suggesting the multiple vortices observed earlier have coalesced into a single one.

Compared to the previous time step, which contains a vortex with counter-clockwise rotation as this one, this vortex has grown significantly in size and moved closer towards the inlet in the axial direction while maintaining its X position. With a further decrease in crosswind

speed, the core is expected to move upstream and reach a steady-state location around the axis of the inlet.

Additionally, the suction strength of this one inlet vortex has dramatically increased, as evidenced by the pressure contours shown in Figure 6.11(b). A gauge pressure of -2000Pa at the vortex's core can lift up a spherical chunk of pavement 12cm in diameter and weighing almost 3kg. FOD is now a serious concern to engine operability and passenger safety. As the velocity ratio is further increased, this suction strength will increase, making FOD an even greater problem.

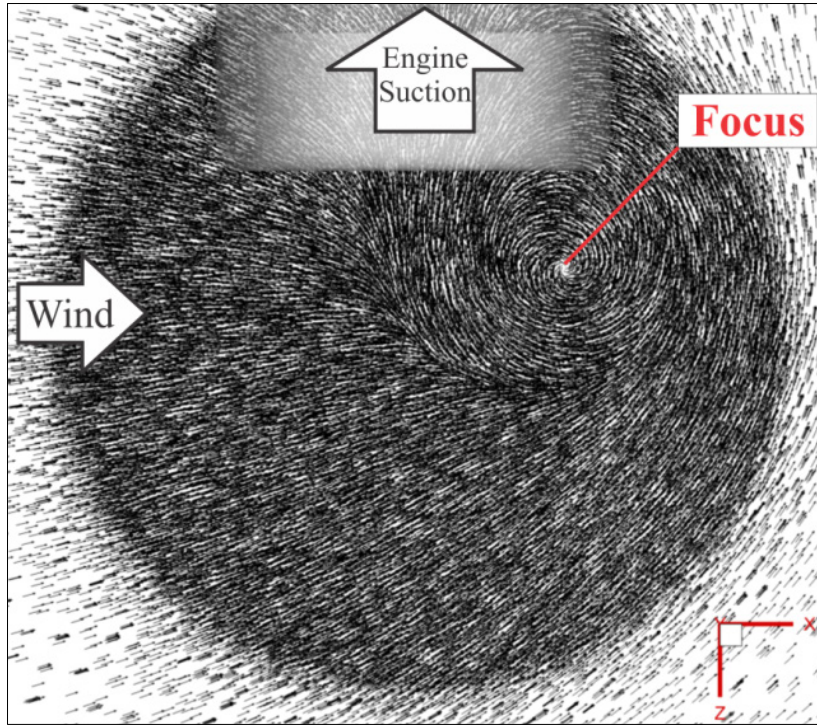
Figure 6.11(c) and (d) shows the out-of-plane vorticity contours at the near-ground and fan face planes. Although the Y vorticity scale has been kept the same throughout all time steps, the results show that its maximum value has increased (evidenced here by the pressure contours). Vorticity is also produced underneath the engine and near the ground, where the upstream and downstream flows meet (Figure 6.11(a), (c)). This region corresponds to one side of a saddle point located far aft of the engine lip plane (not shown in the figure), and also contributes to the increase in vortex strength.

The vorticity contours at the fan face (Figure 6.11(d)) reveal the existence of only one ingested inlet vortex, accompanied by one secondary and one trailing vortex. The inlet vortex contains higher vorticity at the ingestion location, whereas the secondary contains less. De Siervi *et al.* (1982) observed that the total circulation of the inlet vortex system remains constant. The research shown here supports this observation as will be addressed in section 6.4.5 and shown in Figure 6.18(b). However, to maintain this balance in circulation without generating additional vorticity within the system suggests a transfer of vorticity from one vortex to another. This concept may describe the mechanism of vortex coalescence, as well as a possible exchange of

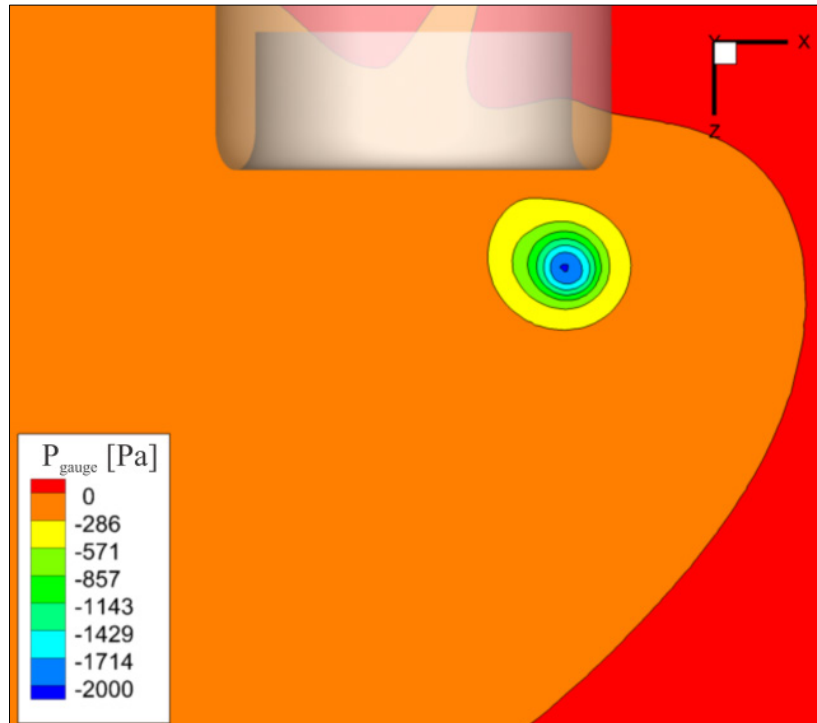
vorticity between the trailing and secondary vortices, since both of these obtain their vorticity from the same source.

The stagnation pressure contours at the fan face reveal the existence of a bi-fold lip separation and show the distortion caused by the inlet vortex (Figure 6.11(e)). The distortions due to the secondary and trailing vortices are small compared to the lip separation and inlet vortex. The ingested inlet vortex core creates more distortion and pressure losses than in previous time steps (as will be clarified by the DC_{60} time history plot in section 6.4.6). This is simply due to the ingestion of a stronger vortex. The lip separation region has a peculiar shape at this time step, and the reason for this is unknown. Additionally, the inlet vortex and lip separation regions have rotated slightly clockwise; the vortex is at a 4 o'clock position at time step 0.80s, and is now at a 5 o'clock position. This is attributed to the decrease in the nearfield crosswind speed, reducing the downwind force acting on the vortices and allowing for ground attachment and ingestion to occur farther upstream.

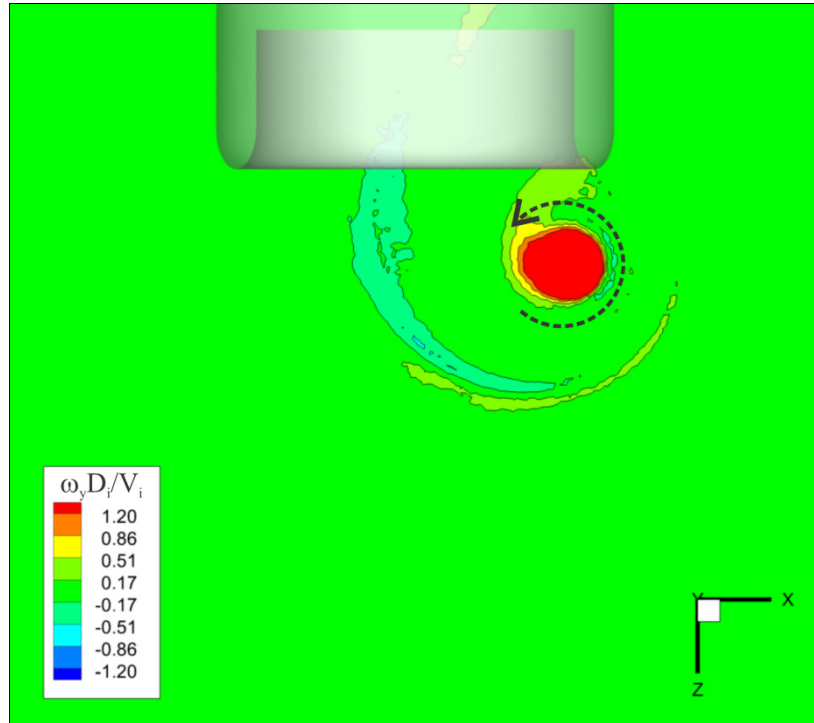
This time step contains a strong inlet vortex, accompanied by weaker secondary and trailing vortices. The iso-surfaces of vorticity magnitude for this system are shown in Figure 6.11(f), capturing the three-dimensionality of the inlet and secondary vortices, as well as the vorticity generated within the separation bubble. The trailing vortex core is not captured due to its lower vorticity level at the fan face plane location. In order to capture the cores, the vorticity level had to be increased to $3000s^{-1}$, a significant increase compared to $1000-2000s^{-1}$ levels for previous time steps. Figure 6.11(g) summarizes the flow field at time step 0.95s, showing the vortex filament sketch.



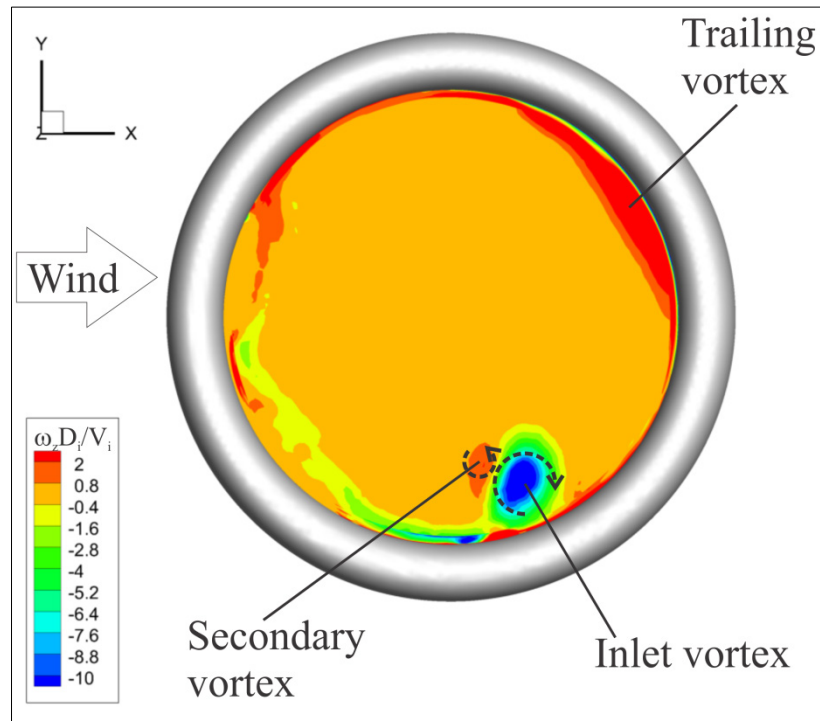
(a)



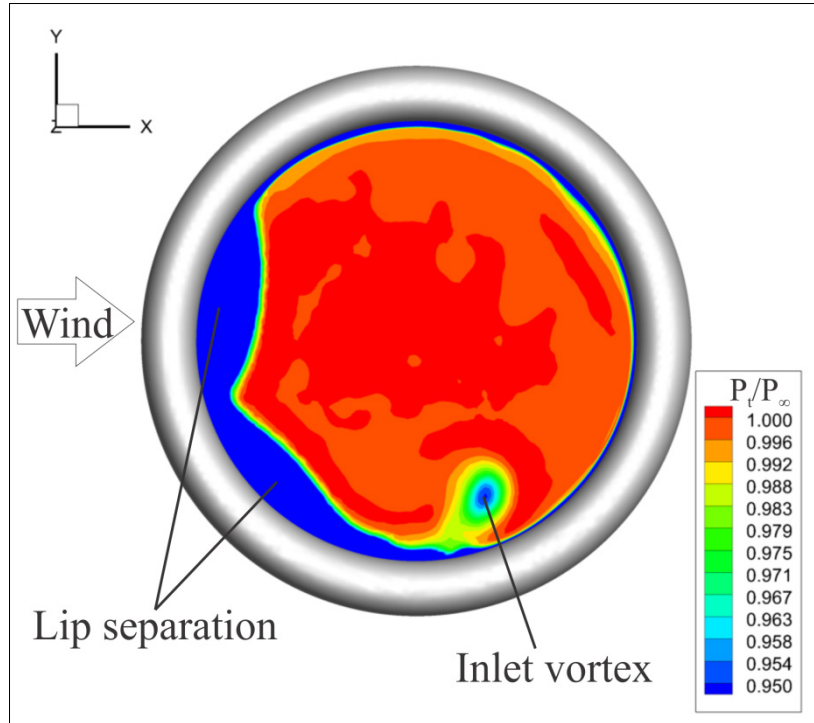
(b)



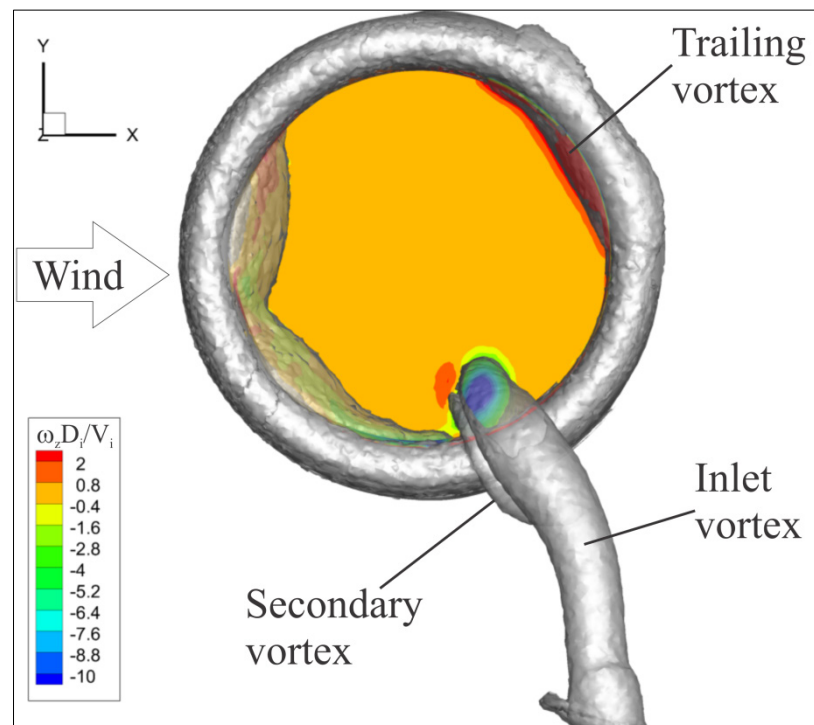
(c)



(d)



(e)



(f)

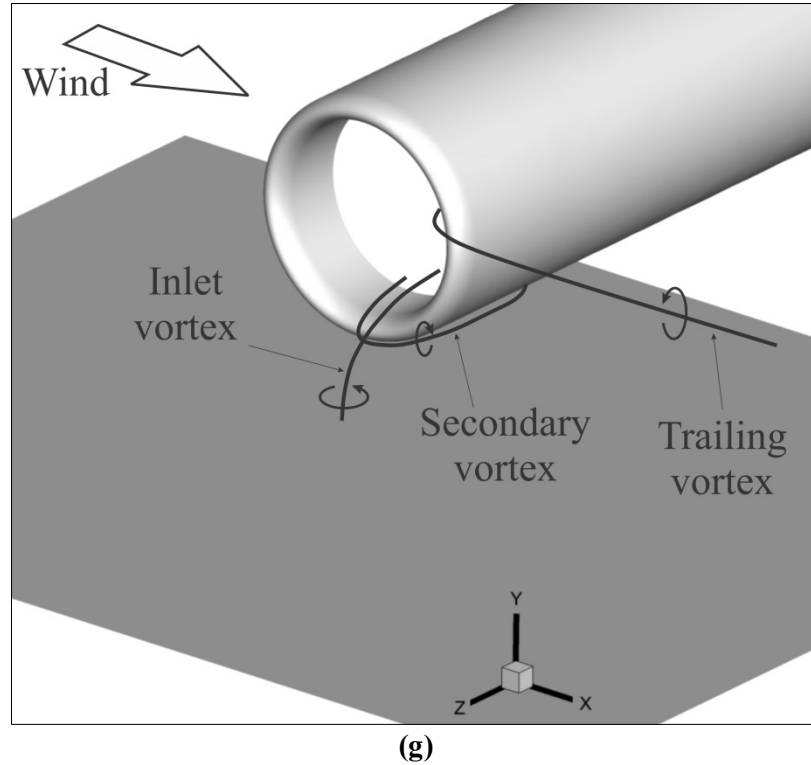


Figure 6.11 (a) Velocity vectors, (b) static gauge pressure contours, and (c) out-of-plane vorticity contours on near-ground plane, followed by (d) out-of-plane vorticity contours and (e) stagnation pressure on the fan face plane, accompanied by (f) vorticity magnitude iso-surfaces to visualizing vortex core profiles and (g) vortex filament sketch summarizing the flow field at time 0.95s.

6.3.8 Final time step, 1.15s

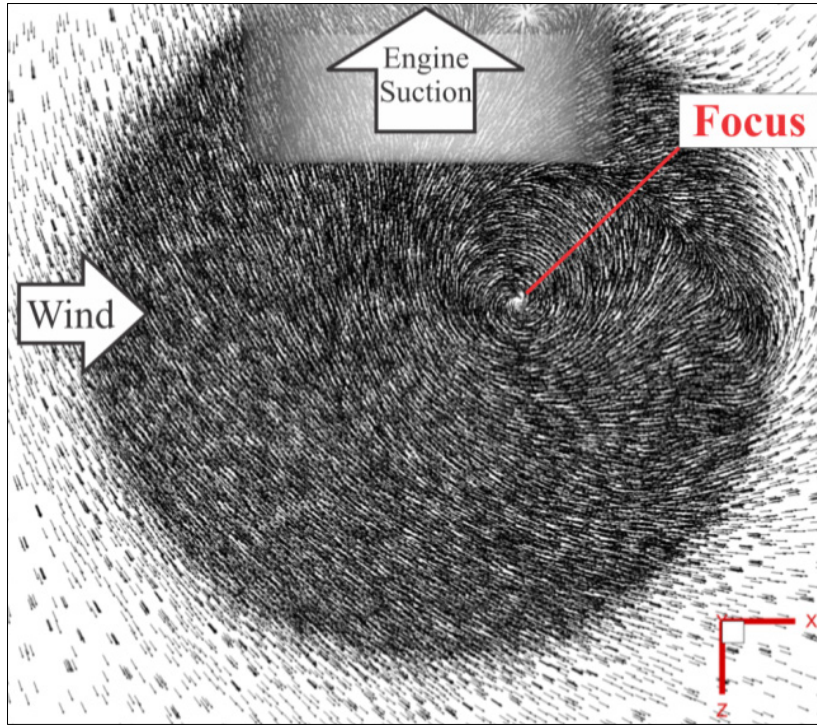
This is the final time step studied in the present research, and according to the velocity profile of Figure 6.2(a), the nearfield crosswind speed has reached the specified farfield boundary condition. The near-ground vector plots, flow topology and pressure contours show the existence of a single inlet vortex (one focus point), which has shifted upwind but is still slightly downwind of the engine axis (Figure 6.12(a) and (b)). The vortex did not grow in size but its suction strength continues to increase, as seen by the core pressure of 2700Pa below gauge. This pressure leads to serious FOD concerns, as this pressure could cause the engine to ingest an 18cm-diameter chunk of concrete weighing almost 7kg. The near-ground suction region has a well-defined circular

shape and borders the inlet vortex core. This means that the area in red on Figure 6.12(b) which surrounds the inlet vortex will not experience any suction effects. Therefore, the location where objects may be picked up from the ground is smaller than in any previous time step.

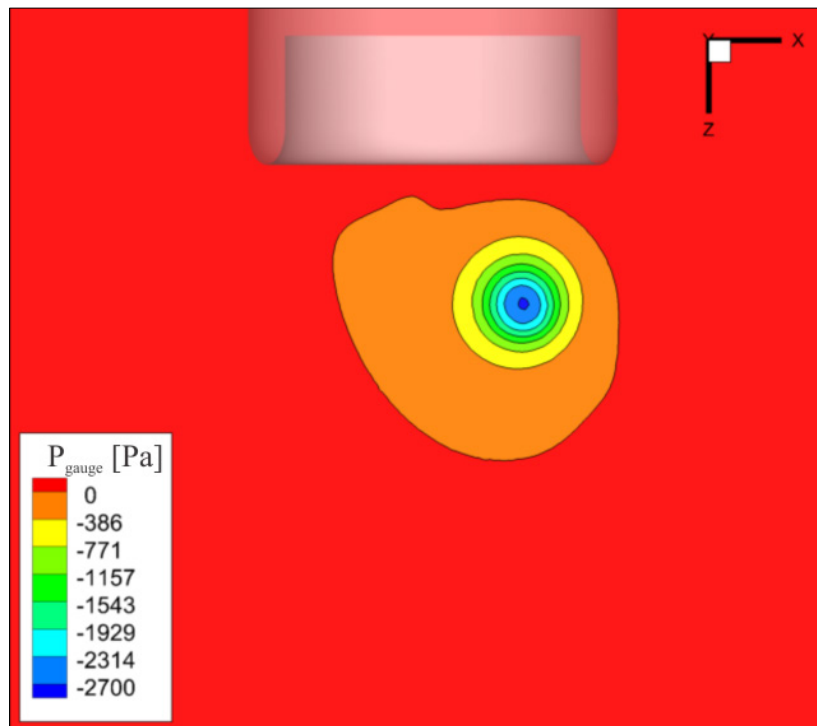
Figure 6.12(c) and (d) show the out-of-plane vorticity contours at the near-ground and fan face planes. At the ground, the contours resemble the previous time step; however the core vorticity has increased. The ingested vorticity, due to the both the inlet and secondary vortices, has increased in magnitude and shows both vortices rotating in a counter-clockwise direction. The trailing vortex ingestion region is not clearly defined.

The fan face stagnation pressure contours reveal a clockwise shift in the lip separation region, while the vortex ingestion locations remain the same (Figure 6.12(e)). The distortion created by the vortices and lip separation has increased in comparison to the previous time step and is linked to the transient behavior of the system. The full fan-face DC_{60} is significantly higher than the modified inlet vortex DC_{60} , having increased from 0.3 at time step 0.9504s to 0.42. The distortion due to the vortices remains constant during these two time steps (see section 6.4.6).

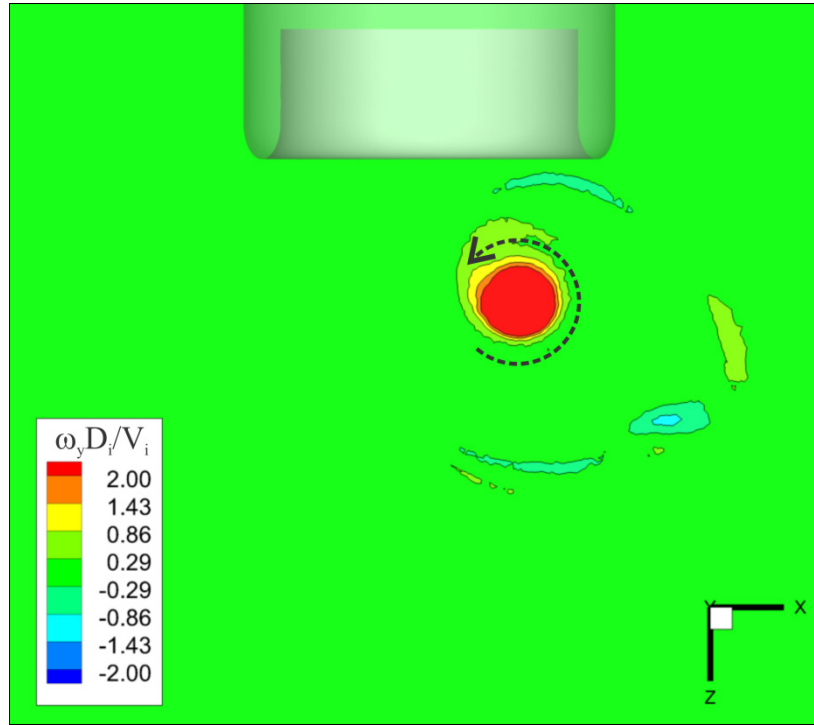
The vortex cores are depicted by vorticity magnitude iso-surfaces at a level of $2000s^{-1}$ in Figure 6.12(f), clearly illustrating the inlet and secondary vortex cores. Additionally, the inlet and trailing vortex cores are shown in Figure 6.12(g) by using streamtraces in Tecplot. The figure shows the profile of the inlet's capture streamtube, evidenced by the ingested streamlines. The core of the inlet vortex is considerably smaller in diameter when compared to the trailing vortex and its core flow travels strictly into the inlet. Conversely, the trailing vortex contains an inner core flow, which travels in the negative X direction and is ingested by the inlet, as well as an outer flow which is not captured by the inlet and flows in the positive X direction downwind. This observation is in agreement with De Siervi *et al.* (1982) and Trapp and Girardi (2012). Lastly, Figure 6.12(h) summarizes the flowfield with vortex filament lines.



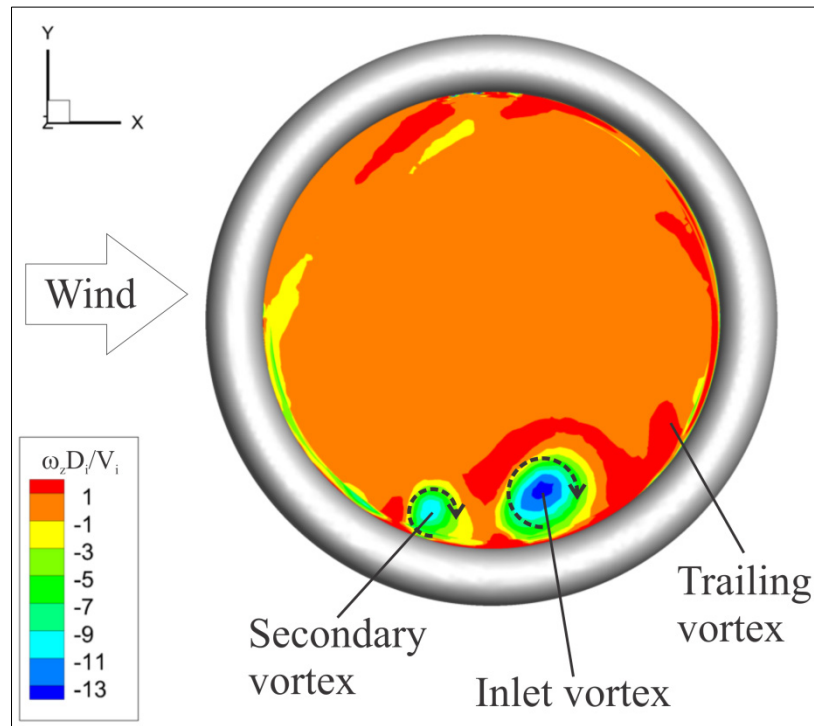
(a)



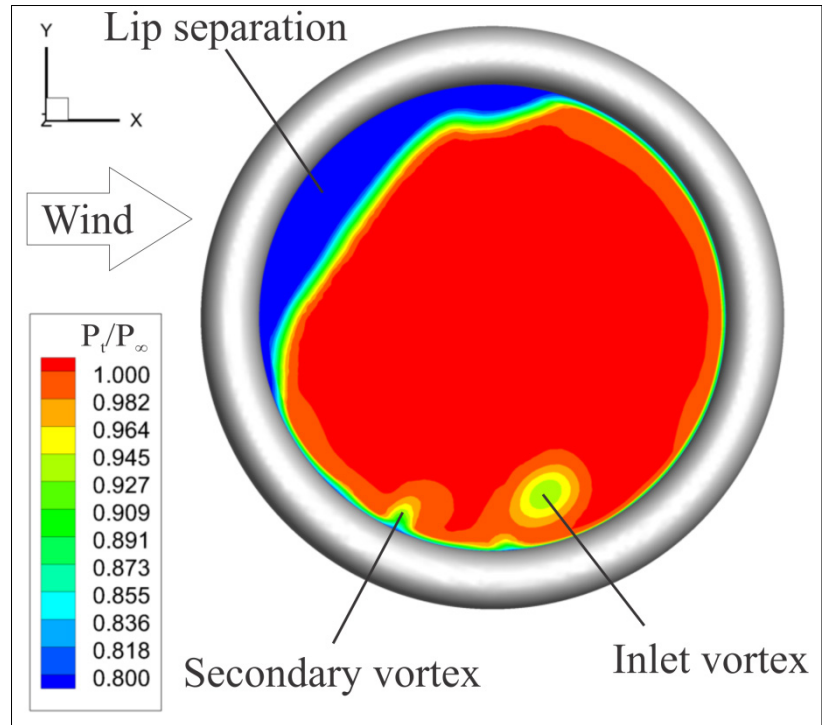
(b)



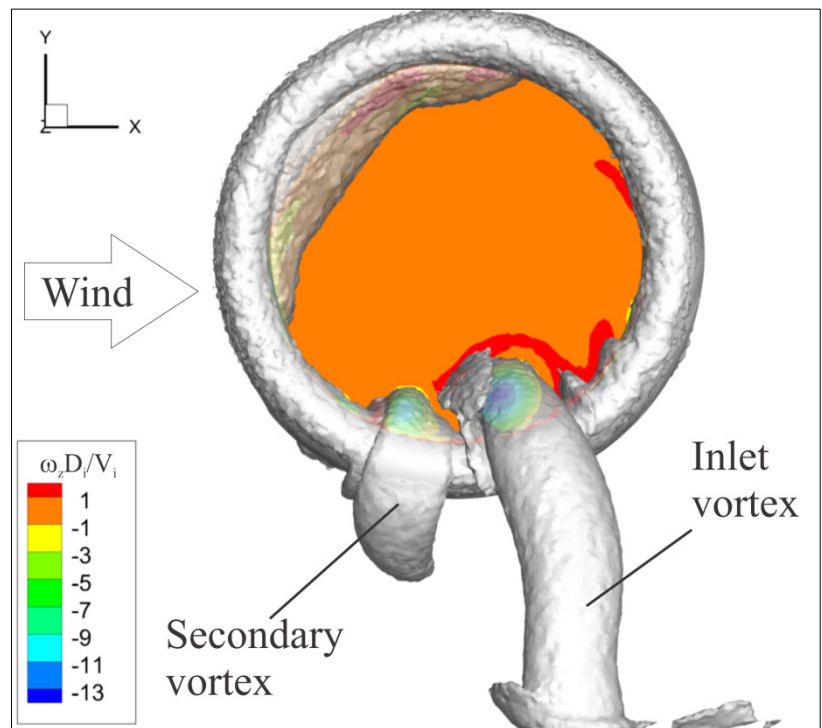
(c)



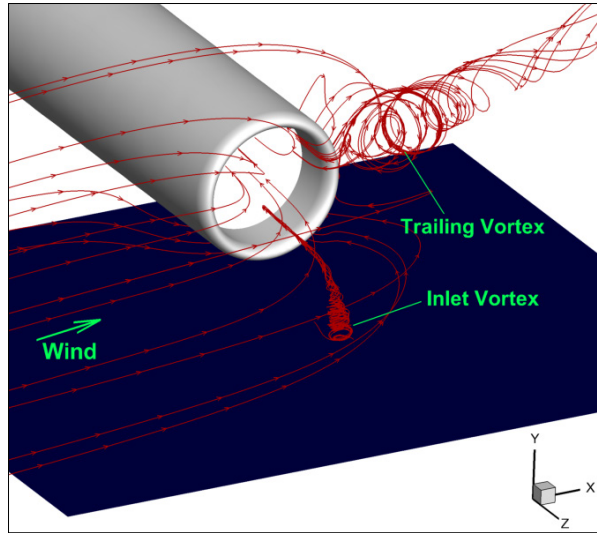
(d)



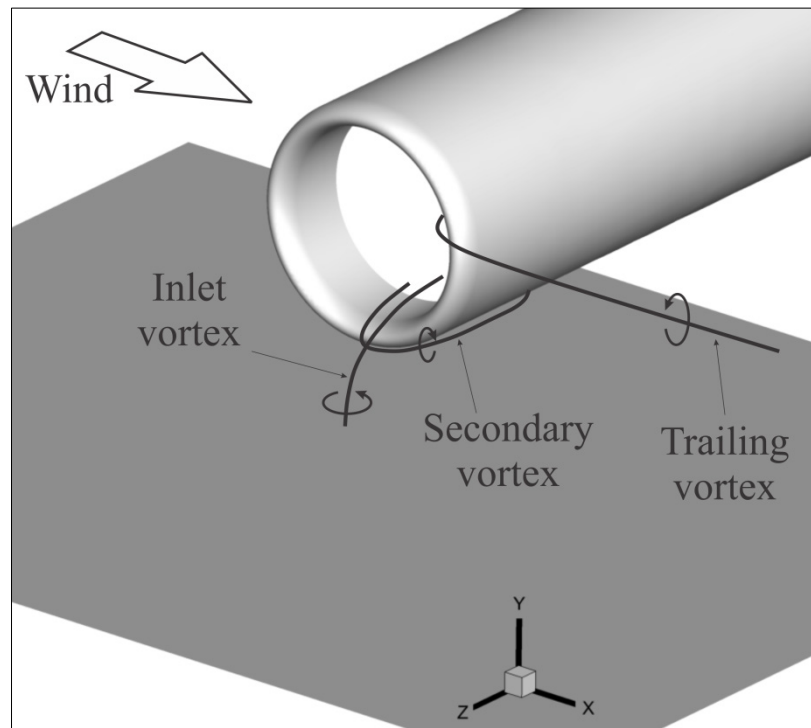
(e)



(f)



(g)



(h)

Figure 6.12 (a) Velocity vectors, (b) static gauge pressure contours, and (c) out-of-plane vorticity contours on near-ground plane, followed by (d) out-of-plane vorticity contours and (e) stagnation pressure on the fan face plane, accompanied by (f) vorticity magnitude iso-surfaces to visualizing vortex core profiles, (g) inlet and trailing vortex streamtraces and (h) vortex filament sketch summarizing the flow field at time 1.15s.

6.4 Time history of relevant parameters

This section provides time history plots of ground static pressure and circulation for the case studied. The duration of the simulation was exactly 1.15s.

6.4.1 Minimum pressure on near-ground plane

The inlet vortex is characterized by a distinct region of low static pressure inside its core responsible for lifting debris off the ground. Figure 6.13 shows the time history of the minimum near-ground gauge pressure during the formation of the inlet vortex. The values shown were obtained by probing the vortex cores on near-ground pressure contours created in Tecplot and shown in section 6.3. These gauge pressures, together with the area over which they occur, were then used to calculate the diameter and mass of asphalt chunks the inlet could ingest under such circumstances. The results are plotted in Figure 6.14(a) and (b) as time history plots. The assumptions made in calculating the size of asphalt chunk were the following:

1. A spherical shape was assumed;
2. The material was taken to be coarse graded asphalt, often used to pave airport runways, with a density of $2,400\text{kg/m}^3$, assumed uniform;
3. The asphalt chunk was assumed to be lying freely on the surface of the runway and no forces were acting on it besides gravity and inlet suction.

Since the inlet Mach number was matched to that of a representative engine, the pressure values obtained are also representative, and thus no scaling was applied to these calculations.

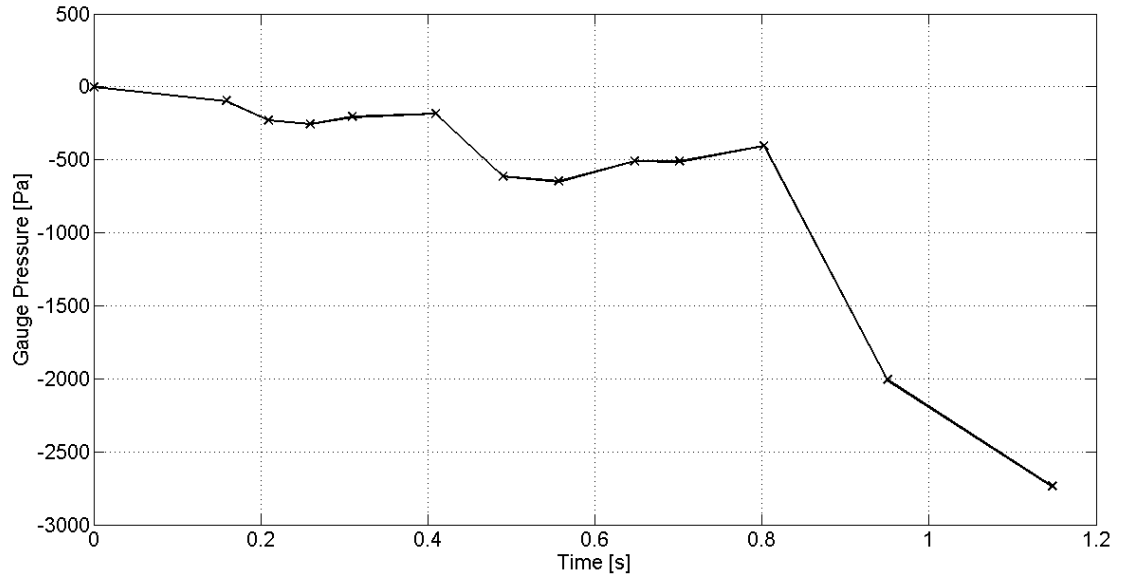


Figure 6.13 Time history of minimum gauge pressure on near-ground plane.

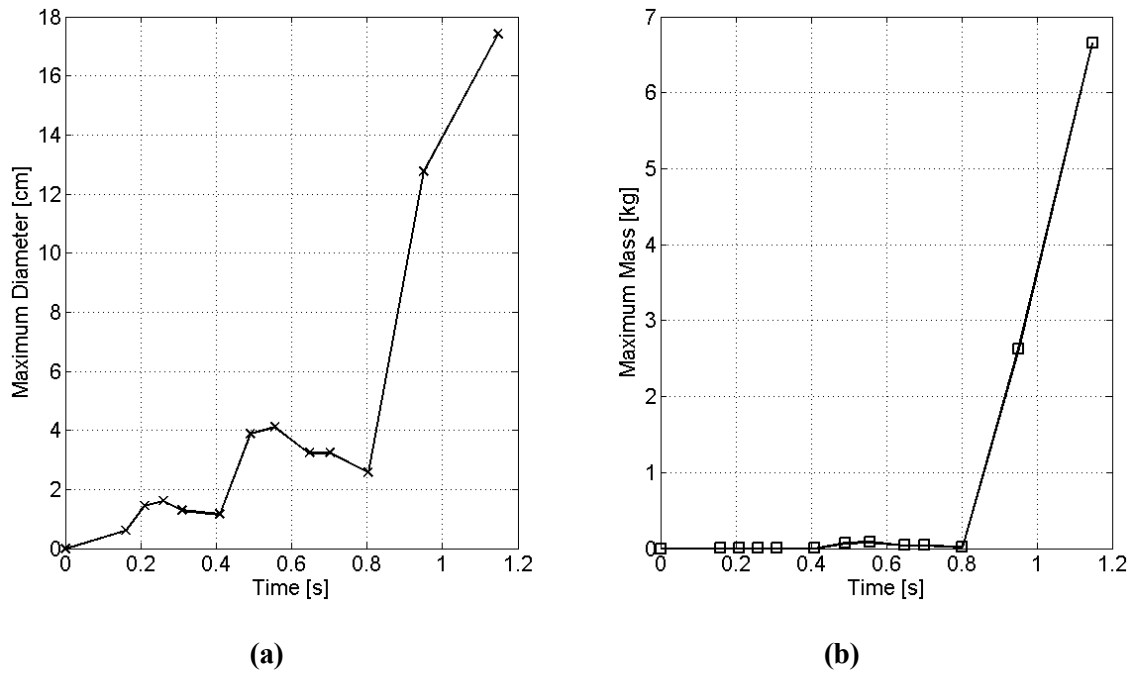


Figure 6.14 Time histories of (a) maximum diameter and (b) maximum mass of asphalt chunk that could be lifted off the ground by the inlet vortices and cause FOD, calculated based on the near-ground plane.

The pressure was observed to be less than 100Pa below gauge for the first 0.2s of flow time, indicating no major suction regions were present on the ground plane despite the existence of two ground vortices during this time period. The size of possible ingested objects was limited to a 2cm diameter, which is no bigger than common gravel. From 0.2s to 0.4s, the pressure dropped to an average of 250Pa below gauge, indicating a slight increase in the suction level on the ground plane. Once again the size of possible ingested objects was very small and hence presented no danger of FOD. Figure 6.2(a) and (b) show that the nearfield crosswind speed reaches the desired value of 10m/s at approximately 0.5s. The ground pressure plot indicates another drop around this time, corresponding to the leveling out of the nearfield crosswind speed. Consequently, the maximum size of a piece of asphalt that could be ingested by the engine has doubled to 4cm in diameter at this time. At around 0.7s the step-change in crosswind velocity takes place, decreasing the farfield wind speed to about 7m/s. The pressure plot reflects this change at approximately 0.8s as the flowfield begins to change close to the inlet. It is clear that near 0.9s, a strong inlet vortex has formed, evidenced by the significant drop in near-ground static pressure. According to the calculations, the engine can now pick up chunks of pavement 13cm in diameter and weighing nearly 3kg. At the final time step of 1.15s, it can lift up a spherical chunk of asphalt from the tarmac 18cm in diameter and nearly 7kg in mass. FOD is clearly a serious safety concern for an engine operating under such conditions.

The plot in Figure 6.13 shows that the ground pressure distribution is highly affected by the inlet suction effects, suggesting that an interaction between the inlet's capture area and the ground plane is occurring. This is in agreement with the literature, as described in Chapter 2, which indicate that inlet vortices form only when the inlet's capture area overlaps with the ground (De Siervi *et al.*, 1982; Trapp and Girardi, 2010). It also suggests that an engine can operate safely when multiple smaller and weaker vortices are present, since suction effects on the ground

barely exist in such cases. In these scenarios, the engine can still ingest sand grains and even small rocks, but will most likely not suffer blade damage in the short term. For example, most modern-day airports are obligated to sweep runways and taxiways, disposing of loose rocks and pavement so that FOD to jet engines is less likely to happen. However, airports located in deserts or dusty environments present a danger of long-term blade erosion caused by ingestion of small dirt and sand particles. On the other hand, once a single inlet vortex has formed, the results presented here show that engine operation can lead to the ingestion of bigger objects lying on the tarmac such as asphalt chunks, which will damage fan blades, leading to engine failure.

6.4.2 Inlet vortex strength

The strength of the inlet vortices, i.e. their circulation, was calculated at each of the time steps selected, according to the methodology described in Chapter 3. Figure 6.15(a) displays the time history of inlet vortex strength, showing the positive, negative (absolute value) and total circulations (sum of absolute values) of the inlet vortices taken on the near-ground plane illustrated in Figure 6.3(a). Positive vorticity on this plane corresponds to a counter-clockwise-rotating vortex when viewed from above (as illustrated in Figure 6.3(b)).

In the first 0.4s of flowtime, two counter-rotating vortices exist with cores in line with each other and approximately parallel to the Z axis. The clockwise vortex is stronger than the counter-clockwise, as can be seen by the higher negative circulation. The velocity profile plots show that at approximately 0.4s the nearfield crosswind speed approaches the desired value. Figure 6.15 shows that around this same time the counter-clockwise vortex became stronger than the clockwise one. This can be understood in two ways. Firstly, increasing crosswind speed generates more vorticity within the inlet outer surface boundary layer, which in turn is transferred to the counter-clockwise inlet vortex, adding to its strength. Secondly, the ramp-up of the

crosswind speed adds more angular momentum to the counter-clockwise vortex than to its counterpart, since the first is further away from the inlet and thus subject to less suction from the inlet (as was discussed in detail in section 6.3.2).

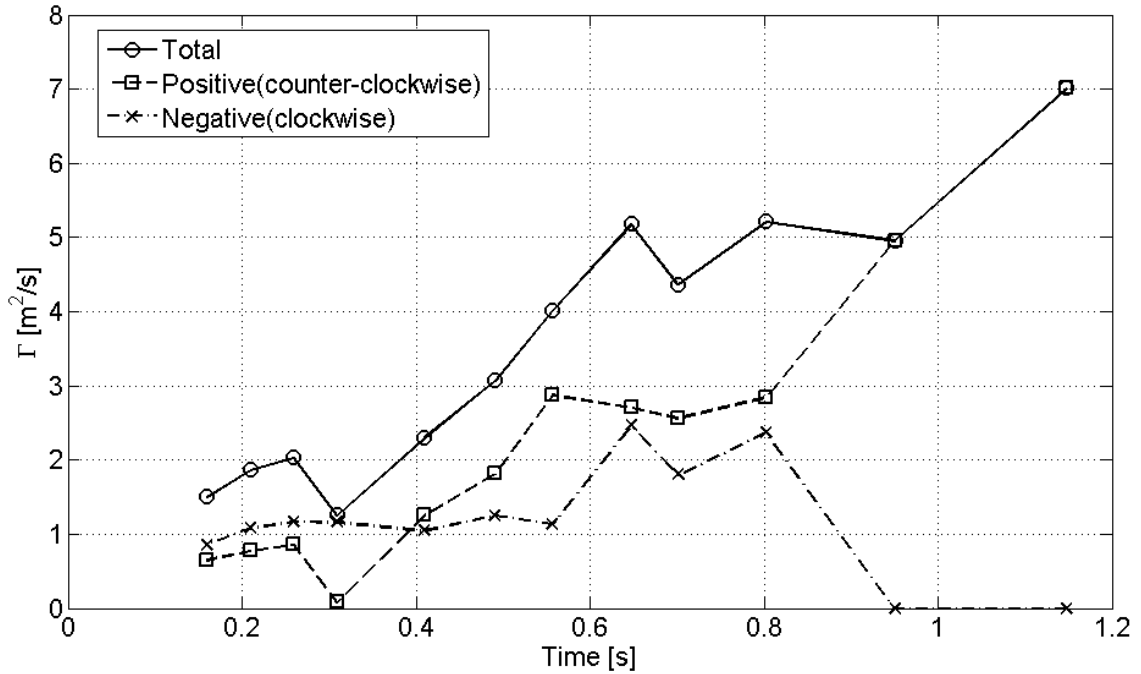


Figure 6.15 Time history of inlet vortex strength, calculated on the near-ground plane.

From 0.4s to about 0.55s, these two mechanisms are again at play, adding vorticity and angular momentum to the counter-clockwise vortex, reflected by its increase in circulation shown in Figure 6.15. The clockwise vortex strength remains fairly constant during this time interval, as does the nearfield crosswind speed and velocity ratio, suggesting that the counter-clockwise vortices receive the added vorticity generated inside the ground and inlet outer surface boundary layers. However, between 0.55s and 0.65s the strength of the clockwise vortices spikes up, even though the nearfield crosswind speed remains steady. During this time interval, three vortices were observed, two clockwise and one counter-clockwise. The counter-clockwise vortex is the

strongest, but due to the formation of one additional clockwise vortex, total negative vorticity is increased.

A rapid drop to zero in the clockwise vortex strength is observed at 0.95s as the nearfield crosswind speed decreases in response to the step-change in wind speed. This drop is accompanied by a spike in the counter-clockwise vortex strength. This clearly indicates that a single counter-clockwise vortex exists on the ground plane at this time, formed after the previously-observed vortices coalesce. The new inlet vortex has approximately the combined strength (circulation) of the clockwise and counter-clockwise vortices present just prior to the coalescing. This observation indicates that not only do the vortices physically merge, but their strengths also combine, conserving circulation in the flow.

The total inlet vortex strength (combined magnitude of positive and negative circulation of all vortices) exhibits an upward trend in time, increasing throughout the formation process, as would be expected in order to generate a strong inlet vortex. This is attributed to the production of vorticity within the nacelle outer surface and ground boundary layers and its convection into the vortex cores by the approaching flow. In agreement with Murphy and MacManus' (2011) observations, as the nearfield wind speed increases, the inlet vortex strength also increases, showing that the vorticity production is the key element in forming and sustaining such vortices. Moreover, the vortex strength also increases after the wind speed was decreased, seeming to contradict the previous explanation. However, since the multiple vortices coalesced into one single vortex, with the combined circulation of them all, then the trend shown in the graph is perfectly reasonable.

6.4.3 Trailing vortex strength

In addition to circulation due to the inlet vortices, the strength of the accompanying trailing vortex was also calculated. The calculations were carried out as detailed in Chapter 4 using a YZ plane slightly downstream of the inlet, as illustrated in Figure 6.4(a). The direction of positive X vorticity is aligned with the X axis, hence describing a vortex that swirls in a clockwise direction when looking in the positive X direction (see Figure 6.4(b)). According to Table 6.1, all time steps contain a single downstream trailing vortex, with the exception of 0.16s. At this specific time step, the nearfield wind speed has not yet reached the farfield speed specified, not enough vorticity has been shed off the surface of the nacelle, and therefore no trailing vortex exists.

Figure 6.16 shows the time history of the trailing vortex strength. All vortices observed on the YZ plane had positive vorticity, meaning they rotated in a clockwise direction looking into the plane from the upwind side. The accompanying sketch shows the plane just described and the positive rotational direction. This then means that the calculated circulation is strictly positive. Therefore, total and positive circulation can be used interchangeably. These are plotted on the same curve below. Negative circulation is also plotted on the graph for illustration purposes, but the values are all zero.

Figure 6.16 shows that before 0.4s no trailing vortices are present. This was expected for reasons described above. However, once vorticity is produced around the nacelle outer surface, the vortex forms. The general trend of trailing vortex strength is the same as that of the inlet vortex up until 0.6s, exhibiting an increase in circulation linked to the initial generation of vorticity due to the crosswind. After 0.6s the trailing vortex strength decreases from a value of $5.5\text{m}^2/\text{s}$ to $4.2\text{m}^2/\text{s}$ at the end of the simulation. The reason for this is unclear. One suggestion is that there is an exchange of vorticity between inlet and trailing vortices during the transient

formation process – this may not be true once a steady-state has been reached – and that as the inlet vortex strength increases, trailing vortex strength must decrease. This hypothesis is not supported by experiments or other numerical work, and therefore warrants further study. De Siervi *et al.* (1982) observed that the steady-state circulation of inlet and trailing vortices are nearly the same, however nothing has been said regarding the exchange of vorticity during the transience. Another hypothesis is that as the trailing vortex forms, its rate of vorticity ingestion may be smaller than the rate for downstream convection, causing it to lose vorticity with time. Once again, additional study is necessary to further explore this observation.

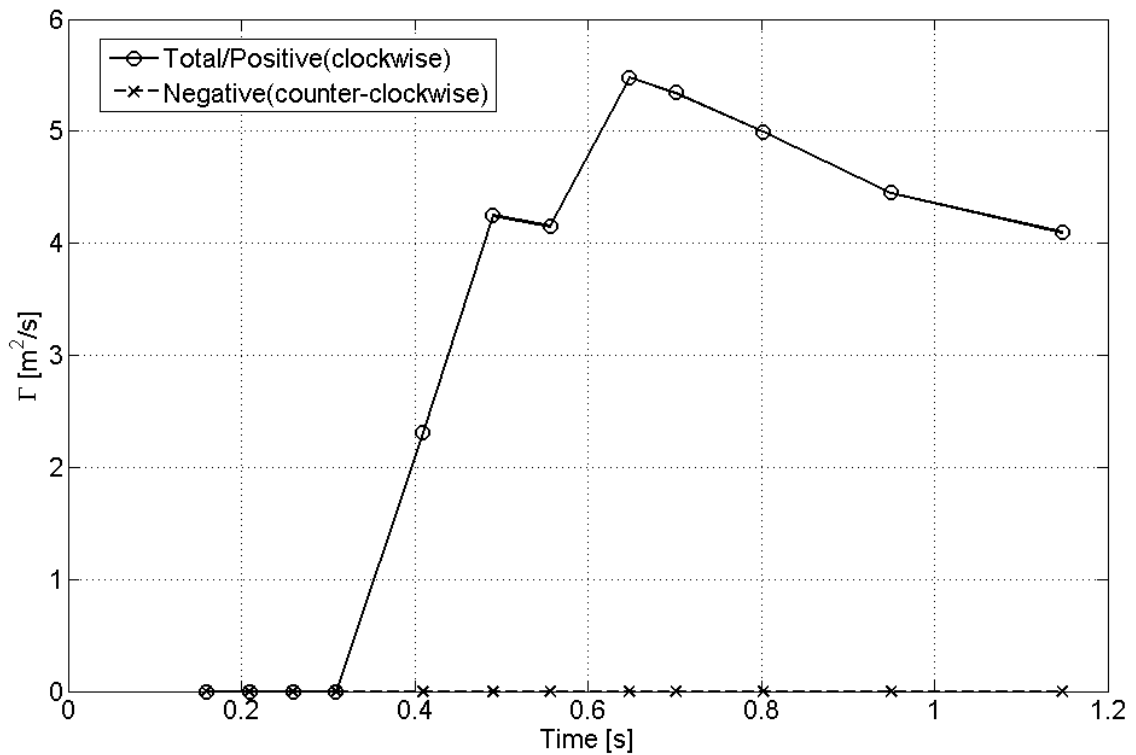


Figure 6.16 Time history of trailing vortex strength, calculated on trailing vortex plane.

It is worth mentioning that unlike the refined mesh region created in front of the inlet to accurately capture the inlet vortex, the downstream region of the inlet (where the trailing vortex would form) has a significantly coarser mesh. Thus, accurate resolution of trailing vortices and

their physical properties was limited in this model. Nevertheless, since trailing vortices have larger diameters than inlet vortices, a coarse mesh was sufficient to capture its location and approximate the vorticity it contained. However, if the trailing vortex contained higher vorticity localized over an area smaller than the local element, this value would not be accurately captured. Therefore, the trailing vortex's actual circulation may be larger than those displayed in the time history above. Further study of the trailing vortex therefore warrants a finer mesh in this area.

By the last time step described in this simulation (1.15s), a single inlet vortex has formed (as described in section 6.3.8). Figure 6.16 shows that the trailing vortex strength contains evidence of approaching (but not arriving at) steady state, as the circulation seems to be plateauing at around $4\text{m}^2/\text{s}$, which is much lower than the inlet vortex strength of about $7\text{m}^2/\text{s}$. This does not contradict De Siervi's *et al.* (1982) observation stated above, but it does indicate that during the transient inlet vortex formation process, the trailing vortex is weaker than the inlet vortex.

6.4.4 Secondary vortex strength

Out-of-plane vorticity was also integrated over a meshed zone using Tecplot on the trailing vortex plane, as shown in Figure 6.5(a). The direction of positive Z vorticity is aligned with the Z axis, hence describing a vortex that swirls in a counter-clockwise direction when looking in the negative Z direction, i.e. at the front of the inlet (see Figure 6.5(b)). A vortical structure was found on this plane and is referred to as the "secondary vortex". Figure 6.17(a) shows the time history of its circulation.

Figure 6.17 shows that no secondary vortices exist before 0.4s. As with the trailing vortices, these structures do not form until the nearfield wind velocity has become sufficiently large, because they require vorticity from the inlet outer surface to exist, and at sufficiently low

velocity not enough vorticity is produced. At just over 0.4s, two inlet vortices, one trailing and one secondary vortex appear simultaneously, and from Figure 6.15, Figure 6.16 and Figure 6.17 had around the same circulation magnitude. However, while inlet and trailing circulation increases with time beyond 0.5s, secondary vortex strength decreases with time. A possible explanation for this is that most of the vorticity produced in the boundary layer of the engine nacelle is being convected into the trailing vortex, weakening the secondary vortex.

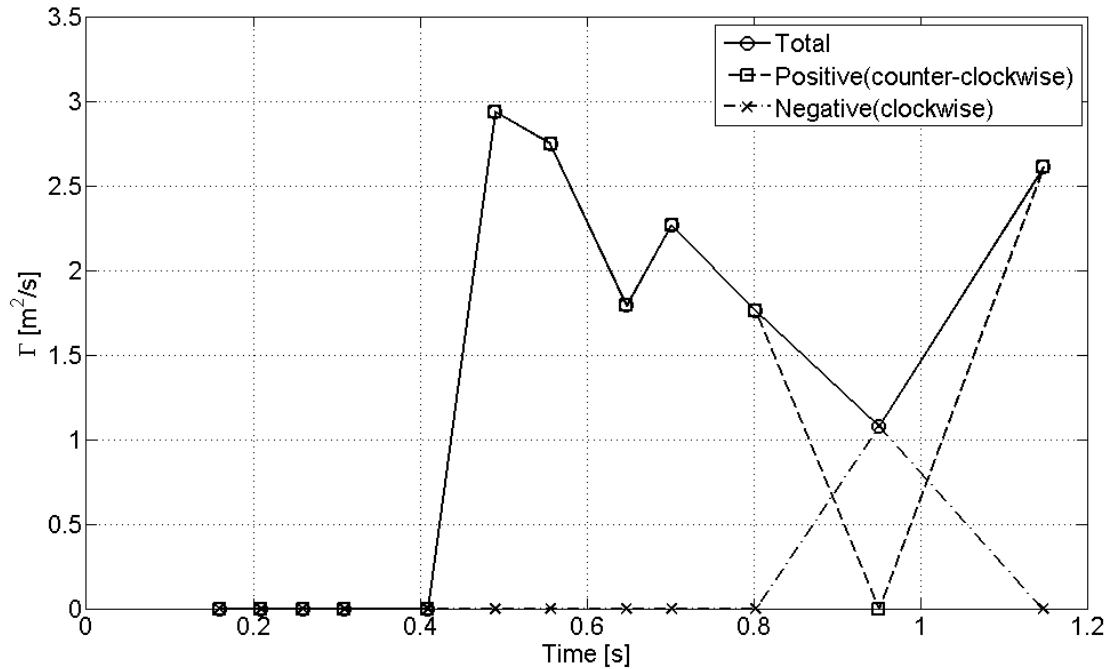


Figure 6.17 Time history of secondary vortex strength calculated on the secondary vortex plane.

At time step 0.95s, subsequent to the inlet vortices coalescing, described in section 6.3.7, a clockwise secondary vortex appears. This is the only time step at which this was observed. Figure 6.17 indicates this by showing how the positive circulation component decreases to zero while the negative component increases to about $1.1m^2/s$, at this time step. The reason for this behavior is unknown. At the following time step the vorticity returns to a counter-clockwise direction once again.

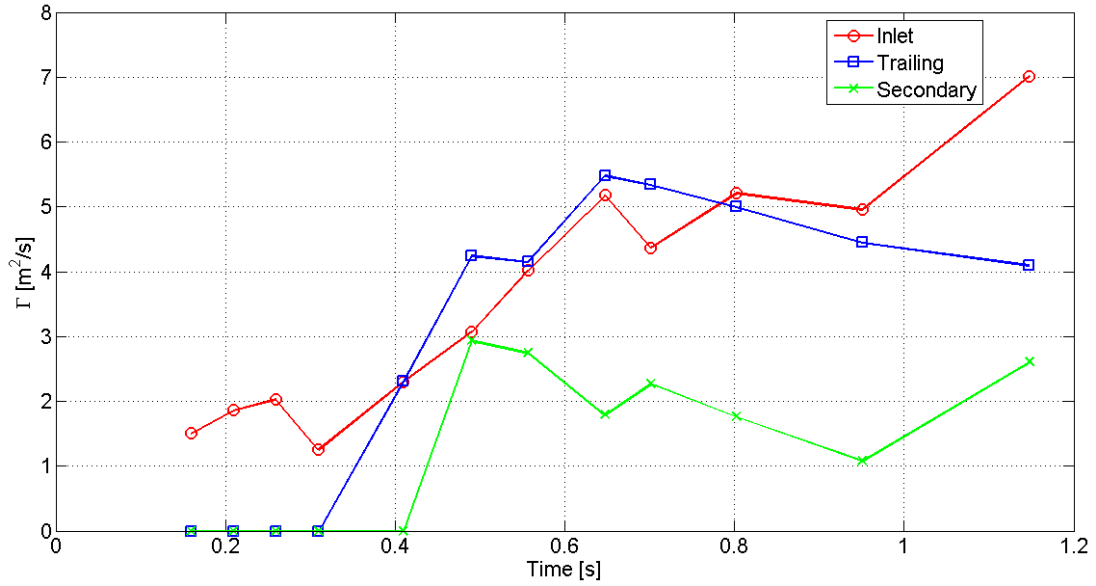
Additionally, at the last time step (1.15s), the circulation spikes up again, following the trend of the inlet vortex shown in Figure 6.15 and opposite the trend of the trailing vortex shown in Figure 6.16. The secondary vortex circulation at this point is approximately $2.6\text{m}^2/\text{s}$, whereas the inlet and trailing circulations were $7\text{m}^2/\text{s}$ and $4.1\text{m}^2/\text{s}$, respectively. The secondary vortex is therefore the weakest of all vortices in this system.

As presented in the flowfield characterization (section 6.3), the secondary vortex originates from the underside outer surface of the nacelle and thus presents no danger of FOD to the inlet. It does, however, create significant distortion of the flow at the fan face, though not nearly as much as the inlet vortex. Many questions arise regarding secondary vortices, and since in this research is the first time this structure has been observed, further investigations are needed to understand its formation and maintenance mechanisms, as well as its role in the inlet vortex phenomenon.

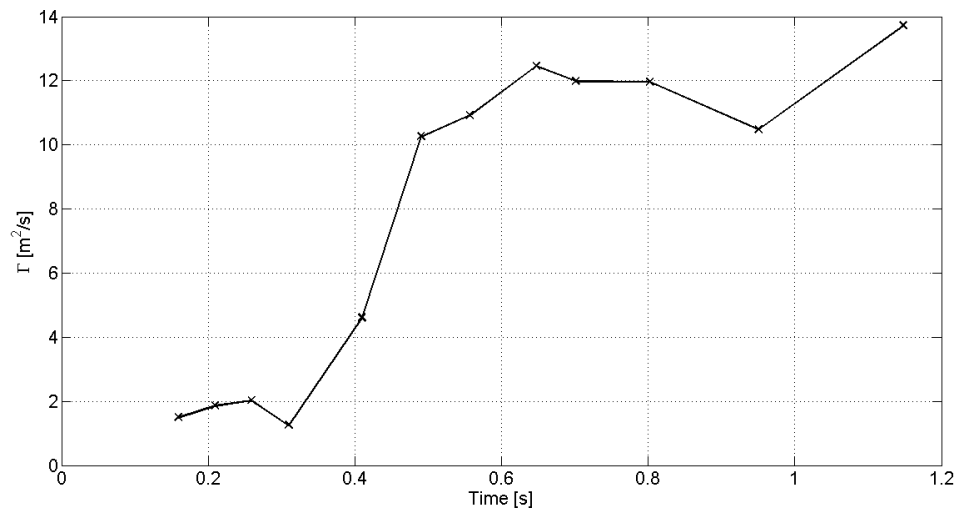
6.4.5 Total circulation plots

Figure 6.18(a) and (b) combine the information presented in sections 6.4.2-6.4.4 in two ways. Firstly, Figure 6.18(a) shows the time history of the total circulation (the addition of positive and negative magnitudes) of each individual vortex (inlet, trailing and secondary). Secondly, Figure 6.18(b) shows the sum of their circulations added together to yield the total circulation of the vortex system at each time step studied.

Figure 6.18(a) shows that before 0.4s no trailing or secondary vortices exist, and the strength of the inlet vortices present is low. However, once the nearfield crosswind speed had stabilized, trailing and secondary vortices appear, and up to 0.8s the trailing vortex strength is slightly larger, although very similar to the inlet vortex strength.



(a)



(b)

Figure 6.18 Time histories of (a) total circulation for inlet, trailing and secondary vortices and (b) combined circulation of all vortices.

The trends of vortex strength growth are representative of the vortices' formation process. As the nearfield wind speed increased, the production of vorticity within the inlet outer surface and ground plane increased, strengthening the inlet and trailing vortices, which received this vorticity via convection of fluid from the boundary layers. Figure 6.18(a) reflects this via a

general increase in circulation for both of these vortices, up until approximately 0.7s. Once the step change in wind speed is applied and the nearfield flow adapts to the new boundary condition, the trailing vortex strength decreases while the inlet vortex strength increases. There is a spike in the inlet vortex strength at the last time step, indicating more vorticity is being convected into this vortex's core. The secondary vortex displays a continual decrease in strength from the moment it forms to the second-to-last time step. At 1.15s its strength increases along with the inlet vortex strength.

The time history of the combined strength of all vortices shows interesting results. Firstly, before the nearfield wind speed had reached the boundary condition value, there is very little circulation in the system, no more than $2\text{m}^2/\text{s}$. Once the nearfield wind velocity matches the farfield specification, the total circulation jumps from about $1\text{m}^2/\text{s}$ to $10\text{m}^2/\text{s}$ in only 0.2s. It then stays around $11\text{m}^2/\text{s}$ until the final time step when it spikes to just under $14\text{m}^2/\text{s}$. Even though multiple ground-to-inlet vortices exist during this time interval, with vortex strengths varying amongst them at each time step, their total circulation combined with the trailing and secondary vortex strengths is constant. This is expected as the single inlet vortex approaches an equilibrium location on the ground.

6.4.6 Fan face distortion coefficient, DC₆₀

The fan face distortion coefficient, DC₆₀, is plotted below in Figure 6.19. The full fan face curve represents the DC₆₀ calculated at the worst 60-degree sector of the full fan face; the inlet vortex curve was obtained by forcing this 60-degree sector to include the inlet vortex/vortices ingestion location; and the modified inlet vortex was obtained by using total and dynamic pressures based on the fan face center point located at (X, Y, Z) of (0m, 0m, -0.05m). Section 4.1 describes this methodology in detail.

The full fan face and modified inlet vortex curves contain very similar results for the first 0.3s of the simulation. This can be attributed to the fact that the separation region has not yet reached a fully developed state, as illustrated in section 6.3. In other words, the stagnation and dynamic pressures at the fan face center are representative of the area-weighted average of stagnation and dynamic pressures on the full fan face. The inlet vortex curve has roughly half the distortion of the other two curves due to the fact that the separated region, though small and weak, is not included in the calculation, yielding a lower value of DC₆₀.

At around 0.4s, the windward lip separation region is fully formed and so the distortion coefficient at the full fan face peaks to about 0.32. This value is highly skewed by the separation region and does not represent the impact of the inlet vortex ingestion on fan face distortion. The modified inlet vortex curve presents a more accurate value of the distortion due to inlet vortices present in the flow. For the duration of the unsteady formation process, the average fan face distortion due to the inlet vortices is approximately 0.05.

The lip separation region also grows in size and experiences greater stagnation pressure loss with time (section 6.3). This is reflected on the graph by the peaks in the full fan face DC₆₀ at around 0.45s and 1s. These peaks corresponded to the stabilizing of the two nearfield crosswind speeds shown in Figure 6.2. At the former of these time steps, the inlet separation region has just formed, and at the latter time step the stagnation pressure loss has increased significantly due to the high nearfield velocity ratio. Therefore, peaks are expected at these exact locations, indicating higher levels of distortion at the fan face.

At approximately 0.4s the inlet vortex DC₆₀ drops to negative values and remains that way until the last time step at 1.15s. This somewhat curious effect does not imply that the inlet vortex is actually reducing distortion. Mathematically, the area-weighted average of the fan face stagnation pressure is lowered by the pressure loss contained in the separation bubble, making the

numerator in the DC_{60} equation negative. To correct this, the modified inlet vortex distortion coefficient is more relevant to the study of the current problem, as explained in section 4.1.

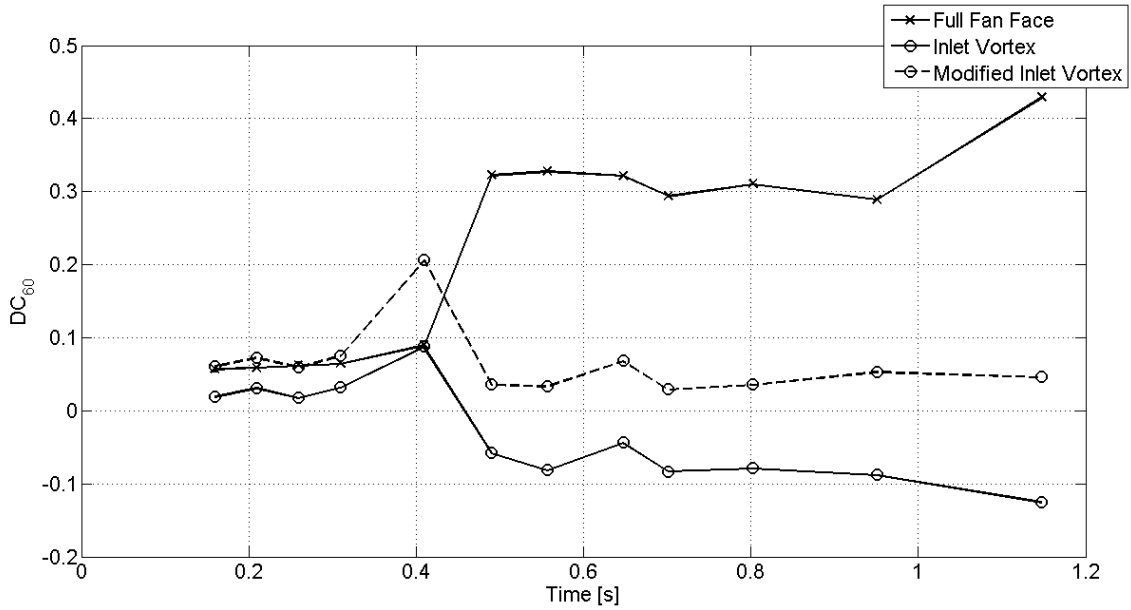


Figure 6.19 Time history of fan face distortion parameter, DC_{60} .

6.5 Conclusion

In this chapter, the flow field was characterized at selected time steps throughout the unsteady formation process. It was shown for the very first time that multiple vortices exist on the ground plane during the transient vortex formation process. These rotate in opposite directions, with a counter-clockwise vortex being the strongest. In the span of one second, these vortices coalesce into one counter-clockwise vortex which contains the added circulation magnitude of all merged vortices. This vortex is what forms the steady state inlet vortex. To the best of this author's knowledge, no other research team has studied the unsteady formation process of inlet vortices, and the results presented in this chapter showing multiple ground-to-inlet vortices have not before been observed or investigated before.

Time history plots of vortex strength, ground pressure and fan face distortion were also presented, outlining the unsteadiness of the inlet vortex formation process, characterizing the flow field quantitatively and discussing its formation mechanisms. A new vortex was identified and termed the “secondary vortex”, which was ingested by the fan face along with the inlet vortex, and had its point of origin on a stagnation point on the underside of the inlet nacelle. Inlet and trailing vortex strengths were shown to increase with time as the vortex system developed, while secondary vortex strength decreased with time. These trends were correlated to the degree of vorticity production on the nacelle outer wall and ground boundary layers. It was shown that the primary means of vortex formation is the generation of vorticity from wall surfaces, and that without such vorticity production, vortices would not exist.

Chapter 7. Conclusions and Recommendations

The inlet vortex phenomenon has been investigated both experimentally and numerically for six decades. However, the process and mechanisms by which it forms remain little understood and a successful technique for vortex prevention is yet to be developed. Chapter 7 discusses the most important conclusions obtained from the research presented in this thesis, supporting observations made by previous authors and emphasizing new knowledge of the inlet vortex problem that can aid the development of efficient prevention techniques. Recommendations for further work are also presented.

7.1 Conclusions

The work contained in this thesis made use of a u-RANS CFD model to study the transient formation process of inlet vortices. A cylindrical model of a scaled jet engine nacelle was created in ANSYS 14 and the three-dimensional, unsteady, compressible Navier-Stokes equations were solved using ANSYS FLUENT 14. The SST $k-\omega$ turbulence model was used. The flowfield was characterized at selected time steps during the 1.15s of simulation that best

described the flow physics. Time history plots of ground suction, vortex circulation and fan face distortion coefficient DC_{60} were developed and discussed.

Comparisons with existing experimental data in the literature have shown good qualitative results. However, quantitatively, they were not accurate enough. Nevertheless, due to the complexity of the inlet vortex flowfield, the RANS method remains the least computationally expensive option for studying this problem.

The flowfield characterization presented at each time step shows that the inlet vortex formation process is highly unsteady. A new vortex was observed in addition to the inlet and trailing vortices, and was named the “secondary vortex”. Due to the known tendency of u-RANS codes to create spurious vorticity, the presence of this new vortex needs to be validated experimentally, however. The inlet and secondary vortices were seen to meander, having different attachment locations on the ground and fan face planes throughout the formation process. The existence of inlet vortices has been shown to be directly related to the production of vorticity within the boundary layers and its subsequent convection to the suction and downstream flows. Before 0.4s, no secondary or trailing vortices existed. This was due to a nearfield wind speed that was not high enough to generate sufficient vorticity within the engine nacelle boundary layer. Since both the secondary and trailing vortices appear to have their origin in vorticity shed from the nacelle outer surface, these vortices did not appear until 0.4s. However, vorticity was generated on the boundary layers of the inlet’s inner surfaces and on the ground during the initial 0.4s. Results show that this vorticity production is enough to generate two counter-rotating inlet vortices. De Siervi *et al.* (1982) suggest that, in order for an inlet vortex to exist, a source of vorticity must be present in the flow. The research described here shows that this vorticity can be present in either the ground or nacelle boundary layers. In other words, an inlet vortex will exist if vorticity is being produced on the ground surface, even if very little is generated on the nacelle

surface. As the nearfield crosswind speed increases, the inlet vortices are pushed downstream and their strengths increase. Vorticity is then produced both in the outer nacelle boundary layers as well as on the ground, and is convected by the crosswind and inlet suction effects to the existing vortex cores.

During the first 0.9s of simulation, three inlet vortices were observed in addition to the trailing and secondary vortices. The two clockwise-rotating vortices were the weakest and remained that way; the counter-clockwise vortex was weak initially but was seen to gain strength as more vorticity was produced in the system. After 0.9s of calculation, the smaller vortices were observed to coalesce with this stronger vortex to form a single inlet vortex with a counter-clockwise sense of rotation.

De Siervi *et al.* (1982) published a correlation that determined at what velocity ratio an inlet vortex would occur, for a given engine height ratio. This correlation, however, is shown to be applicable only when an engine operates at steady-state (constant wind and suction speeds). The research described here has shown that the correlation may not apply during the unsteady vortex formation process, if multiple inlet vortices are in fact present instead of just one.

The near-ground static pressure time history has revealed that while multiple inlet vortices coexist, FOD is not a concern for engine operation. However, once the merging of these vortices occurs, the resulting inlet vortex was observed to have significantly higher suction strength, capable of lifting a 17cm spherical chunk of asphalt from the ground, posing a substantial threat of FOD.

7.2 Recommendations

Despite the computational expense of running a model of the size studied here, CFD remains the least expensive approach to studying this phenomenon. In light of this fact, below are some recommendations for improving the accuracy of the numerical model used in this research:

1. Conduct a parametric study varying the turbulence model and relevant turbulence level constants in order to determine the optimal setup that would improve the results of the validation presented in Chapter 5, in which the model was compared with Murphy and MacManus' (2011) experiments.
2. Conduct detailed research into expected turbulence levels on the fan face, so as to specify fan face turbulence levels with more confidence. This may help resolve the lip separation issues found here.
3. Once items 1 and 2 have been accomplished, this author suggests simulating the case study contained herein once again to observe if secondary vortices are still present and if vortex coalescence still occurs.

Once a model with higher accuracy has been developed based on recommendations 1-3, the following suggestions can also be incorporated:

4. Create a refined region of mesh downwind of the inlet where the trailing vortex is expected to form. This will improve the accuracy of the trailing vortex circulation and allow for better comparison with the other vortices.
5. Specify the number of iterations per time step to be at least 2000. This will allow residuals to reach levels of 10^{-5} to 10^{-6} and yield more trustworthy results. However, this will increase the computational cost.

7.2.1 Engine ramp-up study

The case investigated in this thesis research is that of an engine inlet operating at a fixed Mach number of 0.55 (representative of take-off conditions) and undergoing a step-change in crosswind speed. An additional study could be undertaken of an inlet in a fixed crosswind, in which the engine undergoes a ramp-up in rotations per minute (rpm) and therefore engine suction speed, resembling the transience of an engine start-up at the beginning of a take-off run. This study would require a slightly more complicated boundary condition setup in ANSYS FLUENT but will characterize the unsteady vortex formation process for an aircraft at take-off.

7.2.2 Vortex prevention considerations

Preventing inlet vortex formation is a significant challenge, as evidenced by the length of time engineers have sought, unsuccessfully, to achieve it. Today, there are no techniques available that can be implemented to prevent the formation of inlet vortices. Within the accuracy of this present model, results have shown that the formation process of inlet vortices is characterized by the presence of multiple weaker inlet vortices which coalesce to form a single ground-to-inlet vortex. This may suggest a new approach to developing prevention techniques. If the coalescing of the weak vortices can be inhibited, then the chances of FOD are reduced and fan face distortion kept to a minimum. It is safer and less harmful for an engine to operate with multiple weaker vortices that can only pick up rocks with a diameter of at most 2cm than to operate with one single vortex that can lift a large chunk of pavement from the ground. We therefore recommend the investigation of techniques to prevent coalescing of these weaker vortices, rather than techniques that attempt rather to disrupt an already formed vortex, as all those currently patented attempt to do.

7.2.3 Experimental rig and testing

In order to validate the observations made in this research, an experimental investigation is necessary, replicating the exact conditions of the case studied here. Figure 7.1 shows a conceptual design of a vertically-positioned cylindrical inlet mounted onto a turntable and attached to the end of a blower-type wind tunnel, suggested for such experimental validation. The crosswind velocity is set by the wind tunnel speed and the inlet's suction is achieved by using an adequately-sized heavy-duty fan. As in the numerical calculations presented herein, the inlet Mach number would be matched to 0.55 resembling engine take-off conditions. The turntable can be rotated to study vortex formation at different yaw angles. The use of a PIV (Particle Image Velocimetry) optical system is recommended to characterize the flow velocity field, allowing for the calculation of vorticity and circulation at the vortex cores. Smoke can be used to visualize the inlet vortex core and the inlet's capture area, and wool tufts or oil of wintergreen to study ground flow topology.

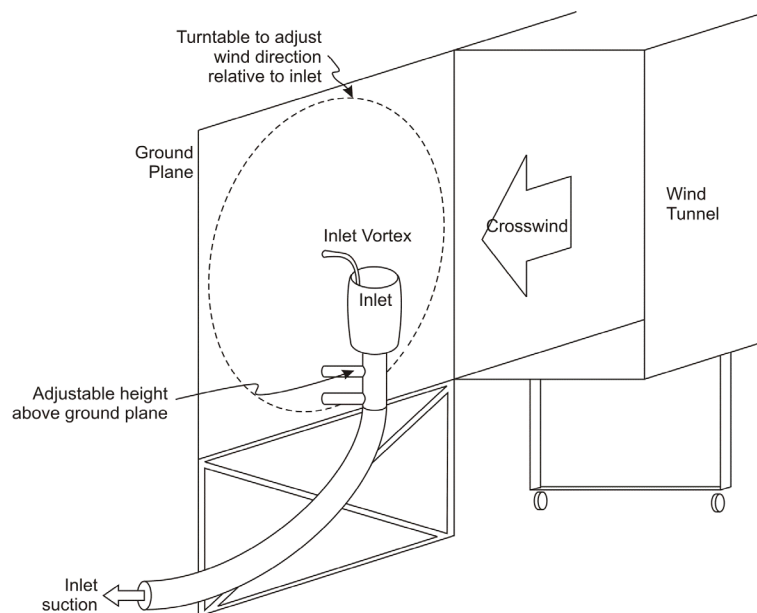


Figure 7.1 Conceptual design of experimental rig.

Bibliography

ANSYS 14 User's Guide, 2012

Barata, J. M. M., Manquinho, P., and Silva, A. R. R., "A Comparison of Different Gas Turbine Engines Ground Vortex Flows," AIAA 2010-7116.

Barata, J. M. M., Manquinho, P., and Silva, A. R. R., "Identification of Gas Turbine Ground Vortex Formation Regimes," AIAA 2012-0600.

Brix, S., Neuwerth, G., and Jacob, D., "The Inlet-Vortex System of Jet Engines Operating Near The Ground," AIAA Paper 2000-3998, June 2000.

Colehour, J. L., and Farquhar, B. W., "Inlet Vortex," *Journal of Aircraft*, Vol. 8, No. 1, January 1971, pp. 39-43.

Cox, P. O., and William, J., Rolls Royce Engines, U.S. Patent for "Pod for a Gas Turbine Engine," No. 3,474,988. F02C7/05, filed 28 Oct. 1969.

De Siervi, F., Viguier, H. C., Greitzer, E. M., and Tan, C. S., "Mechanisms of Inlet-Vortex Formation," *Journal of Fluid Mechanics*, Vol. 124, 1982, pp. 173-207.

Funk, R., Parekh, D., Smith, D., and Dorris, J., "Inlet Vortex Alleviation," AIAA Paper 2001-2449, June 2001.

Glenny, D. E., and Pyestock, N. G. T. E., "Ingestion of Debris into Intakes by Vortex Action," Aeronautical Research Council, Paper 1114, London, 1970, pp. 1-50.

Ho, H. W., Jermy, M., "Validated CFD Simulations of Vortex Formation in Jet Engine Test Cells," *16th Australasian Fluid Mechanics Conference*, Dec. 2007

Klein, H. J., "Small Scale Tests on Jet Engine Pebble Aspiration," Douglas Aircraft Co. Rept. SM-14885, Long Beach, CA, 1953.

Klein, H. J., U.S. Patent for "Vortex Inhibitor for Aircraft Jet Engines," Douglas Aircraft Co., No. 2,915,262. B64D33/02, filed 1 Dec. 1959.

Liu, W., Greitzer, E. M., and Tan, C. S., "Surface Static Pressures in an Inlet Vortex Flow Field," *Journal of Engineering for Gas Turbines and Power*, Vol. 107, April 1985, pp. 387-393.

Murphy, J. P., "Intake Ground Vortex Aerodynamics," *Ph. D. dissertation*, Cranfield University, 2008

Murphy, J. P., and MacManus, D. G., "Ground Vortex Aerodynamics Under Crosswind Conditions," *Experimental Fluids*, Vol. 50, 2011, pp. 109-124.

Murphy, J. P., and MacManus, D. G., "Inlet Ground Vortex Aerodynamics Under Headwind Conditions," *Aerospace Science and Technology*, Vol. 15, 2011, pp.207-215.

Murphy, J. P., MacManus, D. G., and Taylor, M. D., "A Quantitative Study of Inlet Ground Vortices," ISABE-2007-1209.

Nakayama, A., and Jones, J. R., "Correlation for Formation of Inlet Vortex," *AIAA Journal*, Vol. 37, No. 4, pp. 508-510.

Raymer, D. P., "Aircraft Design: A Conceptual Approach," 4th edition, 2006, pp. 228.

Secareanu, A., Moroianu, D., Karlsson, A., and Fuchs, L., "Experimental and Numerical Study of Ground Vortex Interaction in an Air-Intake," AIAA Paper 2005-1206, Jan. 2005.

Shin, H. W., Greitzer, E. M., Cheng, W. K., Tan, C. S., and Shippee, C. L., "Circulation Measurements and Vortical Structure in an Inlet-Vortex Flow Field," *Journal of Fluid Mechanics*, Vol. 162, 1986, pp. 463-487.

Shmilovich, A. and Yadlin, Y., "Engine Ground Vortex Control," *24th Applied Aerodynamics Conference*, 5-8 June 2006, San Francisco, California.

Shmilovich, A. and Yadlin, Y., "Flow Control Techniques for Transport Aircraft," *AIAA Journal*, Vol. 49, No. 3, March 2011.

Smith, J. P., Hawker Siddeley Aviation, U.S. Patent for "Protective Air Curtain for Aircraft Engine Inlet," No. 3,527,430. F02C7/05., 8 Aug. 1970.

Trapp, L. G. and Girardi, R. da M., "Crosswind Effects on Engine Inlets: The Inlet Vortex", *Journal of Aircraft*, Vol. 47, No. 2, March-April 2010, pp. 577-590.

Trapp, L. G. and Girardi, R. da M., "Evaluation of Engine Inlet Vortices Using CFD", AIAA 2012-1200, *50th Aerospace Sciences Meeting*, Nashville, TN, USA, 2012.

Vunnam, K., and Hoover, R., "Modeling of Inlet Distortion using a Combined Turbofan and Nacelle Inlet Model during Crosswind and Low Speed Forward Operation," *Proceedings of ASME Turbo Expo 2011*, GT2011-46466.

Wakelam, C. T., Hynes, T. P., Hodson, H. P., Evans, S. W., and Chanez, P., "Separation Control for Aero Engine Intakes, Part II: Low Speed Investigation of Control Strategies," *Journal of Propulsion and Power*, Vol. 28, No. 4, July-August 2012.